

# Scanning Near-Field Optical Microscopy of Living Cells in Liquid, Elaboration of New SNOM Probes and Detection Methods

THÈSE N° 4984 (2011)

PRÉSENTÉE LE 23 FÉVRIER 2011  
À LA FACULTÉ SCIENCES DE BASE  
LABORATOIRE DE PHYSIQUE DE LA MATIÈRE VIVANTE  
PROGRAMME DOCTORAL EN PHYSIQUE

ÉCOLE POLYTECHNIQUE FÉDÉRALE DE LAUSANNE

POUR L'OBTENTION DU GRADE DE DOCTEUR ÈS SCIENCES

PAR

Kanat DUKENBAYEV

acceptée sur proposition du jury:

Prof. O. Schneider, président du jury  
Prof. G. Dietler, Dr S. Sekatski, directeurs de thèse  
Dr V. Prokhorov, rapporteur  
Prof. A. Radenovic, rapporteur  
Prof. A. Zayats, rapporteur



ÉCOLE POLYTECHNIQUE  
FÉDÉRALE DE LAUSANNE

Suisse  
2011





*Осы жұмысымды сіздерге:  
Гүлмира, Алихан, Алматы  
және Ата-анама  
арнадым қымбатты жанұям.*



*To Gulmira, Alikhan, Almat  
and my parents  
I dedicate this work.*





# Abstract

The aim of the present PhD thesis is the elaboration of new, home-made Scanning Near-field Optical Microscope (SNOM or NSOM), and the demonstration of its great potential for high-resolution topography and fluorescence investigations of soft and solid samples, as well as the possibility to work in air and liquid environments showing high-resolution topographical and fluorescence abilities to investigate soft and solid samples.

The **first** chapter starts from with the description of the general idea of SNOM and with a brief introduction into to the history and theory of optical image formation, and leading to the resolution limits in conventional optical microscopy. The following section will discuss about the different state-of-the-art different SNOM configurations and theirs peculiarities.

The **second** chapter discusses the SNOM instrumentation and its operation in liquid. The central idea of the proposed approach is the application of the “joint recipient principle” method. Then we will describe the double-resonance principle of the SNOM sensor, and the preparation of glass optical fibers by chemical etching. In addition, the description of the important technical components (lasers, filter and so on) for the SNOM experiment conclude this chapter.

The **third** chapter focus is on the time-gated pulse excitation and optical signal detection of SNOM images. The technical configuration of the SNOM is presented in more details.

The **fourth** chapter starts from with a broad overview of living bacteria *Escherichia coli* (*E.coli*) and of the Green *Synechococcus* – type of Picocyanobacteria cell lines, and presents the distinctive advantages for of the SNOM investigations working in native physiological conditions. The following sections emphasize our obtained high-

resolution experimental SNOM result measurements, then followed a discussion of the results follows. The sample preparation and deposition procedures of the living cells for the scanning will are also discussed in this chapter.

The chapter **five** introduces our recently developed SNOM sensor, based on polymethylmethacrylate (PMMA) plastic optical fiber. The chemical preparation of sharp ( $>100$  nm) tips, and its significant advantages will be illustrated by experimental results.

**Keywords:** SNOM, double resonance, glass optical fiber, joint recipient principle, signal to noise ratio, pulse/gated detection, E.coli, Cyanobacteria, Scytonemin, Chlorophyll  $\alpha$ .

# Résumé

L'objectif de ce travail de thèse est l'élaboration d'un nouveau microscope optique à balayage à champ proche (SNOM ou NSOM) et la démonstration de son grand potentiel pour les mesures topographiques et par fluorescence à haute résolution de substrats rigides et flexibles, en air et en liquides.

Le **premier** chapitre commencera par la description des principes généraux du SNOM et par une brève introduction à l'histoire et à la théorie de la formation des images optiques et des limites de résolution des techniques de microscopie optique conventionnelles. L'étape suivante exposera les différentes configurations standards du SNOM et leurs particularités.

Le **deuxième** chapitre présentera l'instrumentation du SNOM et son utilisation en liquide. L'idée centrale de l'approche proposée ici est l'application de la méthode dite du "principe des récipients communicants". Nous décrirons, ensuite, le principe de double-résonance du senseur SNOM et la préparation des fibres optiques en verre par attaque chimique. En conclusion du chapitre, nous présenterons les composantes techniques les plus importantes relatives au SNOM (lasers, filtres, etc.).

Le **troisième** chapitre se concentrera sur l'excitation par impulsion temporelle et sur la détection des signaux optiques des images SNOM. La configuration technique du SNOM y sera présentée plus en détails, et les résultats obtenus seront discutés.

Le **quatrième** chapitre débutera par une présentation générale de la bactérie *Escherichia coli* (*E. coli*) et de la picocyanobactérie verte de type *Synechococcus*, ainsi que les avantages particuliers de l'investigation par SNOM en conditions physiologiques natives. Les étapes suivantes montreront nos mesures expérimentales à haute résolution obtenues par SNOM suivies d'une discussion des résultats. Les procédures de préparation des échantillons et la déposition des cellules vivantes pour l'observation sont également abordées dans ce chapitre.

Le chapitre **cinq** présentera notre sonde SNOM, récemment mise au point, basée sur des fibres optiques en plastique polyméthacrylate de méthyle (PMMA). La préparation chimique des pointes ( $> 100$  nm), et ses avantages significatifs seront illustrés par des résultats expérimentaux.

**Mots clé:** SNOM, double-résonance, fibre optique de verre, principe des récipients communicants, rapport signal sur bruit, détection impulsion/barrière, E.coli, Cyanobactérie, Scytonemin, Chlorophylle  $\alpha$ .



# CONTENTS

<b>Abstract</b>	<b>iii</b>
<b>Résumé</b>	<b>v</b>
<b>Acronyms</b>	<b>ix</b>
<b>Introduction.</b>	<b>1</b>
<b>Chapter 1.</b>	<b>4</b>
<b>Scanning Near-field Optical Microscopy (SNOM)</b>	<b>4</b>
1.1 Brief history of SNOM	4
1.2 The resolution beyond diffraction limit	5
1.2.1 Far-field optics	6
1.2.2 Near-field optics	6
1.3 Different modes of operation of SNOM	7
1.4 Varieties of super-resolution fluorescence microscopes.	9
<b>Chapter 2</b>	<b>13</b>
<b>SNOM instrumentation.</b>	<b>13</b>
2.1 Introduction	13
2.2 SNOMs sensor and preamplifier	16
2.2.1 Sensor's preamplifier	23
2.3 SNOM sensor fabrication	26
2.4 Installation of the scanner head onto the inverted optical microscope.	28
2.5 XYZ piezo-cylinders	29
2.6 Lasers, filters and photon counter detectors.	30
2.7 Electronics unit of the SNOM	31
2.8 SNOM software	32
2.9 SNOM operation in liquid.	32
<b>Chapter 3</b>	<b>37</b>
<b>Pulse excitation/gated detection of an optical signal.</b>	<b>37</b>
3.1 The single molecule fluorescence spectroscopy detectors	37
3.2 Photon counting interface: pulse excitation and gated detection of an optical signal	38
3.3 Conclusion.	42

<b>Chapter 4</b> . . . . .	<b>43</b>
<b>Imaging of live <i>E.coli</i> and Green <i>Synechococcus</i> cells</b> . . . . .	<b>43</b>
4.1 <i>Escherichia coli</i> bacteria . . . . .	43
4.2 Green <i>Synechococcus</i> cells . . . . .	46
4.2.1 Varieties of Cyanobacteria . . . . .	47
4.2.2 Cyanobacterial pigments and Photosynthesis. . . . .	51
4.2.2.1 Scytonemin pigment. . . . .	52
4.2.2.2 Chlorophyll $\alpha$ pigment . . . . .	56
4.3 Near field optical detection of the living cells . . . . .	59
4.3.1 Introduction . . . . .	59
4.3.2 Experimental and results . . . . .	59
4.4 Sample preparations and methods . . . . .	66
4.5 Conclusions . . . . .	67
<b>Chapter 5</b> . . . . .	<b>68</b>
<b>NSOM using polymethylmethacrylate optical fiber probe</b> . . . . .	<b>68</b>
5.1 Introduction . . . . .	68
5.2 Experimental . . . . .	69
5.3 Results and discussion . . . . .	75
5.4 Conclusion . . . . .	78
<b>Appendix I</b> . . . . .	<b>79</b>
<b>Appendix II</b> . . . . .	<b>82</b>
<b>Appendix III.</b> . . . . .	<b>83</b>
<b>Appendix IV.</b> . . . . .	<b>84</b>
<b>Bibliography.</b> . . . . .	<b>85</b>
<b>Acknowledgements</b> . . . . .	<b>92</b>
<b>CV</b> . . . . .	<b>94</b>

# ACRONYMS

<b>AFM</b>	Atomic Force Microscopy
<b>APC</b>	Allophycocyanin
<b>Chl <math>\alpha</math></b>	Chlorophyll $\alpha$
<b>CPC</b>	C-phycoerythrin
<b>EA</b>	Ethyl Acetate
<b>E.coli</b>	Escherichia coli
<b>FCS</b>	Feedback Control Systems
<b>FLIM</b>	Fluorescence Lifetime Imaging
<b>FRET</b>	Fluorescence Resonance Energy Transfer
<b>GFP</b>	Green Fluorescent Protein
<b>HF</b>	Hydrofluoric Acid
<b>NA</b>	Numerical Aperture
<b>NSOM</b>	Near-field Scanning Optical Microscope
<b>PALM</b>	Photoactivable Localization Microscope
<b>PMMA</b>	Polymethylmethacrylate
<b>PMT</b>	Photo-Multiplier Tube
<b>POF</b>	Polymer Optical Fiber
<b>PS I</b>	Photosystem I
<b>PS II</b>	Photosystem II
<b>PSTM</b>	Photon Scanning Tunneling Microscope
<b>SNOM</b>	Scanning Near-field Optical Microscope
<b>SPAD</b>	Single-Photon Avalanche Diode
<b>SPM</b>	Scanning Probe Microscope
<b>SSIM</b>	Saturated Structured Illumination Microscope
<b>STED</b>	Stimulated Emission Depletion Microscope
<b>STOM</b>	Scanning Tunneling Optical Microscope
<b>STORM</b>	Stochastic Optical Reconstruction Microscope
<b>STM</b>	Scanning Tunneling Microscope
<b>TGEU</b>	Time-Gating Electronic Unit
<b>TIR</b>	Total Internal Reflection
<b>TF</b>	Tuning Fork
<b>UVR</b>	Ultra Violet Radiation



# Introduction

Mankind has always been keen about being able to see through the microscope, in order to understand all kinds of natural phenomena. The degree of resolution of microscopes has increased over the centuries from a few tens to almost a million times. The latter techniques like the electron microscope allowed one to be able to see with molecular resolution. However, only two decades ago a new technique was invented, the scanning probe microscope (SPM), which revolutionized the whole microscopy application area. Actually the first type was based on scanning tunneling microscopy (STM), and some years later atomic force microscope (AFM) was added to these SPMs [1].

Later on, in early eighties of last century, another powerful member of SPM technique was created a Scanning Near-field Optical Microscopy (SNOM or NSOM). SNOM is becoming one of the most useful microscopes among the SPMs types. The *advantage* of SNOM is inherent spectral information, which allows for chemical imaging of surface adsorbates. The confinement of light by subwavelength scatterers is known to play a dominant role on SNOM imaging and enables to make resolution far beyond the diffraction limit possible [1]. Moreover, technological developments of varieties of SNOM types is at present days continuing.

Despite its limitations, optical microscopy is the most popular microscopy technique today. It is fast, cheap, provides a wealth of information and allows to investigate samples at ambient conditions. The latter point is of particular importance when biological objects are to be studied in their native environments, an application that is largely responsible for its popularity, especially in research. With all its advantages,

optical microscopy is the most indispensable tool and ideally complemented rather than rivaled by the more recent higher resolution techniques, such as scanning electron microscopy or scanning tunneling microscopy [2].

Experimental SNOM setups (Fig. 1) have many similarities with other SPM setups. A suitable probe is approached to close distance to the sample. Piezoelectric actuators raster-scan the probe across the sample surface, and the physical properties of interest are recorded at each point of the scan. In SNOM, this probe most often is a subwavelength light source or “entrance of the detector” [2].

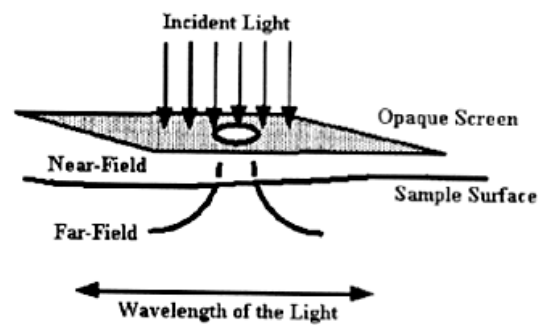


**Fig. 1** Principle of Scanning Near-field Optical Microscope using a fiber-optic probe [3].

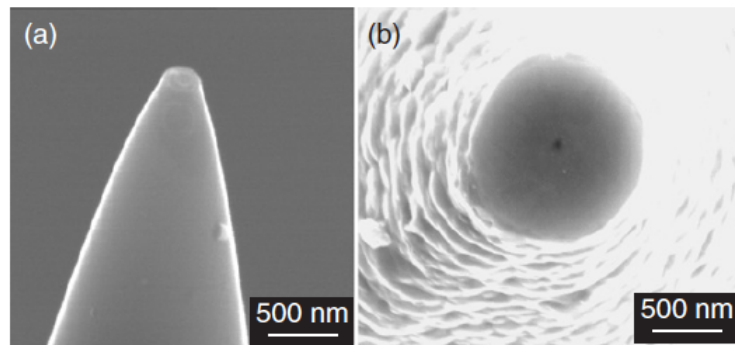


**Fig. 2** (a) Scanning electron micrograph showing the shaft of a near-field optical probe. The probe is constituted of a pulled optical fiber coated with a thin layer of aluminum. (b) View of the front face displaying an aperture of 50 nm in diameter (dark spot at the center) [4].

Light reflected or transmitted by the sample is detected at discrete measurement points during the scan. With a conducting tip and sample, the tip-to-sample distance can be controlled via the tunneling current and a topographical (STM) image is

provided simultaneously with the NSOM image. Nanopositioning and precise scanning control are critical for a distortion-free, high-resolution image [3].

Since the invention of first complete version of SNOM by Pohl and Lewis [5, 6], already past two decades, and technical as well as theoretical improvements are still in progress. Nowadays the use of SNOM in photonics, plasmonics and nanotechnology is more and more appreciated. Applications of this technique especially in biology become an additional significant advantage.

In our laboratory we have at our disposal a home-made SNOM, which has been several times modified for different tasks. The principal goal of these transformations was to make it capable to work in *liquid* environment, with possibilities of reaching the single molecule resolution in the future. Among all the technical features, I would like to point out the following advantages of our SNOM, compared to the most of currently existing near-field techniques: 1) the stability of the electronic and scanner head units during the work in air and liquid environments (this allows us to investigate biological specimens in their native/physiological conditions); 2) possibilities of observation a highly-resolved topographical and near-field optical images; and 3) the potentials of use to investigate soft and solid, organic or nonorganic materials.

# Chapter 1

---

## Scanning Near-field Optical Microscopy

This chapter starts with a brief introduction of the historical, theoretical and technical overview of Scanning Near-field Optical Microscopy (SNOM, or Near-field Scanning Optical Microscopy, NSOM). In this chapter, we discuss optical resolution limit of conventional far-field optical microscope and double-resonance principle for the SNOM sensor. In the final section of this chapter we will describe different operational modes of current SNOM techniques and the state-of-the-art Near-field Optical measurements.

### 1.1 Brief history of SNOM

SNOM belongs to the family of high-resolution microscopes relying on proximal probes such as scanning tunneling microscopes (STMs) and atomic force microscopes (AFMs). The resolution in such apparatus is obtained by raster scanning a minute probe, generally a tip, very close or in a contact to the surface to be imaged [5]. For each lateral coordinate of the tip, the observable (e.g., a tunnel current for STM, interaction forces for AFM, and an optical contrast for SNOM) is stored and displayed to reconstruct a two-dimensional map of the surface [7].

The sizing of optical elements down to the nanoscale, in order to be able to confine the optical fields to nanoscale was the fundamental idea of Synge [8], who proposed to use a hole in a metal screen to confine the optical fields laterally to the extent of such an aperture. In other words, he suggested bringing a source of light with dimensions smaller than the wavelength very close to a surface to circumvent the diffraction limit [8]. According to the reciprocity theorem, a local source of illumination is analogous to



local scatterer [9]. Therefore, the theorem implies that the fine details of an object can be recovered by either diffusing the evanescent fields of an illuminated object with a small scattering center or by illuminating the object with evanescent fields created by a local point-like source [10, 11].

Several historically important papers [5, 12, 13, 14], described the first complete versions and several interesting developments of the SNOM technique, where the main purpose was to obtain high-resolution nanometer sized near-field optical images. Nowadays, SNOM became one of the powerful scientific tools for characterization of different parameters such as morphology, structure and optical properties of organic and nonorganic samples.

Finally, during the last decade the researches in the near-field optical domain has contributed a lot to the development of several new SNOM areas such as Plasmonics SNOM, as well as Single Molecule Spectroscopy and Fluorescence Resonance Energy Transfer (FRET) SNOM, where the optical resolution can reach and down to 10 nm. In the following sections, we will discuss the origin of the diffraction limit, and will reveal one way to overcome this limit by looking at the optical image formation.

## 1.2 The resolution beyond diffraction limit

Traditional optical microscopy based on lenses has been the most popular (actually, the only one) microscopy method for over 300 years. The main reasons for this are the ease of handling and low price compared to other advanced microscopy techniques.

Despite the incessant improvements, during these 300 years, still the “light cannot be confined to a linear dimensions much smaller than  $\lambda/2$ ” [15]. This signifies the optical resolution is diffraction-limited to approximately half the optical wavelength, i.e. about 200 to 300 nm in visible spectral range [16]. SNOM is a method to obtain information about the optical properties of a sample at a lateral resolution below the diffraction limit of far-field microscopy [17].

## 1.2.1 Far-field optics

In conventional optical microscopy, lenses with a finite numerical aperture (NA), are placed in the optical far field. Optical microscopy could not resolve structures much smaller than the wavelength of visible light (400–700 nm) because of the diffraction limit [15, 18]. Each spot on the sample emits its own diffraction pattern. A classical optical microscope illuminates all spots at once, and therefore has to distinguish the corresponding diffraction patterns from each other. This, however, is only possible if the spots are farther apart than:

$$R = 0.61 \frac{\lambda}{n \sin(\theta)}$$

where  $\mathbf{n}$  is the refractive index while  $n \sin(\theta)$  is the numerical aperture;  $\lambda$  is the wavelength, and **0.61** is “the factor that depends on the intensity distribution of the light beam falling on the objective” [19] (Rayleigh criterion); and  $\mathbf{R}$  is the smallest distance between two objects that can still be resolved.

## 1.2.3 Near-field optics

The waves containing the highest spatial frequency information about the object do not propagate but decay exponentially with the distance from the object. The SNOM is based on detection of these non-propagating evanescent waves in the near-field zone, in order to obtain the high spatial frequency information of the object. For this a probe has to be brought into the near-field zone, close to the sample to either detect the near-field directly, by means of a nanometer-size detector, or to convert the evanescent waves into propagating waves and detect these in the far-field, by using a nanometer-size scatter source or a waveguide with subwavelength size aperture of 50-100 nm. In order to improve the lateral resolution beyond the diffraction limit, the variations of the field associated with the high spatial frequencies need to be detected [7]. The Fig. 3 illustrates the detection of the evanescent wave in the near-field region using metalized aperture optical SNOM probe.

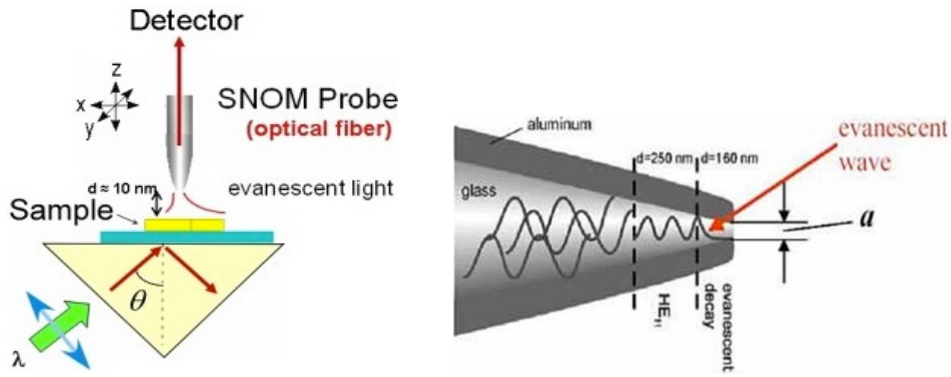
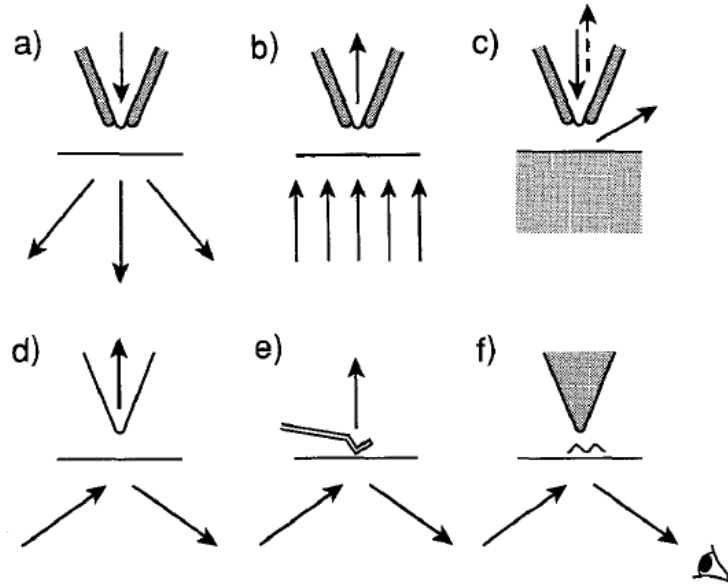


Fig. 3 The schematics of evanescent wave in the near-field optical region using metalized optical SNOM probe [20, 21].

### 1.3 Different modes of operation of SNOM

In this section of the present Thesis we will discuss different configurations of SNOM. Depending on the scientific problem, the configuration of SNOM can be varied from one device to another. In Fig. 4, we show the most common modes of operations, where each mode can be associated with a different instrumental configuration. The *first* mode is the “illumination mode”, proposed by [5, 6, 14, 22] in early eighties. This was the original SNOM technique, where the light is illuminating through a local probe placed near the sample and the evanescent field is generated at the tip end. As the tip approaches to the distance where near field is shared by tip and sample, light is scattered from the probe and sample system. Since the scattered light is a propagating wave, NSOM image is obtained by collecting the scattered light [23]. The *second* type is called “collection mode” and was proposed by [24]. The *third* type of SNOMs mode is reflection mode: a dielectric probe illuminates the sample, the radiation reflected off the surface is collected either by far-field optics, or by the probe tip itself; this is the only SNOM mode applicable to opaque samples [2]. The following *fourth* type of approaches is include the “scanning tunneling optical microscope” (STOM)/“photon scanning tunneling microscope” (PSTM) mode [25-28] (see chapter 6 for details). The last SNOM operation mode is “scattering mode” for apertureless NSOM developed by [29-37], and Surface Plasmons (SP) are generated in a thin metallic film on the sample surface by illumination in TIR, leading to a minimum in the

TIR signal (the TIR is attenuated) when the SP resonance is excited. A microscopic probe brought into near-field distance can scatter the SPs giving rise to a detectable change of the TIR attenuation [2]. In Fig. 4 we illustrate different configurations of SNOM.



**Fig. 4** Different modes of SNOM. **a)** SNOM in illumination mode: a dielectric probe illuminates the sample, the light is collected in the far field; **b)** SNOM in collection mode: a dielectric probe collects the light coming through the sample, the sample is illuminated from the far-field; **c)** SNOM in reflection mode: a dielectric probe illuminates the sample, the radiation reflected off the surface is collected either by far-field optics, or by the probe tip itself; this is the only SNOM mode applicable to opaque samples; **d)** PSTM or STOM : a dielectric probe frustrates the evanescent field at the sample surface, generating waves which propagate in the probe; **e)** PSTM/STOM/SFM: combination of PSTM/STOM and contact Scanning Force Microscope; **f)** SPNM: plasmons are generated in a thin metallic film by illumination in TIR and scattered by the probe tip; the attenuated TIR signal is monitored [2].

Among the many above-mentioned modes of operation, in our laboratory we used the “local illumination and detection” mode for the shear-force topographical and near-field optical investigation of the living cells in their native condition (see in Chapter 4). In addition, the above-mentioned PSTM mode was used with recently developed SNOM sensor based on PMMA plastic optical fiber (see in Chapter 5) In Chapter 3 we will introduce the SNOM instrumentation and all the accompanying preparatory issues concerning SNOM experiments.

## 1.4 Varieties of super-resolution fluorescence microscopes

A great advancement in sub-diffraction optical microscopy has been recently provided by the implementation of far-field techniques that take advantage of specific photophysical properties of fluorescence probes in conjunction with tailored ways of illumination to either achieve direct or reconstructed imaging at the nanoscale [38].

Aside from the dynamic nature of cell domains, revealing their true size and composition requires high-resolution microscopy techniques. In principle, *Förster resonance energy transfer* (FRET) is capable of detecting proximity below the optical resolution ( $\sim\lambda/2$ , where  $\lambda$  is the wavelength of light) since the efficiency of the process depends directly on donor–acceptor distances, typically 1–10 nm. In addition, FRET experiments do not provide information on distances beyond 10 nm, and thus not able on its own to reveal the true size of domains. It should be noticed that in more recent years, time resolved FRET as combined with fluorescence lifetime imaging (FLIM) and appropriate theoretical modelling is providing more depth-inside in the size of nanodomains in both model systems as well as in living cells has been carried out [39].

High-resolution fluorescence microscopy is compatible with live cell imaging, provides excellent spectral contrast and in combination with sensitive detectors allows the detection of individual molecules. Until only fifteen or so years ago, near-field scanning optical microscopy has been the only optical technique able to provide resolution beyond the diffraction limit of light. However, recently developed far-field methods have also demonstrated optical resolution in the nanometer range, not only laterally but also in 3D. Each of the methods is briefly discussed below in terms of their advantages but also limitations. Fig. 5 shows the principles of the four different methods developed so far, with a separation between far-field and near-field approaches [38].

*Stimulated emission depletion* (STED) microscopy was conceptually introduced more than a decade ago by Hell and colleagues and successfully implemented afterwards [40–46]. STED creates a nanometric optical region by first exciting fluorophores to an excited state over a diffraction-limited region using a pulsed laser. A second pulsed laser illuminates the sample with a doughnut-shape like pattern in a wavelength that depletes

the excited state of the fluorescent molecules back to the ground state. Fluorescence is effectively detected only from the hole of the doughnut (Fig. 5 A). The final spot size can be tuned to balance resolution against signal and imaging speed by controlling the power of the depleting laser, and indeed images with a resolution of  $\sim 30$  nm have been reported using this technique [39].

*Saturated structured illumination microscopy* (SSIM) is conceptually the opposite of STED (Fig. 5 B). By using a structured light illumination from two high-intensity power interference beams, most of the fluorescence molecules in the illuminating beams saturate, leaving only small regions unsaturated at the shadows of the interference pattern: the higher the intensity, the smaller the regions [47-50]. The practical resolving power is determined by the signal-to-noise ratio, which is in turn limited by fluorescence photobleaching. In its linear form, SIM can work at lower intensities reducing photobleaching but can provide only a two-fold resolution increase beyond the diffraction limit [39].

The two methods described above allow truly optical resolution at the nanometer scale and can be readily extended to 3D imaging. The resolution in fluorescence microscopy can be increased even further by allowing only a subset of fluorescent molecules to be photoactive at a given time and ensuring that the nearest-neighbour distance between active molecules is larger than the diffraction limit. Methods that make use of this principle are *photoactivatable localization microscopy* (PALM/FPALM) [51, 52] and *stochastic optical reconstruction microscopy* (STORM) [53]. The basic premise of both techniques is to fill the imaging area with many dark fluorophores that can be photoactivated into a fluorescing state by a flash of light. Because photoactivation is stochastic, only a few, well separated molecules “turn on.” Then Gaussians are fit to their point spread functions (PSF) to high precision. After the few bright dots photobleach, another flash of the photoactivating light activates random fluorophores again and the PSFs are fit of these different well-spaced objects. This process is repeated many times, building up an image molecule-by-molecule; and because the molecules were localized at different times, the “resolution” of the final image can be much higher than that limited by diffraction (Fig. 5 C). The main difference between PALM and STORM resides on the type of fluorophores used for photoactivation: PALM relies on autofluorescent proteins, while STORM uses organic switchable dyes

(from the cyanine family). The ascertainable localization accuracy depends strongly on the total number of photons being detected. Especially PALM/FPALM can quantitatively map relative molecular densities with very high localization accuracy over wide fields and in living cells. As already mentioned, these forms of nanoscale image reconstruction methodologies rely on photoswitchable fluorophores, and therefore imaging conditions are consistent with single molecule detection and require so far long acquisition times [39].

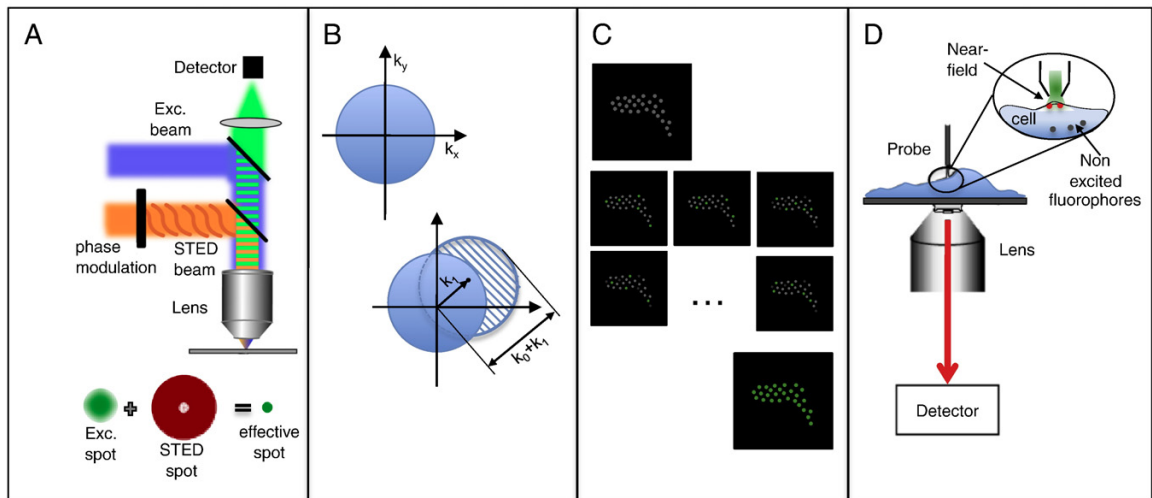


**Fig. 5** Different schemes for super-resolution imaging microscopy. **(A)** Stimulated emission depletion (STED) microscopy. **(B)** Structured illumination concept as introduced by Gustafsson. Top: Circular observable region of radius  $k_0$  in frequency space observed by a conventional microscope. Bottom: New set of information available in the form of moiré fringes (hatched circle) provided that the excitation light contains a spatial frequency  $k_1$ . The new region has the same shape as the normal observable region but it is centered at  $k_1$ . **(C)** Principle of PALM/FPALM and STORM. PALM/FPALM are based on photoactivable autofluorescent proteins while STORM rely on on-off photo switchable organic fluorophores. The techniques use the stochastic photoactivation of single molecules (set to the dark state at the beginning of the experiment as shown in the top panel) and their subsequent nanometric localization over thousands of widefield image frames (series of small panels) to construct a super-resolution image (bottom panel). **(D)** NSOM uses a subwavelength aperture ( $\sim 50\text{--}100$  nm) probe to locally excite the sample surface and to generate point-by-point a super-resolution image related to the size of the probe. Only fluorophores at the cell surface are effectively excited (red dots close to the near-field region) reducing the contribution of background fluorescence from other regions of the cell (dark dots in the interior of the cell) [39].

In its most commonly implemented mode, a subwavelength aperture probe is scanned in close proximity ( $<10$  nm) to the specimen (Fig. 5 D) to generate an image. Using the probe as a near-field excitation source, the interaction with the sample surface induces changes in the far-field radiation, which is collected in the far field by conventional optics and directed to highly sensitive detectors to provide an optical

image. Moreover, another unique characteristic of near-field excitation is given by the finite size of the probe itself: decreasing the area of illumination obviously reduces the interaction volume and background scatter, which is of major importance in enhancing the sensitivity for spectroscopic applications (fluorescence, Raman, etc.) [39].



# Chapter 2

---

## SNOM instrumentation

This Chapter will introduce the design of our home made SNOM, developed for measurements in air and liquid, and important technical issues related to this development. The main purpose of our design was to achieve high-resolution topographical and optical images of living cells in their native condition. In the following sections we will discuss the SNOM instrumentation, operation of the SNOM in liquid, SNOM sensors and the preparation of glass optical fibers using chemical “tube-etching” method with Hydrofluoric Acid (HF). Finally, the SNOM software to manage experiments will be described.

### 2.1 Introduction

In modern science, investigations on a nanometer scale became very common. Characterization and manipulation of individual nanostructures require not only extreme sensitivity and accuracy but also very high spatial resolution [54]. Nowadays SNOM is a well-established research method and there are SNOM devices commercially available on the market. Nevertheless, the general understanding amongst the Near-Field Optics (NFO) community is that all technical and methodical problems are not yet solved. Therefore a lot of researchers still design and construct their own devices rather than buying them [55].

The general aim of such adaptation of SNOM techniques for own scientific purposes rests with achieving a high resolution topographical and fluorescence images, and finding answers to the questions associated with biochemical and biophysical

problem of investigating objects. With respect to these issues, it is extremely important to use a high  $Q$  sensitive SNOM probe/sensor in SNOM related research.

During several years in our laboratory we prepare such SNOM sensors where the main principle is based on double resonant montage of a fiber probe onto the tuning fork (see Fig. 6). “Double resonance” means that the working frequency of the latter coincides with the second resonance frequency of lateral dithering of a free standing part of the fiber, and its advantages have been discussed in details by Cherkun *et al.* in [56]. Such a montage requires careful control of the length of a free-standing part of the fiber beam (for a standard 125 micron-diameter sharpened glass fiber resonance condition holds when it is equal to  $4.8 \pm 0.1$  mm) as well as of the position where thin glass connector between a probe and a tuning fork is to be glued. Cherkun *et al.* showed that this assembly ensures a large quality factor  $Q$  of the sensor: the initial value of  $Q = 10,000 - 11,000$ , which is characteristic for a free unloaded tuning fork in air, drops down to the values of  $Q = 3,500 - 5,500$  after proper gluing of a fiber probe onto it [56].

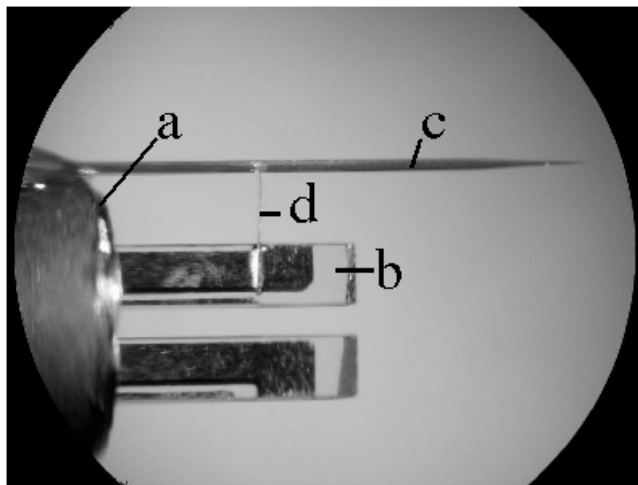


**Fig. 6** Optical probe bonded to the metal case of the tuning fork: (a) Case residue and its end face (b), (c) probe fiber, and (d) drive [56].

To make a stable, easy and well-performing SNOM working in liquid is a long-standing purpose for almost all researchers in the field. This is evidently explained by the very nature of many samples to be investigated. First of all, biological ones (cells and cell fragments, membranes and so on) which normally can not be extracted from their liquid environment without destruction or at least irreparable damage to the

structure and functions. Moreover, these samples usually are rather fragile and easy-to-be-damaged, and therefore require small forces when imaged with a Scanning Probe Microscope [57].

These circumstances complicate the problem a lot, because the quality factor  $Q$  of an electromechanical oscillatory system “sharpened fiber probe glued onto the tuning fork (or other piezoelectric sensor)”, which nowadays is by far the most popular SNOM sensor, rapidly drops after submersion of the fiber probe tip into the liquid, so its usage then necessitates rather large probe - sample forces. Our own measurements performed with different fiber probes simply glued onto one prong of a standard quartz tuning fork with the working frequency of 32 kHz show that an initial  $Q$ -factor, ranging, for such a simple emplacement, from 200 to 500, diminished down to the values of 20 to 40 when the water submersion deepness equals 100 microns or so. Similar data can be found in the literature (to cite only a few of many related papers): when working in liquid, the value of  $Q$  factor around 60 was reported in [58],  $Q = 40$  in [59],  $Q = 20$  in [60],  $Q = 52$  in [61], and  $Q = 300\text{--}600$  we reported in our recent paper (for more details see part 3.3). Of course, for these small  $Q$ -values an appropriate well-designed low-noise electronics still enables to keep the value of an acting force  $F$  at a certain reasonable level, but even with the most sophisticated electronics such a force is in a nanoNewton range. This can easily damage fragile biological samples and often leads to the non-reliable imaging with poor topographical resolution [57]. In addition, the authors from [62] made the SNOM measurements in liquid, and value of  $Q = 35$  with 500 microns in depth.

This partial preservation of the quality factor of the fiber probe is very important—see, for example, [63] where the generally accepted view in the field is quite well formulated: “A sensitive force distance control under liquid seems only feasible if the high quality factor can be at least partially preserved.” For the fiber probes simply glued onto the tuning fork, the quality factor of the sensor in liquid typically attains the values of only 20–60 (our own measurements; see also, e.g., [58, 59, 61], which necessitates the use of large probe-sample interaction forces lying in the nano-Newton range. It is instructive to compare our results with those of other approaches used to preserve a large enough  $Q$ -factor of the SNOM probes working in liquid. For the exploration of short, 3–4 mm in length, fiber probe fragments glued onto the tuning fork [63] and

dithered normally to the sample surface [63, 64–67] the quality factor value equal to 370 was reported [68]. The use of thin fibers holds much promise to be used in liquids, but we are unaware of such studies. At the same time, the general believe is that operation of SNOM in liquids still remains a challenging task where new approaches, ideas and methods are highly desirable [57].

## 2.2 SNOMs sensor and preamplifier

The use of quartz tuning fork resonators has become very popular in a variety of scientific instruments, especially in near field optical microscopes, atomic and magnetic force microscopes, high sensitivity magnetometers, atomic point contact sensors, and spectroscopic gas sensors. The attractive features of this type of sensor are numerous. These resonators are readily available and inexpensive due to their extensive use as frequency control elements in the time keeping industry. They utilize the intrinsic piezoelectric effect in quartz for excitation that can conversely be used for vibration detection of mechanical motion of the tuning fork tines. This avoids the need for optical detection of mechanical vibration, and therefore makes quartz tuning forks effective single component miniature sensors in scanning probe microscopy applications [69].

The advantage of the approach based on the use of the tuning fork is primarily the absence of the need to use any additional light source (a diode laser), whose parasitic illumination is a most important and almost insuperable source of noise in practically all experiments in the field of near-field optical application. What is more, this approach is characterized by low costs, operating convenience, good compatibility with high-vacuum or extra-low temperature conditions, and so on [56].

Quartz tuning forks are also miniature micro-machined devices with large spring constant  $k$ , large mechanical quality factor, and excellent temperature stability, making them attractive force sensors in scientific instrumentation [69].

First, let us consider two literature examples of the use of the tuning fork as force sensors. The photography image of the quartz tuning fork resonator is shown in Fig. 7. The tines of the resonator are  $l=1.6$  mm long,  $w=100$   $\mu\text{m}$  wide, and  $t = 100$   $\mu\text{m}$  thick.

The spring constant of the tuning fork tine  $k$  is:

$$k = \frac{Ewt^3}{4l^3}$$

where  $E$  is the Young's modulus of quartz ( $E = 7.87 \times 10^{10} \text{ N/m}^2$ ). These physical parameters of the resonator result in the effective spring constant of  $k = 480 \text{ N/m}$ . This is one of the smallest reported spring constant of a quartz tuning fork resonator. This value of the spring constant is important, as it falls in the range of optimal values of spring constants for frequency modulated atomic force microscopy instruments [69].

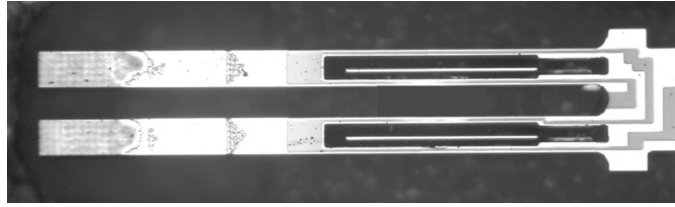


**Fig. 7** Quartz tuning fork resonator. The tines are  $l=1.6 \text{ mm}$  long,  $w=100 \text{ }\mu\text{m}$  wide, and  $t = 100 \text{ }\mu\text{m}$  thick. The spring constant of the tuning fork tines is  $480 \text{ N/m}$  and operating frequency is  $f_{\text{res}} = 32\,763 \text{ Hz}$  [69].

The second important physical parameter of the sensor that relates to its fundamental dissipation properties is the mechanical Q-factor. The equivalence of the mechanical and electronic properties of the quartz tuning fork resonator is well established best measured electronically. The authors used arrangement of a transformer-coupled capacitance compensating circuit, shown in Fig. 8. The center-tapped transformer and tunable capacitor  $C_T$  driven by an AC voltage source, allow for cancellation of the stray parallel capacitance  $C_0$  of the tuning fork resonator, resulting only in the net motional  $L_M C_M R_M$  oscillator. The output of the circuit is coupled to the lock-in amplifier [69].

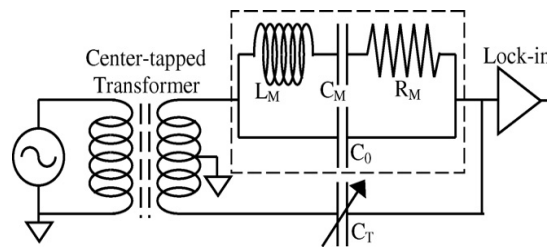


**Fig. 8** Electronic circuit for quartz tuning fork sensor measurement [69].

The frequency response of the  $L_M C_M R_M$  resonator with the parallel package capacitance  $C_0$  nulled is shown in Fig. 9. The response, shown in the measured data points, follows very well the expected Lorentzian line shape response fit also shown in the figure. From the fitted curve, they deduce the quality factor value of  $Q=27,500$  in a vacuum packaged environment, with the center frequency of  $f_{\text{res}} = 32\,763$  Hz. The measured equivalent motional capacitance, inductance, and resistance values are:  $C_M = 3.4$  fF,  $L_M = 6.94$  kH, and  $R_M = 51.95$  k $\Omega$  [69].

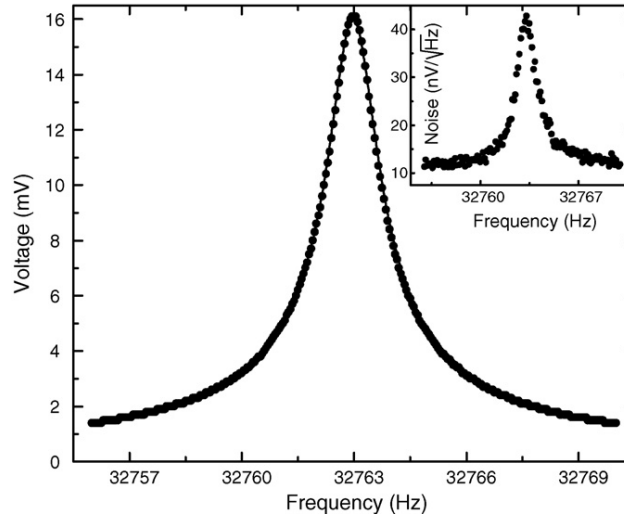


**Fig. 9** Measured frequency response of the quartz tuning fork resonator (data points) with the nulled parallel capacitance  $C_0$ . The Lorentzian line fit with  $f_{\text{res}} = 32,763$  Hz and  $Q = 27,500$  is shown through the data points. The inset shows the noise spectrum of the quartz tuning fork resonator. The resonator force sensitivity is limited by the fundamental thermo-mechanical vibrations at room temperature [69].

In our SNOM, we used an original electronic circuit for measuring the resonance frequency and the quality factor of the tuning fork +cantilever system, based on the active compensation of the stray capacitance, and a specially designed low-noise current source. An important feature of the transducer is the use of the high quality factor  $Q$  of such a system: the inherent high  $Q$  of the tuning fork is reduced but insignificantly if a light cantilever is accurately glued to one of its prongs. A much more difficult task is to optimally couple the tuning fork to a relatively heavy optical-fiber probe. Such a probe glued to one of the tuning fork prongs typically reduces the quality factor of the system to some 300–1000, which substantially impairs the sensitivity of the transducer [56].

To solve these problems, Cherkun *et al.* [56], suggested and realized a new tuning

fork+optical-fiber probe system relying on the coincidence between the resonance frequencies of the fork and the probe tip and using a thin “drive” to couple the probe to the fork (see Fig. 6). This probe attachment method makes it possible to retain the high quality factor characteristic of the tuning fork, eases the assembly of the transducer, and also provides for an additional twofold gain in sensitivity [56].

When the probe is glued directly to a prong of a tuning fork, the quality factor of the latter decreases from 10 000–14 000 to 300–1000, which strongly affects its sensitivity. To avoid this shortcoming, we selected the probe length from its attachment point on the tuning fork case to the tip point at  $4.8 \pm 0.1$  mm, having experimentally verified that this probe length corresponds to the probe dithering resonance at a frequency close to 32 756 Hz. In that case, the probe vibrates with the amplitude presented in Fig. 10 as a function of the probe length. This is a theoretical curve obtained numerically by formulas presented in Ref. 2 for a pointed fiber with a diameter of  $d=0.125$  mm. With the probe fiber being 4.8 mm long, there is a vibration node at a distance of  $l_{\text{node}}=3.34$  mm and an intermediate maximum at a distance of  $l_{\text{max}}=2.01$  mm. The point  $l$  indicated in the figure corresponds to the resonance frequency of a fiber having no pointed end. For such a fiber, the ratio between the vibration amplitudes at the point  $l_{\text{max}}$  and at the probe end is around 1.39. For a pointed fiber, this ratio is approximately equal to 2.17 [56].

For the attachment point of the drive  $d$ , we selected the point  $l_{\text{max}}$  of the vibration maximum. Obviously with this attachment the vibration amplitude of the pointed probe tip is greater than that of the tuning fork prong by approximately a factor of  $M=2.17$ . An experimental check has shown that with this probe attachment method the shift of the tuning fork resonance frequency is in the range of  $\pm 100$  Hz. The quality factor ranges between **3000** and **7500** and is governed mainly by losses at the point of attachment of the probe to the tuning fork case [56].

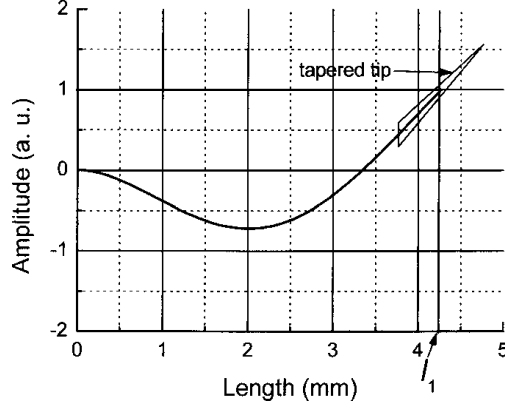


Fig. 10 Shape of the probe fiber bending vibration (mode  $n=1$ ) [56].

In order to clarify the meaning of “double-resonance” principle of our SNOM sensor, let us briefly review calculations of authors in Ref-s [56, 63].

The analysis of this sensors based on refining the coupled harmonic oscillator model of the tuning fork-based transducer earlier presented in [63], is given in [56]. The authors took into account the attachment of the probe to one of the tuning fork prongs as the increase  $\Delta m$  (also as  $-m_{fb}$ ) of the effective mass  $m$  of one of the coupled oscillators and arrived to the following equations describing the frequencies [56].

The force  $F(t) = F_0 \exp(-i\omega t)$  represent the external excitation of the tuning fork with the angular frequency  $\omega$ . For the complex time-dependent amplitudes  $z_1(t)$  and  $z_2(t)$  of the eigenmodes  $Z_1$  (antisymmetric) and  $Z_2$  (symmetric) the following expressions can be obtained:

$$\ddot{z}_1 + \omega_1^2 z_1 + \delta \dot{z}_1 + p \ddot{z} = 0$$

$$\ddot{z}_2 + \omega_2^2 z_2 + (\beta + \delta) \dot{z}_2 + p(\ddot{z}_1 + \beta \dot{z}) = \frac{F(t)}{m(1+q)}$$

Then authors in [56, 63] introduced the following parameters:

$$q = \frac{\Delta m}{2m}, \quad p = \frac{q}{1+q}, \quad \delta = \frac{\gamma}{1+q}, \quad \omega_{10}^2 = \frac{k}{m},$$

$$\varepsilon = \frac{k_{fb}}{2m(1+q)}, \quad \omega_1^2 = \frac{1}{(1+q)} \omega_{10}^2, \quad \omega_{20}^2 = \frac{k+2\alpha}{m}, \quad \omega_2^2 = \frac{1}{1+q} \omega_{20}^2.$$



Applying the substitutions  $z_1(t) = z_{11} \exp(-i\omega t)$  and  $z_2(t) = z_{21} \exp(-i\omega t)$ , the differential equations turn into a system of linear equations for  $z_{11}$  and  $z_{12}$ . For the complex amplitude  $z_{11}$  one arrives at:

$$z_{11} = \frac{\left[ p\omega^2 \frac{F_0}{m(1+q)} \right]}{\left\{ (\omega_1^2 - \omega^2)(\omega_2^2 - \omega^2) - \delta(\beta + \delta)\omega^2 - p^2\omega^4 - i\omega[(\beta + \delta)(\omega_1^2 - \omega^2) + \delta(\omega_2^2 - \omega^2) + p^2\beta\omega^2] \right\}}$$

and the ratio of the amplitude  $z_{11}$  and  $z_{12}$  becomes:

$$\frac{z_{11}}{z_{21}} = \frac{p\omega^2}{\omega_1^2 - \omega^2 - i\omega\delta}$$

For small damping constant  $\beta$  and  $\gamma$ , which can always be assumed in our case, the amplitude  $z_{11}$  can be approximated with Lorentz curve. Ignoring the damping terms, the eigenfrequencies  $\omega_{11}$  and  $\omega_{12}$  can be approximately calculated to be equal [63]:

$$\omega_{11,21} \approx \sqrt{\frac{1}{1+p} \left( \frac{\omega_{10}^2 + \omega_{20}^2}{2} \pm \sqrt{\left( \frac{\omega_{10}^2 - \omega_{20}^2}{2} \right)^2 + p^2\omega_{10}^2\omega_{20}^2} \right)}$$

Especially for a small  $p$  the resonance frequencies can simply be written as  $\omega_{11} \approx \omega_1$  for  $Z_1$  and  $\omega_{21} \approx \omega_2$  for  $Z_2$  [63]. Therefore, from  $\omega_1^2 = 1/(1+q)\omega_{10}^2 + \varepsilon$  and  $\varepsilon = k_{fb}/2m(1+q) + \varepsilon$ , it follows that in our system one can achieve *exact* coincidence between the frequencies  $\omega_{10}$  and  $\omega_1$ , which explains why probe attachment method can be so effective. At small  $q$  values, such coincidence takes place when  $k_{fb}/m_{fb} = k/m$ , that is, when the *double resonance condition holds* [56].

The large quality factors of the probe enabled us to use the proprietary, low noise, precise and fast electronics measuring the resonant frequency  $f_{res}$  and  $Q$ -factor of a tuning fork, earlier exploited for the “tuning fork and AFM cantilever glued upon it” (to achieve large  $Q$  for that sensor does not pose a serious problem) and discussed by Serebryakov *et al.* in [70]. Both  $f_{res}$  and  $Q$ -factor related signals have a form of DC voltage ranging from -10 V till +10 V and hence are quite suitable for easy use as a feedback source [57].

The large force sensitivity of the sensor (8 pN rms in the 300 Hz frequency band) and excellent topographical resolution attained with it were discussed in ref. [56]. We also would like to underline the possibility of a fast scanning with this SNOM: to scan a flat area of 300 x 300 nm in size (128 x 128 points are collected) takes only ca. 15 seconds. Such a fast scanning can be attained due to the peculiarities of the feedback detection scheme, which exploits high quality factor sensors and measures their resonance frequency and losses ( $Q$ -factor value) rather than the dithering amplitude (so called “dynamic force scanning probe microscope”). Different aspects of this problem (among others, the dependence of the scanning speed on the sample roughness), which is evidently important for all branches of the Scanning Probe Microscopy technique, have been profoundly discussed in the literature (see e.g. [70] for review). For illustration in Figs. 11 and 12 we present two images obtained with this SNOM [57].

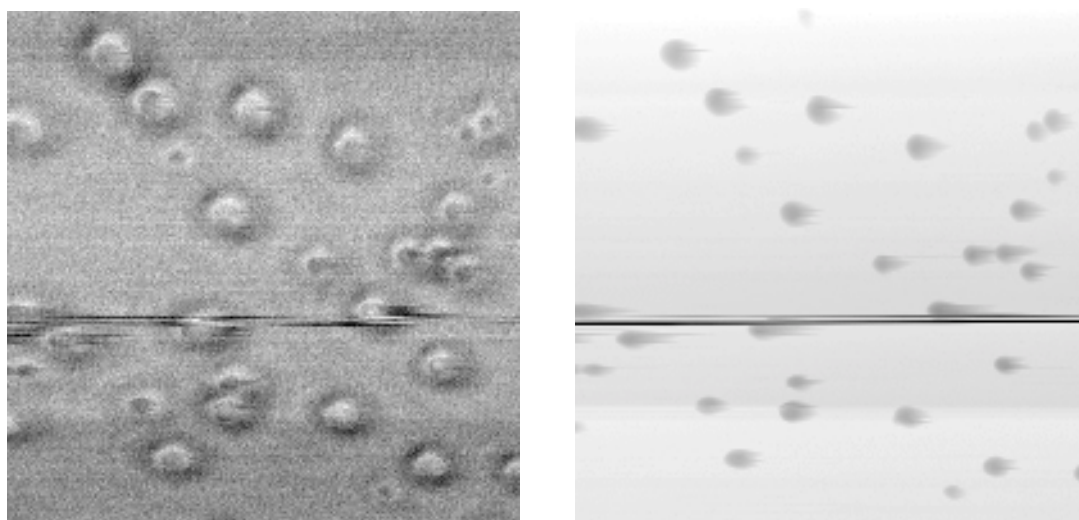


**Fig. 11** Near-field optical fluorescent (left) and shear-force topographical (right) images of OM57 dye molecules [47] deposited onto the glass slide surface by simple drying from the droplet. Scan size 2 x 2 microns, maximal height of the spots in the topographical images, which are nothing else than hills composed by different sort of dirt stained with the dye molecules, is around 20 nm. Note, how well such images imitate “single molecule SNOM images”, cf. e.g. the cover of *Journal of Microscopy*, 194, parts2/3, May/June 1999, Proceedings of Fifth International Conference on Near field optics and related techniques, Shirahama, Japan, 6-10 December 1998, and many other papers [57].

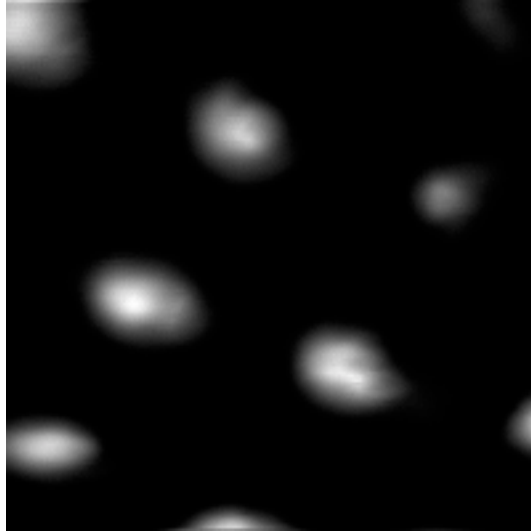


**Fig. 12** Near-field optical image (illumination mode, cw Ar-ion laser line at 488 nm is used) of ca. 200 nm-diameter holes made in 200-nm thick gold film onto the glass slide surface by electron beam etching technique. Scan size: 2 x 2 microns. Sample courtesy of Dr. I. Utke, EPFL [57].

### 2.2.1. Sensor's preamplifier

In ref. [56] the authors have suggested that the improvement of the SNOM sensor sensitivity can be explained proceeding from the law of the conservation of energy. The authors operate the TF in conditions where the amplitude of the current  $I$  through the TF remains constant (see Fig. 13). The current is proportional to the velocity of the vibratory motion, and so it uniquely defines the vibration amplitude. The voltage of amplitude  $V$  developing across the TF is proportional to the loss of energy in the vibratory system. The electric power  $P=VI$  fed to the tuning fork compensates for this energy loss to maintain the vibration amplitude constant [56].

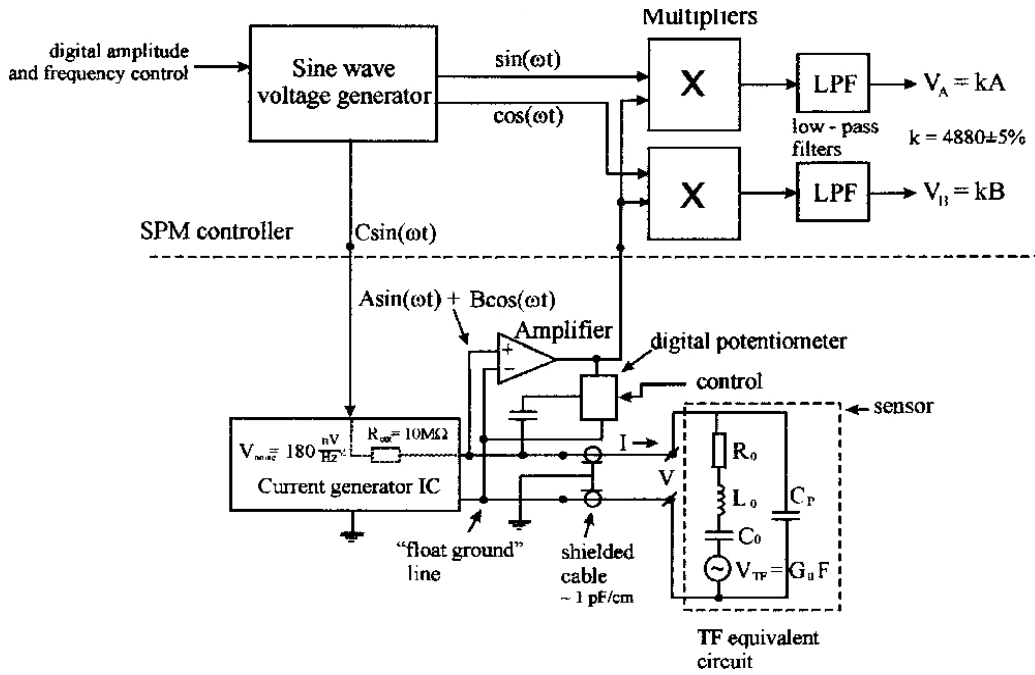


Fig. 13 Circuit diagram of the transducer [56].

This circuit uses an improved sine-wave voltage generator with a signal/noise ratio of not less than 130 dB in the operating band of the transducer, which makes its contribution to the total noise of the system but little perceptible. The frequency adjustment accuracy of the generator is not worse than 0.002 Hz. Another and most important difference from the usual circuit used is the exploration of a special microchip current generator with a “floating ground” instead of the plain resistor. It operates so that its output resistance between the output terminal and the floating ground amounts to 10 MΩ and is close to zero between the output terminal and the common wire. This makes it possible to connect the tuning fork to the electronic circuit by means of two shielded cables, whose capacitance will in that case not affect its operation in the first approximation the capacitance of the cables affects the noise level of the system if it is over 7 pF, and should such be the case, the noise level will rise linearly with increasing cable capacitance. The noise produced by the current generator is less than that of an equivalent 10 MΩ resistor and comes to 180 nV/√Hz [56].

The voltage at the output terminal  $V_A$  is proportional to the force applied to the tuning fork in phase with its vibration velocity and that at the terminal  $V_B$  is proportional to the force in phase with the tuning fork displacement. The vibration

amplitude of the tuning fork is directly proportional to the current through it, and for the tuning forks used by authors the coefficient of proportionality amounts to 0.35 m/A [56].

To evaluate the sensitivity of transducer, authors placed the tungsten wire probe in parallel with an electrode (Fig. 14) with a controllable potential  $V_e$  applied to it. The electrode is fixed to the scanner of a probe microscope, so that it can be moved relative to the probe. The probe is grounded. The amplitude  $C$  of the signal produced by the sine-wave voltage generator tuned to resonate with the tuning fork is selected such that the amplitude of the voltage  $V_{TF}$  across the tuning fork terminals equals 4 mV. At resonance, the voltage at the output terminal  $V_B$  is also equal to zero [56].

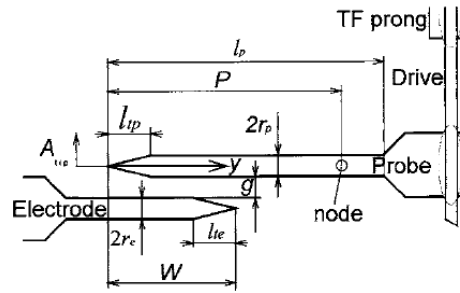


**Fig. 14** Relative position of the probe and electrode in verifying the mechanical amplification of the transducer [56].

When a voltage is applied to the electrode, an attractive force develops between it and the probe. This force contains a constant component (to which the transducer is insensitive) and a variable component due to the variation of the gap  $g$  (Fig. 14) as a result of the probe vibration. Since this force is in phase with the tuning fork displacement, it gives rise to a nonzero component,  $B \cos(\omega t)$ , in the voltage across the tuning fork terminals that is proportional to the applied force. The coefficient of proportionality may be represented as the product of the constants  $G_0$ , determining the coefficient of conversion of the force applied directly to the tuning fork into the voltage across it, and  $M$ , determining the mechanical amplification of the transducer [56]. In the next section we will discuss about technical aspects in details of preparation of SNOM sensor, that currently in use for our measurements.

## 2.3 SNOM sensors fabrication

Already several years in our laboratory we fabricate SNOM sensors based on double-resonance principle. Among other currently available SNOM sensors, they have several distinctive advantages, such as high Q-factor and relative ease of fabrication (all steps tooks  $\sim 2$  hours). Moreover, these advantages of the SNOM sensors allow work in different environmental conditions (e.g. in both air and liquid media).

The method consisting of the use of “quartz tuning fork + glass optical fiber” was first proposed by Karrai and Grober in 1995 [72, 73], showing great potential for near-field optical applications as powerful SNOM sensor. Later on, in 2006, Cherkun *et al.* [56], have proposed a similar, but a bit more advanced version, consisting of “tuning fork + optical fiber probe + thin drive” to prepare the SNOM probe (see Fig. 6). Experimentally we have verified that this montage is both promising and advantageous. Therefore, we have adopted this fabrication technology, and almost all experimental data of present thesis were obtained with these sensors.

The fabrication of SNOM sensors starts with a careful removal of the metallic part of the tuning fork (TF) (the top side of the metallic cylinder)(32 kHz quartz tuning fork, Farnell Components). After the cutting process, the next step is to check the viability of the TF, and then to quickly sold (due to the high temperature of the “solder tip”  $\sim 400^\circ\text{C}$ , there is a high risk to melt the internal structure of TF) on the “aluminum square plate” with two isolated metallic wires. The additional third metallic wire was soldered before on the backside of the aluminum plate and will be used as “ground” for the sensor. The control test was carried out for each probe afterwards. Finally, if the Q-factor were high enough (between 3000-5500), we would proceed to the near-field optical measurements.

For preparation of SNOM sensor it is necessary to follow carefully all technical steps. The preparation steps are as follows: the *first* step is to attach in parallel the metalized sharp optical fiber (with tip apex radius curvature of 50-80 nm and 125 microns in diameter supplied by Veeco) onto the external side of the cylinder of a TF. After that, precisely adjust  $4.8 \pm 1$  mm of total length of the fiber in a way that the apex of the fiber should be directed outwards, and then glue it onto the metallic cylinder.

The *second* step is to glue a thin glass “drive” (the diameter is  $\sim 20$  microns), between glued optical fiber and one prong of the TF at distance of 2.01 mm. Finally the *third* step is to carefully cut the thin glass, drive which is out of the glued point.

For topography scan we use home-made uncoated glass optical fibers (3M), which can be easily reproduced. The details of chemical etching process of fibers are given in Appendix I.

Another parameter that influences the Q-factor is the brand of the glue. In our laboratory we use adhesive epoxy glue (UHU plus, Switzerland), where the drying takes 1 hour. Experience shows that almost in 2 hours (including above mentioned 3 steps) we can obtain a finished version of SNOM sensor with high reproducibility. Finally, the typical Q-factor that we achieve ranges between **2500-5500**.

For the gluing purposes, we have constructed an assembly of three independent XYZ translation stages. The *first* stage holds the metalized optical fiber in appropriate position with a possibility of freely rotating it along the XYZ axes. The *second* stage is made for holding the metallic plate of SNOM sensor with a possibility to rotate it along the XYZ axes. On the *third* stage, we mounted the “cutting mechanism” to cut the small connecting fiber after drying (see Fig. 6, d)). This stage can be displaced along the XYZ axes as well. In Fig. 15 we illustrate the technical features of this 3D mechanical system for gluing SNOM sensor.

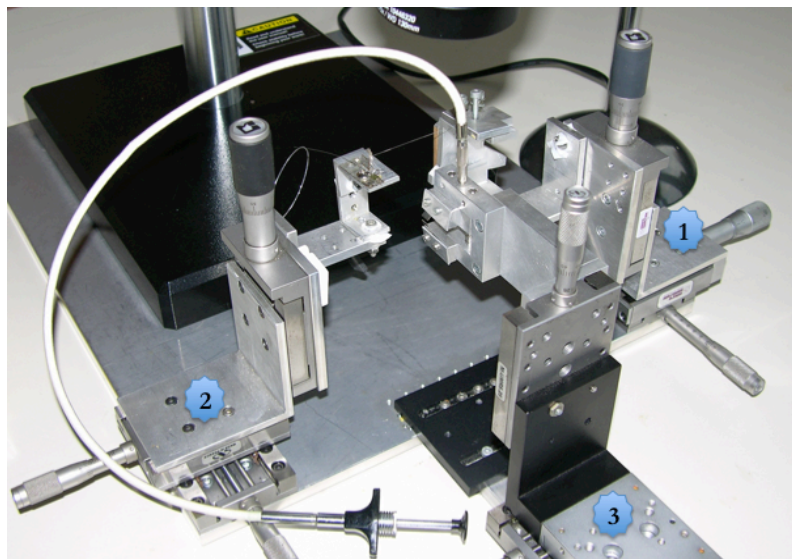


**Fig. 15** The technical features of this 3D mechanical system for gluing SNOM sensor. Where 1<sup>st</sup> is fiber holder stage, 2<sup>nd</sup> is metallic plate holder and 3<sup>rd</sup> stage is “cutting mechanism” for cutting small drive (see Fig. 6, d)).

## 2.4 Installation of the scanner head onto the inverted optical microscope

In order to perform SNOM experiments in liquid, we installed the SNOM scanner head onto the inverted optical microscope Carl Zeiss Axiovert S 100 (Carl Zeiss, Germany), for operation in “transmission mode” and to work with living cells. The microscope has two external ports for the fluorescence detection: the *first*, situated on the top side, gives 100% of optical output, and the second, placed on the left side, gives 70%. The objectives (40x/0.65 (A-PLAN) and 60x/0.95 (A-PLAN) (Carl Zeiss, Germany)) were used for SNOM observations of living cells. Since the argon-ion laser is positioned far from the microscope, we used several external mirrors to introduce the laser light into the optical fiber via fiber-coupler with objective 100x/0.90 (A-PLAN). The optical signal was detected using the Photo-Multiplier Tube MP-942 (PMT, Perkin Elmer, Germany) (see in 2.6). In Fig. 16 we present the photography illustrating the technical overview of present SNOM in liquid.

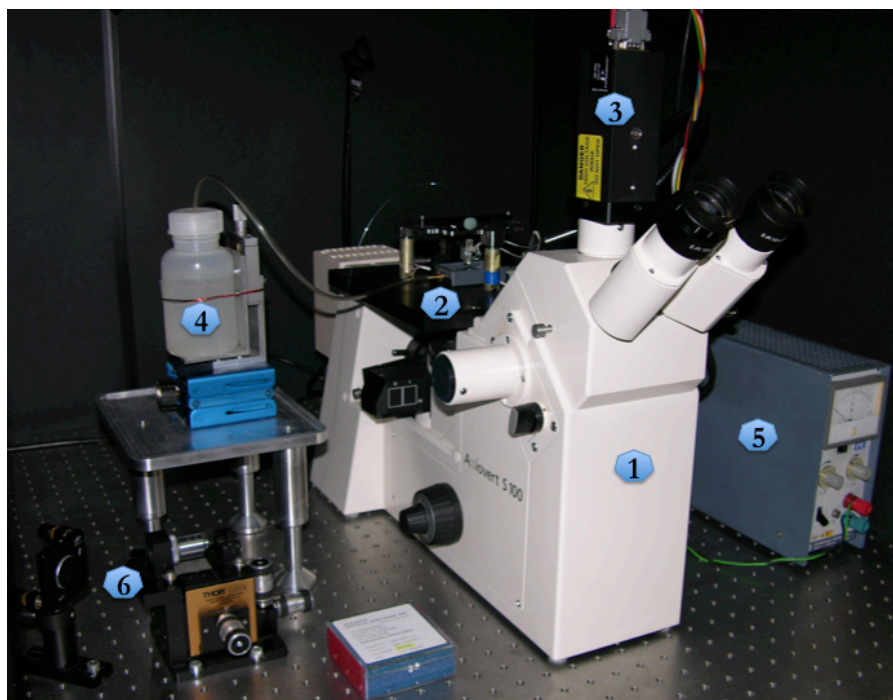


**Fig. 16** Photography of the SNOM in liquid with following parts: 1) Inverted Optical microscope; 2) scanner head with piezo-cylinders and sample holder; 3) Photo-multiplier tube with filter set on the bottom; 4) the external water reservoir with translation stage for “Joint recipient method”; 5) power supply for PMT and 6) the mirror with fiber coupler for collecting laser light into the optical fiber.



## 2.5 XYZ piezo-cylinders

XYZ piezo-cylinders (scanner head) (Institute of Spectroscopy, Academy of Science, Troitsk, Russia) were mounted onto the sample holder of the inverted optical microscope. The principle of “stip and slick” motion was used for the micron scale XYZ displacement of the SNOM sensor. The scanner head has three piezo-cylinders for the XY movements, and one more for the Z movements. The largest scanning sizes of these piezo-cylinders are 35 microns for XY and 5 microns for the Z directions [57]. A metallic plate with a square hole in the center was made for the installation of all piezo-cylinders. These features allowed us to work in transmission mode of the SNOM, and freely move the “sample holder” with “cell chamber” along Z-axis (see Fig. 17). The SNOM sensor was hold by a “T shaped” holder and placed onto the three XY piezo-cylinders, and then adjusted to the center in a way that tip of the SNOM probe is centralized along the axis with microscope objective. To illustrate this, in Fig. 17 we present the photography of the XYZ piezo-cylinders and “scanner head” of the SNOM used for investigation of living cells in liquid.

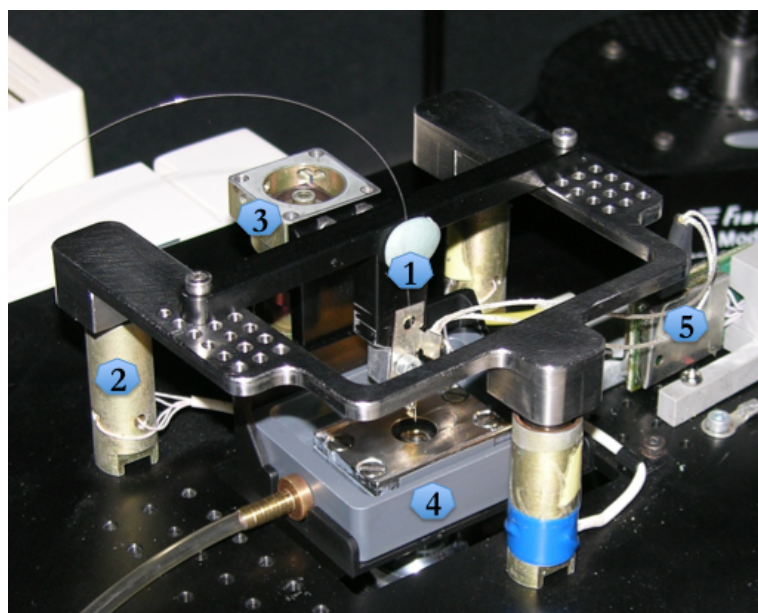


**Fig. 17** The photography of the XYZ piezo-cylinders of our SNOM in liquid. Here 1) is the “T shaped fiber holder” with mounted SNOM sensor; 2) the XY piezo-cylinders mounted onto the plate; 3) the Z piezo-cylinder with cell chamber holder; 4) the “cell chamber” with flexible polymer tube for water delivering and 5) the small preamplifier for the SNOM sensor.

The tip-sample approach was divided in two stages: The *first* is the careful mechanical approach, and the *second* is an automatic approach by “UsScope”, the SNOM software program (Institute of Spectroscopy, Academy of Science, Troitsk, Russia) (see in part 3.7). Once the tip touches the surface of the sample, the program instantly hinders the approach and “feedback control” system keeps the constant value that was given by the program.

## 2.6 Lasers, filters and photon counter detector

In order to detect the SNOM optical signal, we used Argon-ion, HeNe and Nd:YAG lasers for the near-field optical experiments. The argon-ion laser (Spectra Physics, Stabilite 2017) can be tuned to several wavelengths such as 488 nm and 514 nm, with total power of >4.4 W. Another laser that we also used was HeNe laser (JDS Uniphase), with the wavelength of 633 nm and a total power of ~5 mW. We also used a cw Nd:YAG laser at 532 and 1064 nm wavelengths, with an acousto-optical modulator to prepare laser pulses with the duration of 10-100  $\mu$ s.

The collected light from the sample was detected using the MP-942 Photo-Multiplier Tube (PMT, Perkin Elmer, Germany). It is important to notice, that there are several features of our PMT, which makes it suitable for single photon detection in the spectral range 165-650 nm, with the quantum efficiency equal to 20% at maximum. Low noise level (10 dark counts per second), and high sensitivity facilitate detection of low light levels.

To filter noise and pass the fluorescence signal, in same case we used four types of Holographic Notch filters (Kaiser Optical Systems, Inc., USA) for wavelengths of 488 nm, 514.5 nm, 532 nm and 632.8 nm respectively. According to the chosen laser wavelength we put appropriate filter at the entrance of the PMT.

## 2.7 Electronics unit of the SNOM

The general scheme of the microscope electronics is presented in self-explanatory Figure, section Electronics (see Appendix II). It is composed of 1) an interface PCI-card to be inserted into an appropriate slot of a modern Pentium PC, 2) a separate electronics block which comprises a signal processing board, a sensor board and HV amplifiers to operate the scanner, and 3) a small preamplifier placed close to the sensor and connected with it by a short (no more than 30 - 50 cm; for longer cables the compensation of stray capacitance becomes ineffective) coaxial cable. Electronics of this SNOM uses a digital feedback algorithm based on the sum of three signals: an error signal (difference between the set point of a sensor and its current value), its integral of this signal with a time constant preselected by user (typically 0.5 - 5 ms), and its differential; amplification factors of these signals and summation coefficients can be changed in a broad region. Feedback scheme includes a special option reacting on any abrupt and hence potentially dangerous change of a sensor signal by rapid disengagement of a probe from the sample surface. Built-in dynamic protection system prevents the piezoceramic overheating and short circuit of the high voltage part of the electronics [57].

Electronics of the microscope could be used separately from its head with other scanners and optical microscopes. If necessary, other sensors and preamplifiers also can be used. Additionally, our electronics also enables to realize pulse detection of the optical signal with the resolution of 25 ns. This option is described in details in [39], where we present experimental near field optical images demonstrating improved signal-to-noise ratio obtained with it. Finally, we would like to mention the following peculiarity of our microscope: each time when the  $x, y$  position of the probe changes, its electronics generates a standard short TTL pulse which can be used to switch on/off external detectors. This option, which is often neglected when designing a Scanning Probe Microscope, proved to be really useful when combining the microscope with a modern CCD camera (“brightness amplifier”) such as Pentamax or other [57].

## 2.8 SNOM software

In our laboratory we use custom software – “UsScope” (Institute of Spectroscopy, Academy of Science, Troitsk, Russia) (see Appendix IV) developed for nanoscale manipulation of the SNOM scanning head including the XYZ piezo-cylinders and SNOM sensor. As the standard Scanning Probe Microscopy (SPM) program, it has general options like: a) “scan size”, where the total scanning size can be set for XYZ parameters; b) “scan offset”, where the managing parameters can be generated within managing different parameters; c) “scan window”, where the measurements are registering in real time, and so on. For analysis and processing of obtained topographical and near-field optical images, we use commercially available SNOM software “FemtoScan” (Advanced Technologies Center, Russia) (see Appendix III). This program has a bucket of useful options for processing raw images with detailed analyzing in 2D and 3D. All the experimental images presented here were prepared with this software.

## 2.9 SNOM operation in liquid

The prerequisites favorable for this SNOM to work in liquid were discussed in the section 2.1. Its stable work in liquid has been attested experimentally using the set-up presented schematically in Fig. 18 [57]. Our experience showed that the quality factor of the probe rapidly decreases when the end of the fiber tip is immersed into the water. After the very point of the probe touches the water surface,  $Q$ -factor drops down abruptly and in a rather uncontrollable fashion, hence we were unable to quantify this particular drop. Upon the subsequent immersion, however, the decrease of  $Q$  becomes roughly a linear function of the depth and is sufficiently reproducible. Experimentally, we determined that the initially large  $Q$ -factor around **3500–5500**, which is characteristic for our probes, drops down to the values around **300-600** when the depth attains the value around **0.3 mm**.

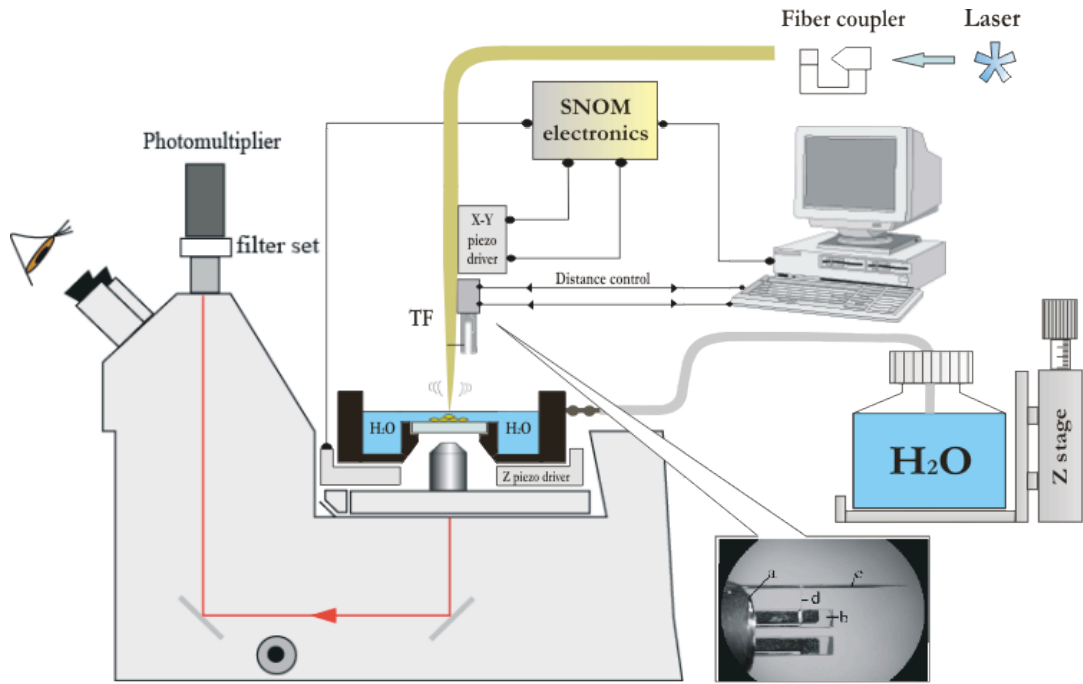
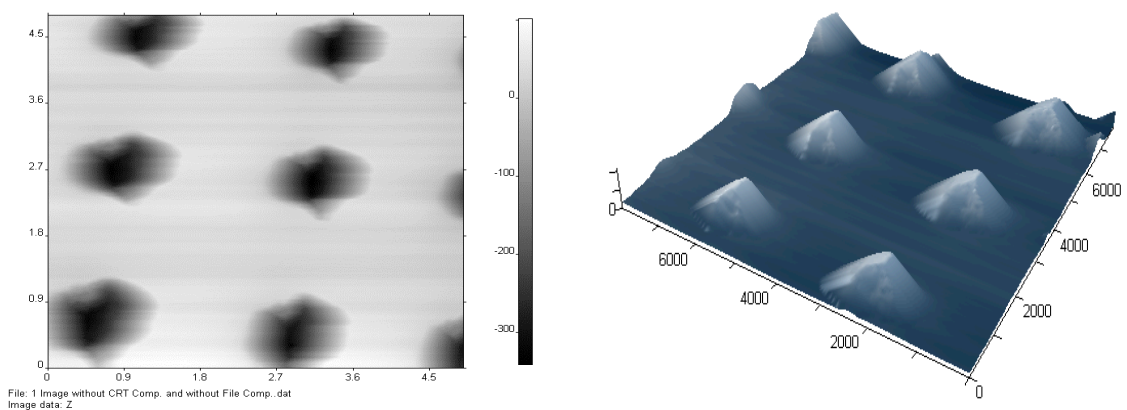


**Fig. 18** SNOM operation in liquid. The level of the liquid and the fiber probe immersion depth are fixed by the proper positioning of an additional external water reservoir shown at the right part of the figure (out of the scale). Afterwards the tip-sample contact is engaged automatically without influencing the probe immersion depth until the contact is reached; see text for further explanations. Double resonant assembly of the sharp fiber probe *c* onto the tuning fork *b* is shown in the inset: *a* is metallic case of the tuning fork, *d* is thin glass rod [68].

Our electronics [56, 70] still works reasonably with a minor modification for such probe parameters, but further decrease of the quality factor is undesirable both from the viewpoint of a proper functioning of the electronics and rapid increase of the acting probe – sample force. Hence the depth of the water layer at which the fiber probe tip is submerged should be kept equal to **0.2 - 0.3 mm**. This was easily achieved using an additional simple construction enabling to regulate the level of the liquid in the water cell by connecting it with a large external water reservoir via a flexible tube (see Fig. 18). This external reservoir is placed onto an additional Z-translation stage so the level of liquid there can be regulated by vertically moving this stage. Due to the “*joint liquid recipients*” principle and because the quantity of a liquid in an external reservoir and its surface are much larger than those values characteristic for the liquid cell, this vertical movement of the cell almost does not influence the level of liquid in this cell. Hence the liquid level and the sample Z-coordinate are independent; after the desirable submersion depth of the fiber probe is set by positioning an external water reservoir at

the proper height, the position of a probe (and correspondingly the submersion depth) did not change any more while the sample-tip contact is engaged using a built-in standard automatic approach option applied to the liquid cell. As far as we know, somewhat analogous idea has been occasionally tested for SNOM working in liquid [61] but up to now it is not broadly accepted [57].

When using this *“joint recipients construction”*, operation of the Microscope in water proved to be quite easy using both feedback channels, and this was tested with numerous samples having different characteristics. To illustrate the operation of this SNOM in liquid in Fig. 19 we present the shear force topographical image of the TGT 01 calibration grating, NT-MDT Company, Russia, imaged under the  $\sim 0.3$ -mm thick water layer. This same grating was imaged in air (Fig. 19 **a, b**) so that images can be directly compared. The quality of both images appeared to be the same. Fiber (uncoated and home made) used to image in liquid was a bit sharper than that used to image in air. That explains apparently sharper peaks in Fig. 19 (**c, d**). Based on known force sensitivity and noise level of our electronics [56], as well as on the quality factor of the probe in liquid, we can estimate an achievable acting force as ranging from 200 to 300 pN (which is comparable to the force around 300 pN reported for the diving bell method in [71]), hence quite suitable for imaging soft samples [57].



**a**

**b**

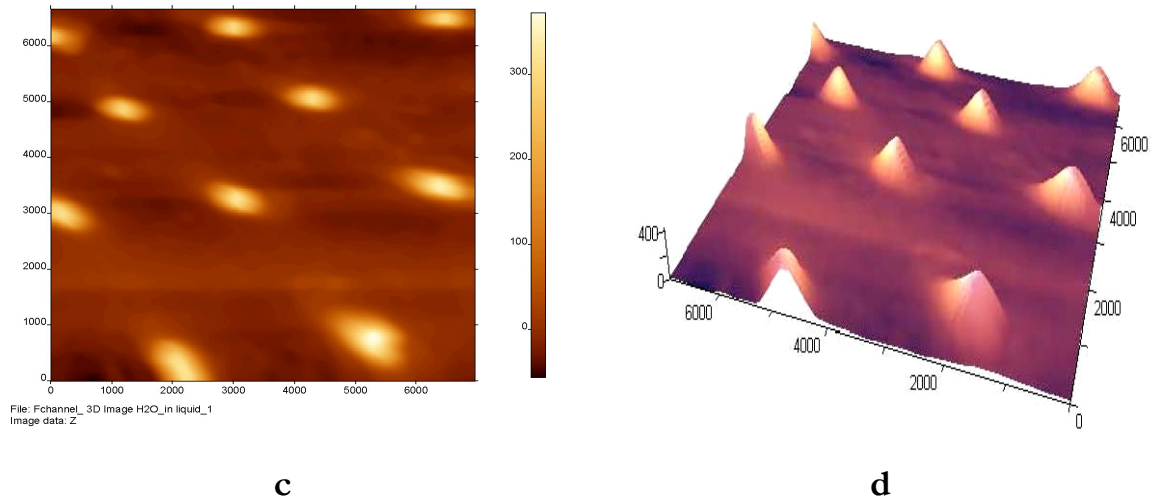


**Fig. 19** Shear-force topographical images of the TGT 01 calibration grating (NT-MDT, Russia), obtained in the **air**: **a)** 2D and **b)** 3D reconstruction; and in the **liquid** environment, of the same calibration grating under 0.3 mm layer of water: **c)** 2D and **d)** 3D reconstruction. Scale is given in nanometers. Grating period: 2.12 microns, tip height: 0.3 – 0.5 microns. Image is given without the scanner non-linearity correction.

Since our work of microscope in liquid has been established we, prior to the study of the living cells, proceeded to imaging the Polystyrene microspheres (Polysciences Inc., USA), with diameter of 2.0 microns in air and in liquid. The results show that images obtained in liquid demonstrate a shape close to the original shape of the microbeads [see Fig. 20, **c)** and **d)**], compared to the a) and b) of Fig. 20, which looks as if the beads were deformed by pressure. The same features are seen in the Fig. 19 **c)** and **d)**.

In Fig. 20 we present shear-force topographical images of the homogenous monolayer of Polystyrene microspheres in the air and in the liquid environment. For the experiment in liquid, we have done the same SNOM manipulations as in the case of “calibration gratings”, and the level of the water was kept at the same level of ~0.3 mm in depth.

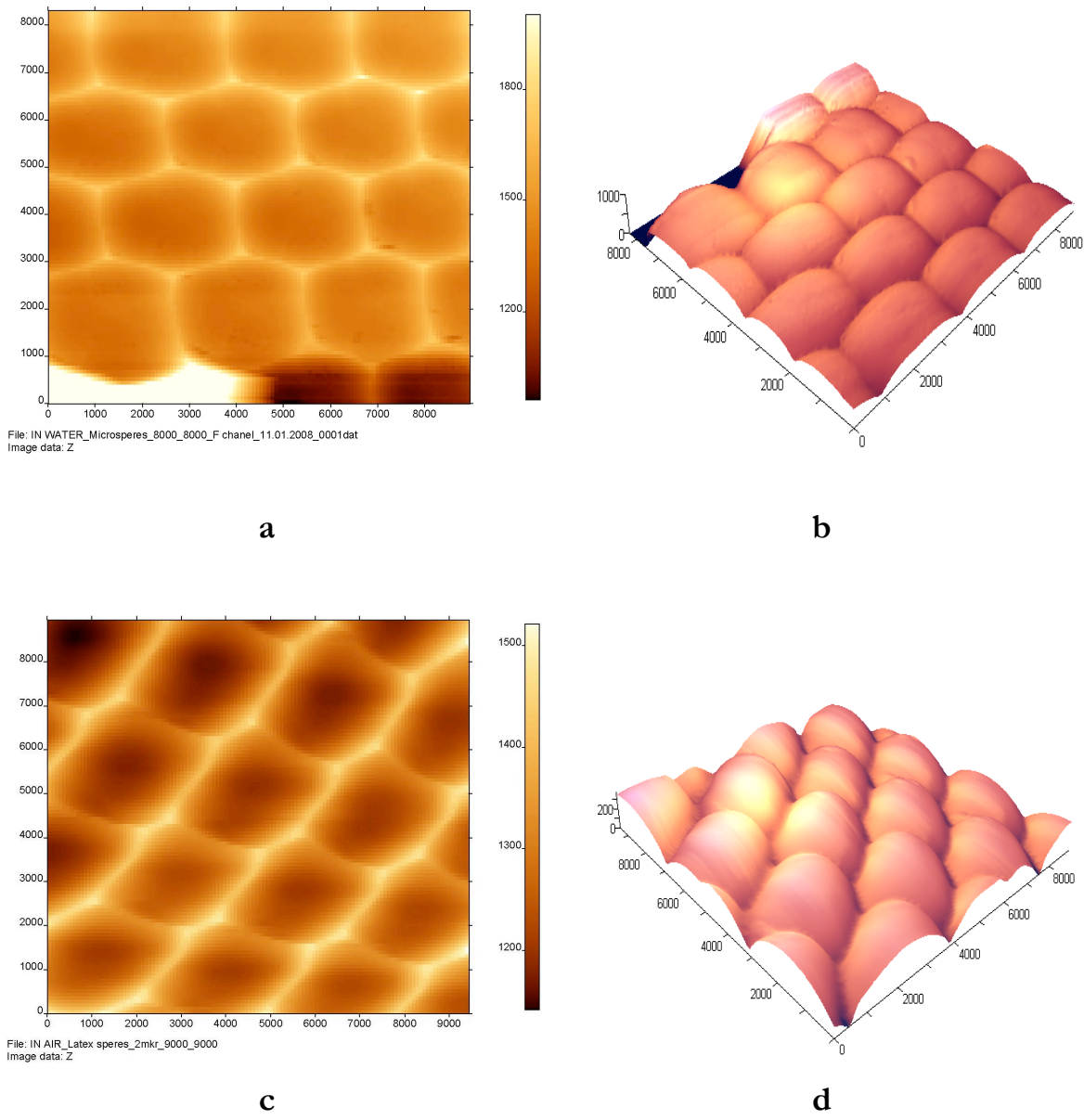


**Fig. 20** Shear-force topographical images of the Polystyrene microspheres, obtained in the **air**: **a**) 2D and **b**) 3D reconstruction; and in the **liquid** environment, of the same Polystyrene microspheres under 0.3 mm layer of water: **c**) 2D and **d**) 3D reconstruction. The diameter of the single sphere is - 2.0 microns. Scale is given in nanometers. Image is given without the scanner non-linearity correction.



# Chapter 3

---

## Pulse excitation/gated detection of an optical signal

This Chapter discuss less standard aspect of SNOM technique, viz. gated detection of an optical signal. Fast scanning of our SNOM enables to overcome the severe photostability problem, which was very important to obtain fluorescent images. These images are presented and briefly discussed in the following sections. Pulsed excitation/gated detection of an optical signal is illustrated by presentation and discussion of a near-field optical ‘pseudoresolution’ (in all probability a kind of topography artifact, see in following sections later) of the glass slide surface-deposited 100-nm-diameter transfluorescent spheres in noisy conditions [55].

### 3.1 The single molecule fluorescence spectroscopy detectors

The photon counting detectors used to measure weak fluorescence signals should have a low rate of dark counts and high quantum efficiency. Single-channel detectors, such as photomultiplier tube (PMT) or avalanche photodiode (APD) have a high time resolution and are used to measure the fluorescence lifetimes and intensity correlation functions. The APD has a higher detection quantum yield than PMT for orange-red region of light. The limitation of APD is its small active area, but this is an advantage for single molecule detector rather than a disadvantage. Its small active area can act as an additional pinhole to reject the out-of-focus autofluorescence. For APD, the signal-to-noise ratio is determined by the shot noise rather than read-out noise [74].

According to Spinelli *et al.* [104], a single-photon avalanche photodiodes (SPADs) are now in use for an increasingly large range of applications in which light detection with single-photon sensitivity is required. Compared to photomultiplier tubes (PMTs), they offer several advantages, including ruggedness, low operating voltage, compact size, and more or less low cost.

### 3.2 Photon counting interface: pulse excitation and gated detection of an optical signal

The photon counting interface of our SNOM electronics (see Appendix II) enables to record an optical signal either in analog (e.g. PMT in current mode) or digital (single photon count) modes. One known practical limitation of SNOM technique consists in the fact that at the output of the sharpened fibre probe one cannot attain intensity materially exceeding the level of the order of  $I_{\max} \cong 10^3 \text{ W cm}^{-2}$  (cw mode), because a subwavelength aperture probe is easily damaged by more intense light passing through it. Of course, this limitation complicates things a lot and makes some tasks requiring a high sensitivity, for example, single-molecule detection, very difficult to solve [55].

One approach to cope with this limitation and improve the SNOM detection possibility (the signal-to-noise ratio) consists in using the pulse excitation and gated detection of the emitted photons. This idea is based on the circumstance that the photodamage of a fibre probe is due mainly to the thermal effects of light ('aperture burning'), and roughly the same quantity of light can be introduced into the fibre probe during 1 s either in a cw mode or in a pulsed one provided the pulse repetition frequency  $N_{puls}$  is large enough and condition  $EN_{puls} \cong I_{\max}$  holds. (Here  $E$  is the light pulse energy). The latter statement has been confirmed by us using both nanosecond Nd:YAG pulse lasers at 532 and 1064 nm wavelength and an acousto-optical modulator to prepare laser pulses with the duration of 10–100  $\mu\text{s}$  starting from cw Nd:YAG laser. When, as it usually takes place, the process of the laser excitation/fluorescence of species to be studied is a linear one with respect to the incoming light intensity, signal-to-noise ratio can be much improved when pulsed illumination and gated detection is used: the number of signal photons collected

remains the same whereas the noise counts diminishes  $1/N_{\text{puls}} \tau$  times. Here  $\tau$  is the light pulse duration; we suppose that the photons are detected using the gate coinciding with the excitation pulse and that  $\tau$  is longer than characteristic fluorescence time, which for the most dyes, luminescent defects in solids, etc. do not exceed 10 ns or at most 100 ns. Of course, such an approach enables to diminish only those noise counts that are not directly related with the excitation light itself, that is, for example, own dark counts of detector or a stray light; it cannot diminish, say, the noise due to the detection of excitation photons, which avoid cutting by filters or monochromators, or like. However, in many cases exactly these noise sources, especially the stray light contamination, is of uttermost importance, and pulse illumination/detection scheme is then very useful [55].

Our SNOM is equipped with the built-in *photon-detection mode* quite suitable to realize this approach. Two options are available: (1) if a TTL pulse from an external source is used as a trigger source, gated detection can be switched on when a time  $T_1$  from this TTL pulse passed, then this signal is detected during a time  $T_2$  and switched off afterwards; (2) or, alternatively, SNOM electronics itself can generate a TTL pulse that is used to trigger the external laser (or for similar purposes). In the latter case, this same electronics switches on a photon detector when a time  $T_1$  from the TTL pulse passed, keeps it active during a time  $T_2$  and then switches this detector off. The values of  $T_1$  and  $T_2$  are installed by user as an option of the SNOM software, and they are a quantum of 25 ns [55].

In Fig. 21, we present the results of testing of this *time-gated pulsed detection mode*. Sample is the polystyrene TransFluoSpheres 543/620 with the diameter of 100 nm deposited onto the standard 170- $\mu\text{m}$ -thick glass plate by simple drying from the water solution drop. [TransFluoSpheres 543/620 is a trademark of Molecular Probes Inc., Oregon, used to designate spheres containing specially selected pair of donor–acceptor dyes to attain the large difference between excitation (543 nm) and fluorescence (620 nm) maxima]. Concentration of the beads in a drop is selected in such a manner that the densely packed monolayer coating of the glass slide with the spheres could be anticipated provided that they are uniformly distributed over the slide surface. Sometimes (in certain areas on the glass slide surface) this is indeed the case, but rather irregular multi-layer coatings of beads are formed in the most areas of the slide, as this

is illustrated by the topographical image in the right side of Fig. 21. Note that this image is deliberately left uncorrected for scanner non-linearities because, in our opinion, such a correction (which is trivial to realize) prevents the characterization of a microscope (scanner), giving the characterization of the software used instead. To illustrate this point, in Fig. 22 we presented both corrected and non-corrected topographical shear-force images of the calibration grating TGT-01 of NTMDT Company, Zelenograd, Russia [55].

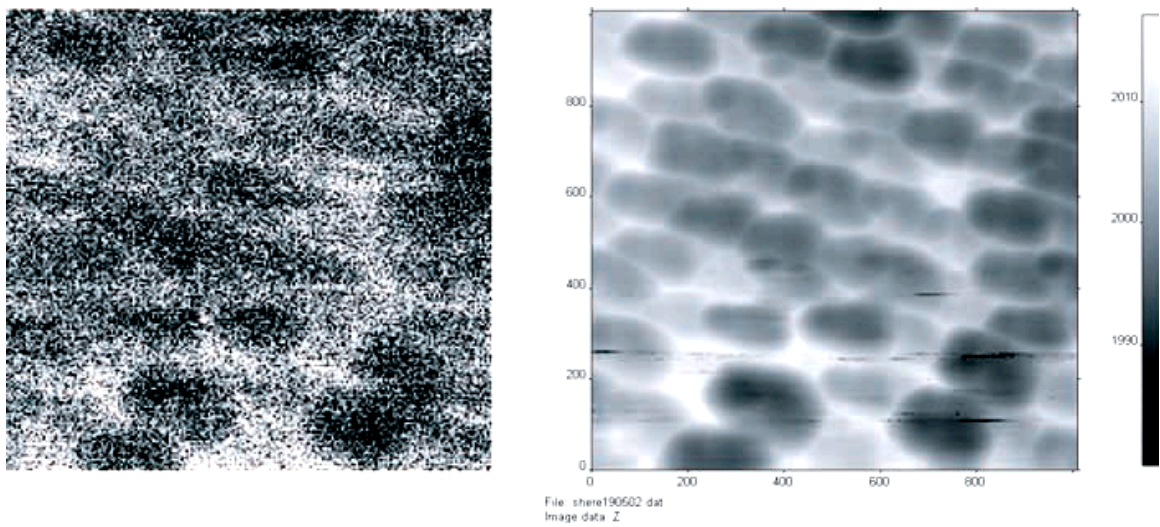
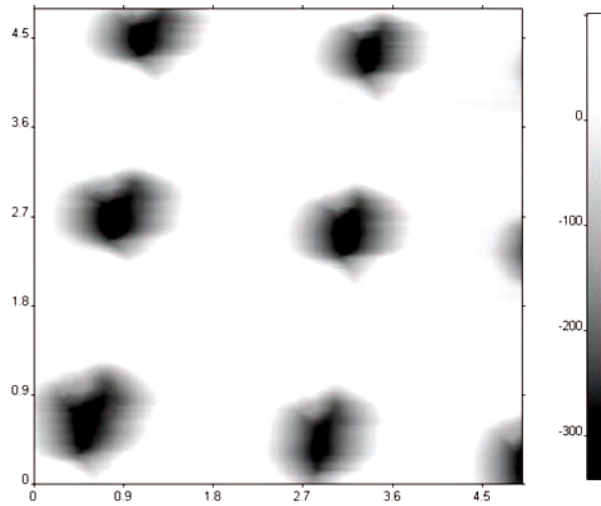
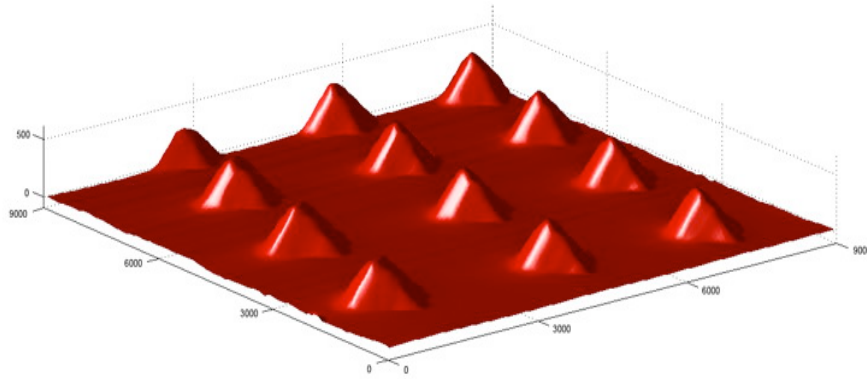


**Fig. 21** Scanning near-field optical image taken using pulsed excitation/gated detection mode (left; maximum of the signal (white) corresponds to  $3.8 \times 10^4$  counts  $s^{-1}$ , minimum of the signal (black) corresponds to  $2.0 \times 10^4$  counts  $s^{-1}$ ) and shear-force topographical image (right) of 100-nm-diameter TransFluoSpheres 543/620 by Molecular Probes, Oregon, deposited onto the glass slide surface by simple drying from a drop. Scanner is pre-calibrated and sizes are given in nanometers (grey bar scale is used for  $z$  coordinate), but no electronic or software correction for scanner non-linearity is used; cf. **Fig. 22** [55].



**a**



**b**

**Fig. 22** Shear force topographical image of TGT 01 calibration grating (NT-MDT Company, Russia). **a)** image without scanner non-linearity correction, **b)** another image of the same grating corrected for the scanner non-linearity and presented as a 3D picture. Scale is given in nanometres, note that  $z$ -scale in 3D image is different from  $x$  and  $y$  scales. Grating period:  $2.12\ \mu\text{m}$ , tip height:  $0.3\text{--}0.5\ \mu\text{m}$ , tip point radius of curvature is not larger than  $10\ \text{nm}$  from which the radius of a curvature of the fibre probe (uncoated home-made by etching in HF solution) around  $80\ \text{nm}$  in one direction and  $150\ \text{nm}$  in other direction can be inferred [55].

Pulse detection option number two was exploited: pulsed laser illumination is realized by passing exciting  $532\ \text{nm}$  light from cw Nd:YAG laser via acousto-optical modulator and then introducing it into the aperture fibre probe (Nanonics, Israel, nominal aperture size  $100\ \text{nm}$ ). Fluorescence photons were collected by a  $20\times$  micro-objective and detected by a red-sensitive PMT (Hamamatsu Photonics, Japan) equipped with an appropriate combination of spectral filters (notch filter from Kaiser, U.S.A., and glass color filters) to reject an excitation light. Pulse duration was equal to  $10\text{--}100\ \mu\text{s}$  and pulse repetition rate to  $1\ \text{kHz}$ , hence  $1/N_{puls}\tau = 10\text{--}100$ . One millijoule of light

energy has been introduced into the fibre during 1 s, the value which we know from our earlier experiments as being the safe for the case of fibre used (Nanonics Supertips, Israel, with the nominal aperture of 100 nm) when working in a continuous illumination mode (while approximately 2 mW can be already dangerous) [55].

### 3.3 Conclusion

In summary, our experiments show that this same power value is safe also for the discussed mode employing the acousto-optical modulator. Clear optical ‘pseudoresolution’, which is in all probability the topographical artifact, is seen in Fig. 22 (see e.g. references [75, 76] and references therein for discussion of origin of such artifacts in SNOM images), whereas working without a pulsed excitation/gated detection mode we were not able to discern such a ‘pseudo-optical resolution’ due to essentially smaller signal-to-noise ratio [55]. Note also that in our SNOM a standard TTL output pulse is generated simultaneously with the change of  $x$  or  $y$  position of the sample/sensor during the scanning, that is, with the beginning of information collection at a new point. This option proved to be really important when microscope is combined with modern ultrasensitive CCD camera for photon detection, where such TTL pulse is required to govern the work of the camera.

# Chapter 4

---

## Imaging of live *E.coli* and Green *Synechococcus* cells

In this chapter we will give an overview of biology of two eukaryotic living cells that we investigated with our home made SNOM adopted for use in liquid. The SNOM study of *Escherichia coli* (E.coli) and *Green Synechococcus* - type of Picocyanobacteria (PCC 7942) cells produced interesting topographical and fluorescence data. We will discuss the importance and reasons of working with these species. In the last section details of sample preparation and subsequent cell deposition for SNOM experiments are given.

### 4.1 *Escherichia coli* bacteria

*Escherichia coli* (E.coli), originally known as *Bacterium coli commune*, was identified in 1885 by the German pediatrician, Theodor Escherich. E.coli is widely present in the intestine of humans and warm-blooded animals and is the predominant facultative anaerobe in the bowel and part of the essential intestinal flora that maintains the physiology of the healthy host. E.coli is a member of the family Enterobacteriaceae, which includes many genera, including known pathogens such as *Salmonella*, *Shigella*, and *Yersinia* [77]. Although most strains of *E.coli* are harmless, others can make you sick. Some kinds of *E.coli* can cause diarrhea, while others cause urinary tract infections, respiratory illness and pneumonia, and other illnesses. Still other kinds of *E.coli* are used as markers for water contamination, which are not themselves harmful, but indicate the water is contaminated [78].

The *E.coli* is a one of the widely known eukaryotic cells, which has the oval shape and complex internal structure. Depending on the type of the cells, their size may vary from one to another with typical dimensions of length from 2 to 2.5  $\mu\text{m}$  and width of

0.5 to 1  $\mu\text{m}$ . A distinct feature of bacterial cells is a rigid cellular wall that is a critical factor in the survival of these organisms in a broad range of environmental conditions [79]. The bacteria have a capsule with a wall that rigidly protects from external invasion. The plasma membrane and cytoplasm are also important substances that are nurturing the ribosomes, plasmid and nucleoid (DNA). Finally, from an outer plasma membrane there are many small pili's and flagellum. Fig. 23 illustrates the internal structure of eukaryotic cells.

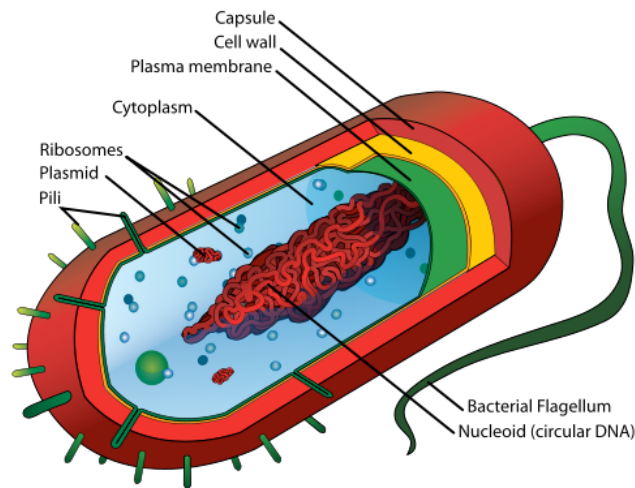


**Fig. 23** Internal structure of eukaryotic cells [80].

Being surrounded by cellular wall, bacteria have a surface much more rigid than that of animal cells, which simplifies SNOM study. Moreover, our SNOM allows imaging in liquid without the sample drying thus enabling to image live cells. One of the main advantages of scanning probe microscopy over conventional structural research techniques is the possibility of imaging in liquid [79].

The SNOM used in this study was modified as discussed previously. For our SNOM study with living *E.coli* bacteria, the cell culture growth and preparation methods here elaborated by Dr. Jozef Adamcik. Since we succeeded with the imaging in liquid of calibration gratings and polystyrene spheres, the following essential step was to image biological soft samples. In Fig. 24 we present the shear-force topographical images of the *E. coli* bacteria, obtained under a  $\sim 0.3$ -mm thick layer of water. Looking at these topographical images one can say that oval structure is well observed in all images of Fig. 24. However, the images made in liquid environment are smoother, which could



indicate that the cells were not as damaged as in case **a)** and **b)** of Fig. 24. The scales are given in nanometers.

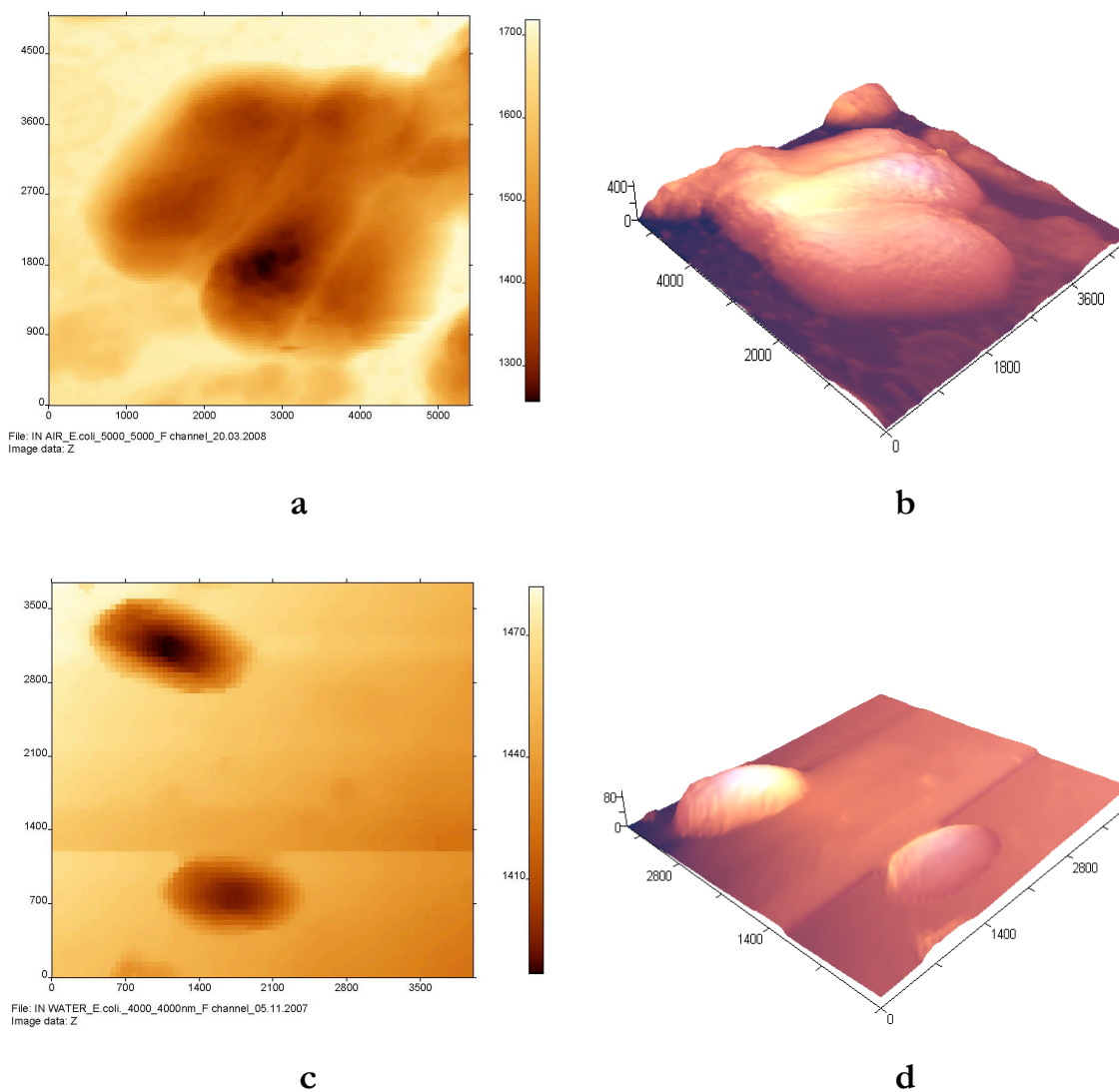


**Fig. 24** Shear-force topographical images of the *Escherichia coli* cells in *air* (**a** – 2D and **b** – 3D reconstruction) and in *liquid* (**c** – 2D and **d** – 3D reconstruction) environments. These topographical images were obtained under  $\sim 0.3$  mm-thick layer of water. Sizes are given in nanometers and  $z$ -scale in 3D images is different from  $x$  and  $y$  scales [81].

## 4.2 Green *Synechococcus* cyanobacteria

Cyanobacteria are a phylogenetically primitive group of gram-negative prokaryotes having a cosmopolitan distribution ranging from hot springs to the Arctic and Antarctic regions. They were probably the first photosynthetic oxygen-evolving organisms that appeared during the Precambrian era (between 2.8 and 3.5 x 10<sup>9</sup> years ago) and provided a favourable condition for the evolution of current aerobic life. Cyanobacteria are major biomass producers both in aquatic as well as terrestrial ecosystems and represent more than 50% of the biomass in many aquatic ecosystems [82].

Cyanobacteria cells are commonly found in freshwater, springs, wetlands, rivers, lakes and oceans. They play a major role in the nitrogen, carbon, and oxygen dynamics of many aquatic environments. Being an extremely important component of the overall primary production in ecosystems of all climatic zones, they are increasingly investigated during the last years. Phototrophic picocyanobacteria, contribute to the carbon fixed in marine systems and perform oxygenic photosynthesis like plants and algae [83, 84].

As the first organisms to use oxygenic photosynthesis, cyanobacteria were key players in the early evolution of life on Earth. *Oxygenic photosynthesis* (a biological process that converts light energy into chemical energy and splits water to release oxygen) requires the coordinated action of two photosystems that, working in series, generate the electrochemical potential needed to extract electrons from water, releasing O<sub>2</sub>. The production of oxygen by cyanobacteria was responsible for the oxidation of Earth's atmosphere around 2.4 to 2.2 billion years ago; cyanobacteria also contributed substantially to *primary productivity* (the production of organic compounds from CO<sub>2</sub>) in the Proterozoic eon and are now important players in the carbon and nitrogen cycles of the biosphere [85].

## 4.2.1 Varieties of Cyanobacteria

Cyanobacteria were formerly classified as *blue-green algae* because of their algal-like appearance, their possession of *chlorophyll* rather than bacteriochlorophyll, and their photosynthetic production of oxygen by a two-photosystem process as in algae and higher plants. They also possess several features that set them apart from other bacteria, especially their photosynthetic apparatus and their ability to produce oxygen [86].

Modern-day cyanobacteria include some 2000 species in 150 genera and 5 orders (see Table 1), with a great variety of shapes and sizes. Ecologically, there are three major groups in the aquatic environment: *mat-forming* species, which form periphytic biofilms over rocks, sediments, and submerged plants; *bloom-formers*, which create a wide range of water quality problems and that are most common in nutrient-rich (eutrophic) lakes; and picocyanobacteria, which are extremely small cells (<3 µm in diameter) that are often abundant in clear water lakes [86].

Among many varieties of cyanobacteria cell lines in this section we will concentrate on: filamentous chain like cyanobacteria type – of Nostocales group (*Anabaena*, *Nostoc* and *Scytonema*); and the isolated individual cells type – of Chroococcales group (*Synechococcus*) (see Table 1). These cells are most widely distributed in almost all aquatic media of the Earth.

<i>Order</i>	<i>Characteristics</i>	<i>Illustrative genera</i>
1. Chroococcales	Cocoid cells that reproduce by binary fission or budding	<i>Aphanocapsa</i> , <i>Aphanothece</i> , <i>Gloeocapsa</i> , <i>Merismopedia</i> , <i>Microcystis</i> , <i>Synechococcus</i> , <i>Synechocystis</i> <i>Chroococciopsis</i> , <i>Pleurocapsa</i>
2. Pleurocapsales	Cocoid cells, aggregates or pseudo-filaments that reproduce by baeocytes	
3. Oscillatoriales	Uniseriate filaments, without heterocysts or akinetes	<i>Lyngbya</i> , <i>Leptolyngbya</i> , <i>Microcoleus</i> , <i>Oscillatoria</i> , <i>Phormidium</i> , <i>Planktothrix</i>
4. Nostocales	Filamentous cyanobacteria that divide in only one plane, with heterocysts; false branching in genera such as <i>Scytonema</i>	<i>Anabaena</i> , <i>Aphanizomenon</i> , <i>Calothrix</i> , <i>Cylindrospermopsis</i> , <i>Nostoc</i> , <i>Scytonema</i> , <i>Tolypothrix</i>
5. Stigonematales	Division in more than one plane; true branching and multiseriate forms; heterocysts	<i>Mastigocladus (Fischerella)</i> , <i>Stigonema</i>

In the bacterial classification scheme, the orders are referred to as subsections of Phylum BX: Cyanobacteria.

**Table 1.** The five orders of cyanobacteria recognized in the classic botanical taxonomic scheme [86].

The cyanobacteria are a phylogenetically coherent group of organisms that also include chloroplasts. However, cyanobacteria have diversified through evolution, producing both unicellular and multicellular forms. The multicellular forms consist of trichomes (see Fig. 25) that, in some strains, can contain hundreds of cells. Most cyanobacteria divide by binary fission, but some exhibit alternatives to the standard mode of bacterial division, reproducing by budding or by multiple fission of enlarged cells. In some filamentous cyanobacteria, vegetative cells can differentiate into *heterocysts* (Fig. 25, **a**), which are specialized for the fixation of N<sub>2</sub> gas; a subset of these cyanobacteria can also form spores, which are known as *akinetes* (Fig. 25, **c**). In the filaments of most heterocyst forming cyanobacteria, such as *Anabaena* spp. (also known as *Nostoc* PCC 7120), the cells divide in only one plane, but in the filaments of some other species, such as *Fischerella* spp., the cells can divide in more than one plane. Some filamentous cyanobacteria also produce hormogonia, which are small motile filaments that can serve a dispersal function in some benthic species (Fig. 25, **d**). Multicellularity involves at least three well-defined processes: cell–cell adhesion, intercellular communication and cell differentiation. These features include a special supracellular structure and the developmental process that produces a filament with two metabolically interdependent cell types, the photosynthetic vegetative cells and the N<sub>2</sub> fixing heterocysts [85].

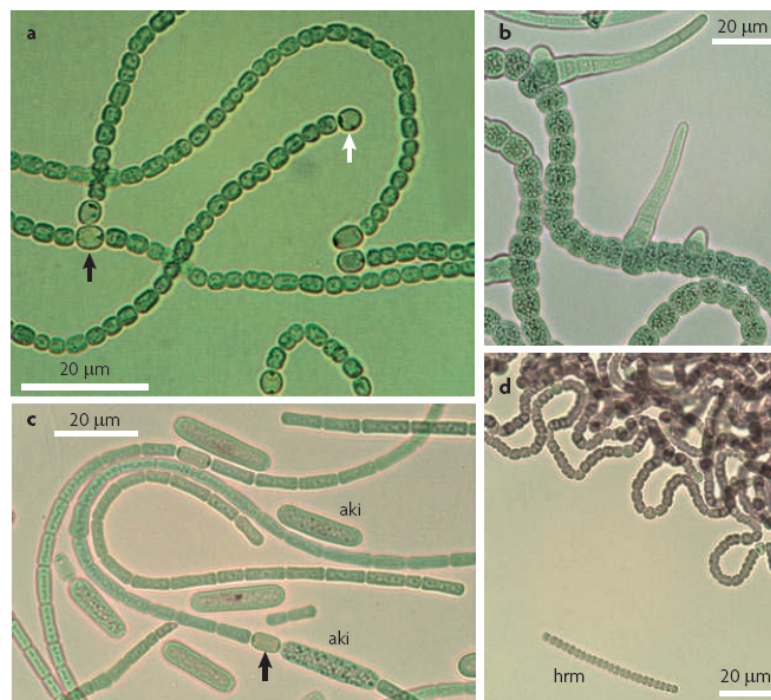


**Fig. 25** Cell types in heterocyst-forming cyanobacteria. **a)** N<sub>2</sub>-grown filaments of *Anabaena* sp. PCC 7120 (also known as *Nostoc* sp. PCC 7120) showing terminal heterocysts (white arrow; note the presence of only one polar granule) and intercalary heterocysts (black arrow; note the presence of two polar granules) in addition to vegetative cells. **b)** Filaments of *Fischerella muscicola* showing true filament branches that result from cell division in more than one plane. **c)** N<sub>2</sub>-grown filaments of *Anabaena cylindrica*, with heterocysts (black arrow) and akinetes in addition to vegetative cells; akinetes adjacent to heterocysts in the filament and isolated akinetes (already released from the filament) can be observed. **d)** N<sub>2</sub>-grown *Nostoc* sp. PCC 9203 showing mature filaments of vegetative cells and heterocysts and one hormogonium (hrm; note the small size of its cells) that has moved away from the colony [85].

Picocyanobacteria are the smallest of cyanobacteria cells, often around one thousandth of a millimetre in diameter; however, they typically occur in high concentrations. Two of the genera *Synechococcus* and *Prochlorococcus* are abundant in the world's oceans from 50° South to 70° North and play a significant role in metal sorption. Picocyanobacteria can reach very high concentrations in nutrient rich saline lakes where the competition for light may be severe, and where their superior light-capturing ability confers an advantage. Moreover, they have been readily observed by epifluorescence microscopy, and increasingly by flow cytometry, and comparative studies have shown that they contribute a large proportion of total photosynthetic biomass in oligotrophic lakes [86]. Fig. 26 illustrate the fluorescence microscopic image (UV excited) of the *Synechococcus* PCC 7942 under physiological condition.

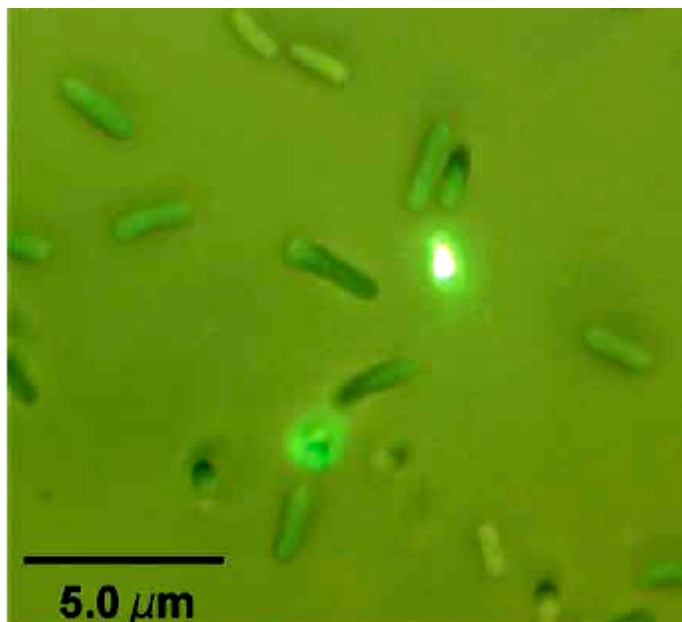


**Fig. 26** The fluorescence microscopic image (UV excited) of living *Synechococcus elongatus* type of Picocyanobacteria (PCC 7942) cells under physiological condition [87].

For our SNOM measurements in liquid, we investigated the *Synechococcus* PCC 7942. These cells are quite similar to *E.coli* cells with their dimensions and typical isolated oval structure. However, imaging of Picocyanobacteria cell has a significant advantage. This is due to natural fluorescent pigments located within the cells and participating through photosynthesis process to producing oxygen dioxide production.

Since we were able to get *E.coli* cells topography with high resolution in liquid, the next essential step was the near-field optical investigation. For this study we used picocyanobacteria cells, scanning them in native physiological condition (in liquid). Although cyanobacterial picoplankton is often the dominant phytoplankton in terms of biomass, a limited number of studies have examined their influence on the biogeochemical cycling in aquatic systems. The characterization of picocyanobacteria surface properties is necessary to reveal their role in the biogeochemistry of aquatic systems and their photosynthetic functions, which makes them a good target for a SNOM study. Almost no such research was reported, which is probably due to difficulties of experimental work with SNOM in liquids [81].

With the high Q-factor of our homemade SNOM sensor, we were able to perform SNOM measurements in liquid, which is very important for living cells. In Fig. 27 we illustrate shear-force topographical 3D image of live *Synechococcus* PCC 7942, obtained in *liquid* using our microscope. This image was obtained under around  $\sim 0.3$  mm thick layer of water. Scales are given in nanometers.

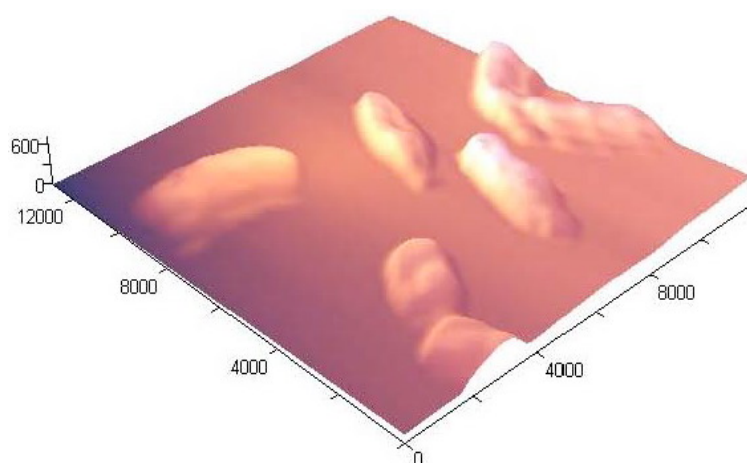


**Fig. 27** Shear-force topography image of living cells of the Green *Synechococcus*-type of Picocyanobacteria strain (PCC 7942) obtained using our home-made SNOM in liquid. This topography image were obtained under  $\sim 0.3$  mm-thick layer of water. Scales are given in nanometers [81].

## 4.2.2 Cyanobacterial pigments and Photosynthesis

Cyanobacteria cells play a key role in natural photosynthesis process in aquatic media, absorbing carbon dioxide and harmful sunlight and producing oxygen. This important photochemical process occurs in almost all places on Earth, and cells can survive at wide temperature ranges (15-74°C), and have several important fluorescent pigments [86]. These pigments and other molecular complexes play a vital role in proper physiological functioning of living cells. However, there are several important pigments such as **Chlorophyll  $\alpha$**  and **Scytonemin**, which are responsible for the absorption of sunlight and fluorescence. The presence of endogenous fluorescent pigments in photoautotrophic organisms on one hand allows distinction of different populations, but on the other it limits the choice of probes [87].

One of major and well-studied cyanobacterial pigments is **Chlorophyll  $\alpha$**  (Chl  $\alpha$ ), which contains the blue phycobiliproteins *phycocyanin* and *allophycocyanin*, giving to the cells their characteristic *blue-green* color. Phycobiliproteins are located in structures called *phycobilisomes* on the *thylakoid* (photosynthetic) membranes. These are highly efficient 'light guides', transferring captured solar energy (excitation energy) to reaction centers of photosynthesis of **Photosystem I** (PS I) and **Photosystem II** (PS II) [86].

Electronic excitation that is generated in the light-harvesting system of *Synechococcus* is transferred to the reaction center of PS I or PS II and initiates photosynthetic electron transport. Electronic excitation is also dissipated as heat and as fluorescence emission that can be used effectively to monitor various photosynthetic processes. Selective excitation by blue light (i.e.  $\lambda=488$  nm) generates fluorescence from the Chl  $\alpha$  and scytonemin molecules of both PS II and PS I [88, 89].

Although cyanobacteria lack membrane-bound organelles, they have a variety of cellular structures and inclusions that have specialized functions and that contribute to their ecological success. These include the photosynthetic thylakoid membranes containing the phycobilisomes, and the nucleoid region or centropylasm in the center of the cell, which contains the complex folded, circular DNA, often in multiple copies. The cells also contain various storage bodies, including glycogen (polyglucose) granules that store carbon. Cyanophycin granules of the cell are stores of nitrogen, composed of arginine and aspartic acid. Finally, the carboxysomes are composed by ribulose 1,5-

bisphosphate carboxylase/oxygenase and act as a store of this photosynthetic enzyme as well as of nitrogen and polyphosphate granules. These inclusions allow cells to accumulate energy and nutrients far in excess of their present requirements when they are under favorable conditions [86]. In the following sub-section we will discuss different aspects of above mentioned cyanobacterial fluorescent pigments and give brief historical and biological overview of cyanobacteria.

#### 4.2.2.1 Scytonemin pigment

Despite of the knowledge of the existence of the pigment called *scytonemin* for over 100 years, its structure has remained unsolved until now. When discovering this pigment, Nägeli C. reported that it is exclusively produced by cyanobacteria [90]. This pigment was the first shown to be an effective, photo-stable ultraviolet shield in prokaryotes. It is a dimeric molecule of indolic and phenolic subunits. It has been observed only in the sheaths enclosing the cells of cyanobacteria. The sheath of cyanobacterial *scytonemin* has green colored pigment with potent ultraviolet absorbing properties. *Scytonemin* was known only from the extracellular sheath of cyanobacterial subunit of Picocyanobacteria (*blue-green algae*), and primarily when these photosynthetic prokaryotes are exposed to high solar irradiance [91].

According to Proteau P. J. *et al.*, the pigment of *scytonemin* plays an important role in UV-screening during evaluation of cyanobacteria. The absorption spectrum of *scytonemin* in intact sheaths and the complete spectrum of the purified pigment are illustrated in Fig. 28. The pigment absorbs strongly in the UV-A spectral region (315-400 nm) with an *in vivo*  $\lambda_{\max}$  = 370 nm. However, there is also significant absorbance in the violet and blue region as well as in the UV-B (280-320 nm) and UV-C (190-280nm). The regulation of this pigment appears to reflect the requirements of a sunscreen, because final sheath content varies directly with UV flux [91].



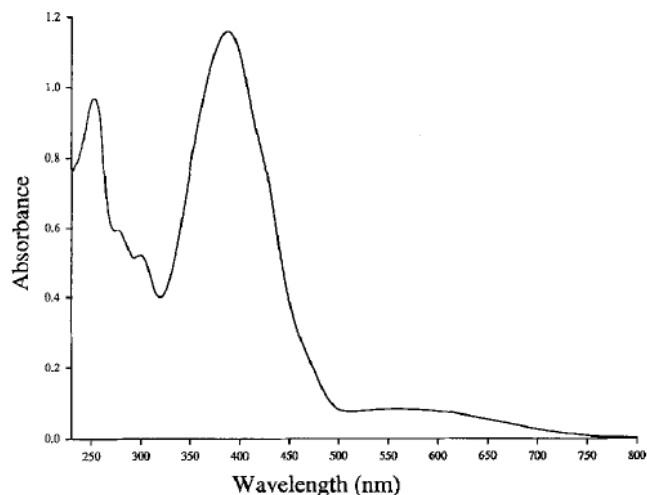


**Fig. 28** Ultraviolet-visible spectrum of scytonemin (concentration =  $2.2 \times 10^{-5}$  M) in tetrahydrofuran ( $\lambda_{\text{max}}=252$  nm, 278 nm, 300nm and 386 nm; a smoothing function was applied to the 500-800 nm region) [91].

According to Singh S. P. *et al.*, *scytonemin* is a yellow-brown lipid-soluble and inducible pigment located in the extracellular polysaccharide sheath of some cyanobacterial species. *Scytonemin* is a dimer composed of indolic and phenolic subunits having a molecular mass of 544 Da. A purified scytonemin shows maximum absorption at  $\lambda=386$  nm but it also absorbs significantly at 252 nm, 278 nm and 300 nm (Fig. 29). In Fig. 29, **a**) the molecular structure of this pigment is illustrated, and Fig. 29, **b**) shows the absorption spectrum of *scytonemin* from *Nostoc commune* of cyanobacterial cell.

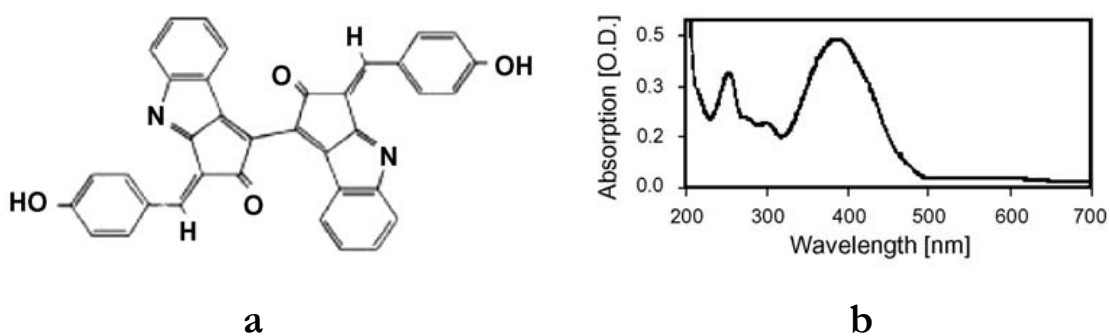
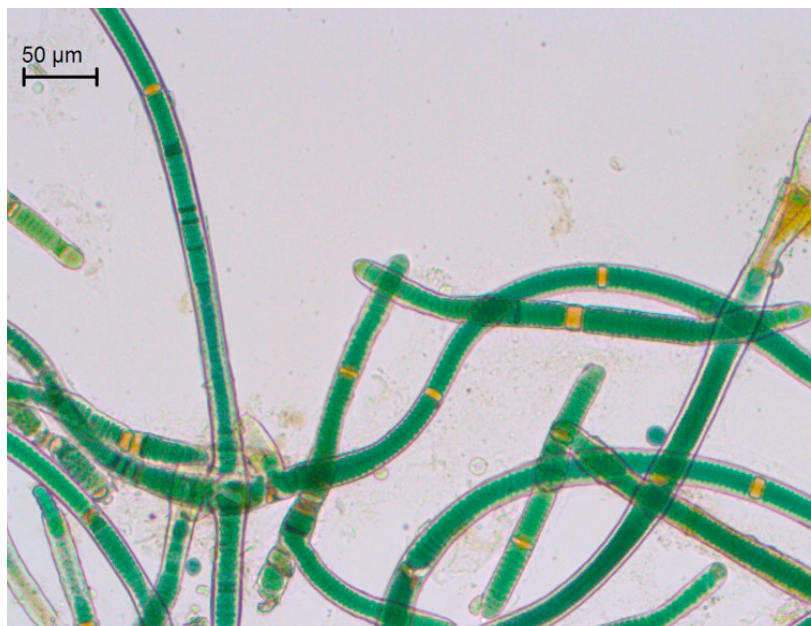


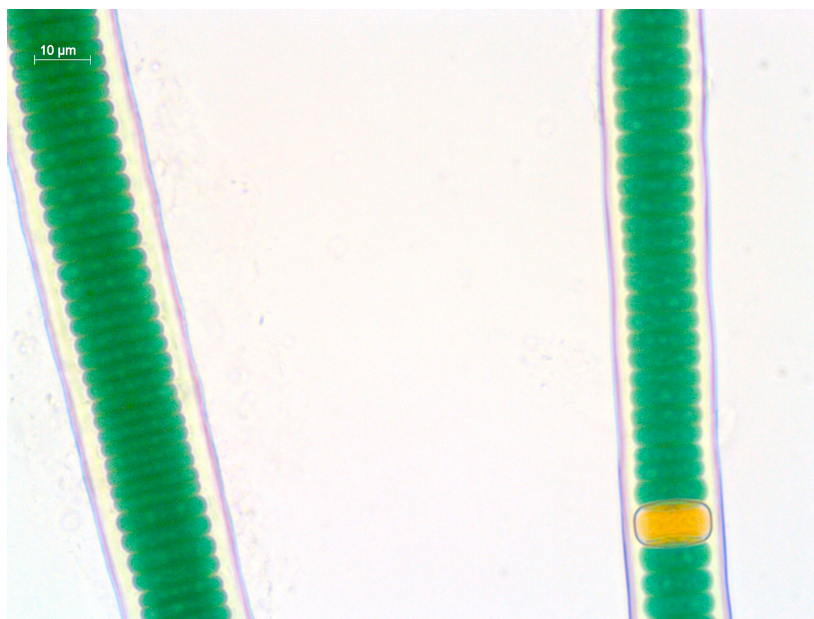
**Fig. 29** The molecular structure of scytonemin **a**) and absorption spectrum of scytonemin from *Nostoc commune* **b**) [82].

*Scytonemin* synthesis is primarily induced by UV-A radiation whereas blue, green or red light at the same intensity does not have a significant influence. In Fig. 30 confocal optical microscopy photography of living cyanobacteria type – 179a *Scytonema*, shows the presence of yellow-brown colored *scytonemin* pigment, 640x times magnified (image

courtesy of Prof. Karl Gademann and Dr. Cyril Portmann). Scale bars are given in microns.



**a**



**b**

**Fig. 30** The confocal optical microscopy photographs (**a** and **b**) of living cyanobacteria type 179a *Scytonema*, showing the presence of yellow-brown colored *scytonemin* pigment (image courtesy of Prof. Karl Gademann and Dr. Cyril Portmann). Scale bars are given in microns.

*Scytonemin* is highly stable and performs its screening activity without any further metabolic investment even under prolonged physiological inactivity. Thus, *scytonemin* can also protect cyanobacteria when other UV-protective mechanisms such as active repair of damaged cellular components are ineffective. Moreover, cyanobacteria have several targets susceptible to Ultra Violet Radiation (UVR) stress and have developed several lines of defense mechanisms that sustain their successful growth and survival in various habitats receiving high solar UVR (see Fig. 31). The balance between damage and defense mechanisms also has the ecological importance as it maintains the productivity and nitrogen economy of an ecosystem and, thereby, regulates other climate change problems [82].

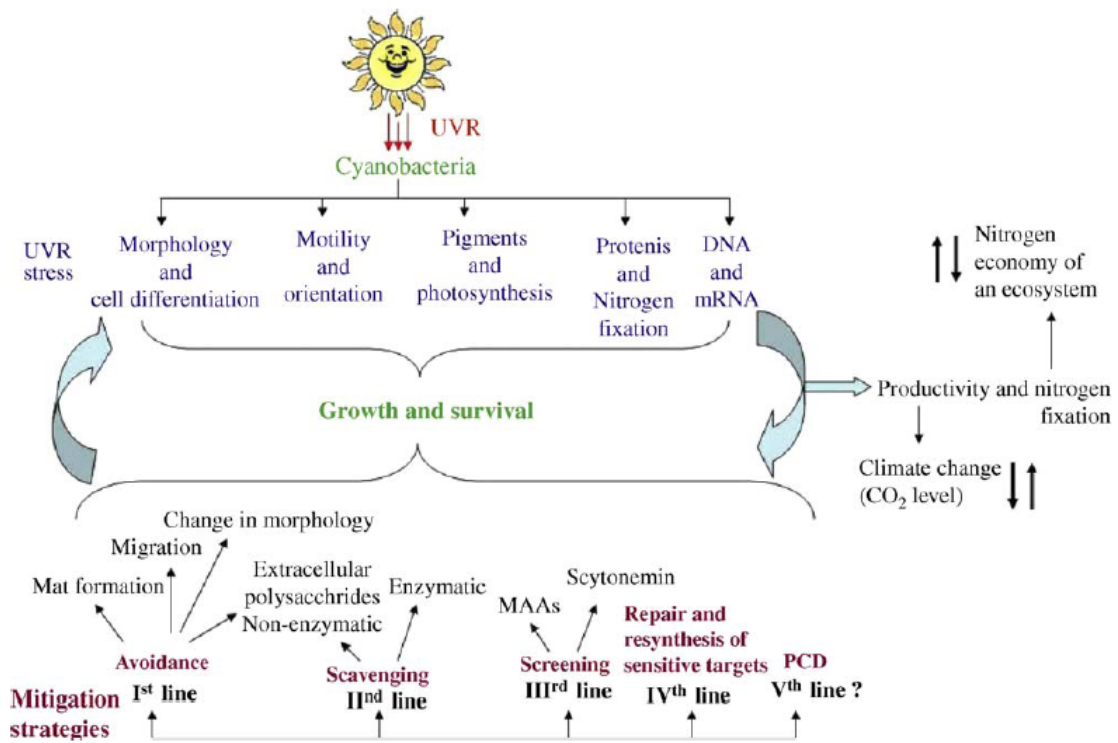


**Fig. 31** Model showing the effects of UVR and mitigation strategies employed by cyanobacteria to cope with this radiation. It also represents the outcome of these two processes on an ecosystem level. '?' indicates role to be verified under UVR stress [82].

*Scytonemin* seems to play an important role in microbial communities exposed to high solar radiation. The high concentration of *scytonemin* in many cyanobacterial sheaths will provide significant protection to other microorganisms living within and beneath the upper layer of sheathed cyanobacteria [91].

## 4.2.2.2 Chlorophyll $\alpha$ pigment

The **chlorophyll  $\alpha$**  (Chl  $\alpha$ ) was identified as one of the principle pigments that emit fluorescence in *Synechococcus elongatus* PCC 7942, and the intensity of which is decreased with illumination time. Likewise, physicochemical and physiological processes that occur within and across the thylakoid membranes is related to photosynthesis and affect Chl  $\alpha$  pigment. Moreover, the syntheses and degradations of holochromic proteins affect the stoichiometry of photosystems and the sizes of their antennae. It is common in all oxyphototrophs, but lack the peripheral trans-membrane light-harvesting complexes of the eukaryotic cells. Instead, for light harvesting they use phycobiliproteins C-phycoyanin (CPC) and allophycocyanin (APC) [89].

Kaňa R. *et al.*, showed (Fig. 32, **A**) the absorption spectrum of the *Synechococcus* sp. PCC 7942 cells suspension at room temperature, and in Fig. 32, **B**) fluorescence emission spectra of the same cell suspensions frozen at 77 K and measured at 2 different wavelengths of excitation. The absorption band maxima and the main contributing chromophores are at wavelengths: 436 nm, 489 nm, 625 nm and 677 nm. Low temperature fluorescence was excited either at 438 nm where Chl  $\alpha$  *in vivo* absorbs strongly and CPC plus APC weakly, or at 580 nm where CPC and APC absorb strongly and Chl  $\alpha$  less strongly. These spectra are shown here in order to characterize the cyanobacterial cells [87].

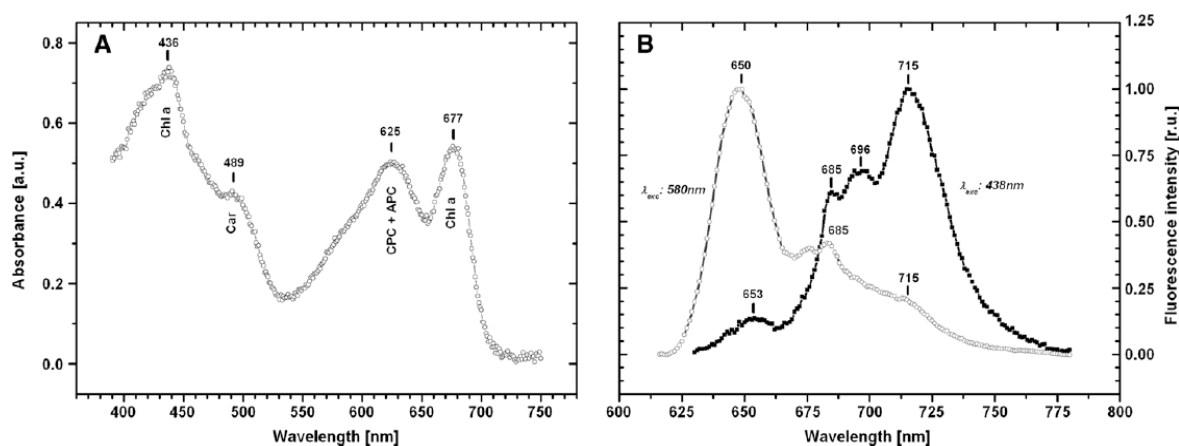


**Fig. 32** Absorption **A**) and fluorescence spectra **B**) of *Synechococcus* sp. PCC 7942. Absorption of a cell suspension was recorded at room temperature; fluorescence of frozen cell suspension was measured at 77 K, following excitation either at 438 nm (closed circles) or at 580 nm (open circles). Displayed curves are average of three measurements [89].

In the same paper Kaňa R. *et al.* showed (Fig. 33) that Chl  $\alpha$  fluorescence time course (also referred as fluorescence induction) curves recorded at room temperature (15 min) with dark pre-adapted *Synechococcus* cell suspensions. The cells were illuminated continuously either with the blue (464 nm), or with orange (622 nm) actinic light and fluorescence was detected in the spectral interval 690–710 nm. Since the blue excitation at 464 nm was not significantly absorbed by CPC or by APC, only Chl  $\alpha$  were excited directly by this blue excitation [89].

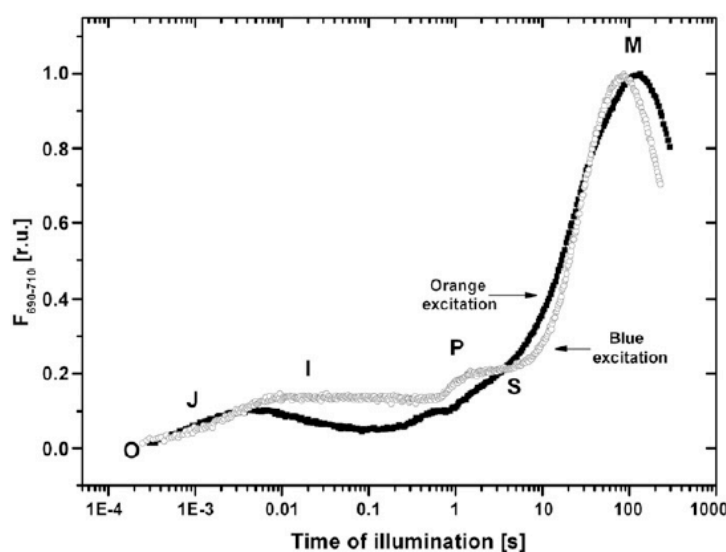


**Fig. 33** Time course of chlorophyll  $\alpha$  fluorescence from *Synechococcus* sp. PCC 7942 suspension during continuous excitation at room temperature. Fluorescence was detected in the 690–710 nm range with excitation either at 464 nm ( $200 \mu\text{mol (photons) m}^{-2} \text{s}^{-1}$ ; blue actinic light) or at 622 nm ( $33 \mu\text{mol (photons) m}^{-2} \text{s}^{-1}$ ; orange actinic light). The fluorescence induction (FI) curves were normalized to equal M - O differences and the O level fluorescence was set to zero to allow us to compare blue light induced FI with FI after orange light excitation [89].

In the Fig. 33, authors showed two normalized curves to facilitate their comparison. In cyanobacteria, the 464 nm excitation is preferentially absorbed by PS I that contains more Chl  $\alpha$  than by PS II. However, because of PS I RC (P700) turns over faster than the PS II, it has lower fluorescence intensity than the PS II antenna. Therefore, Chl  $\alpha$  fluorescence excited by blue actinic light at 464 nm is weaker in comparison to excitation by orange light at 622 nm, as the orange light absorbed by CPC is primarily transferred to more fluorescent Chl  $\alpha$  of PS II. This was indicated by a low temperature PS I emission band (F715) of dark-adapted cells (Fig. 32, **B**) where F715 (emission of PSI) is much weaker for 580 nm excitation than the PS II emission band (F685) [89].

There is another interesting paper of Stamatkis K. *et al.*, where the authors discuss the fluorescence behavior of Chl  $\alpha$  induced by NaCl at room temperature for

*Synechococcus* sp. PCC 7942 cells. The Chl  $\alpha$  fluorescence of photosynthetic cells originates from PS II holochromes. In cyanobacteria, Chl  $\alpha$  fluorescence can be excited either by direct photon absorption or by radiationless energy transfer. As result in the experiment depicted in Fig. 34, the authors showed that NaCl induced swelling of *Synechococcus* cells influences the directly excited Chl  $\alpha$  fluorescence. Cell suspensions were excited at various wavelengths, and the rise of Chl  $\alpha$  fluorescence upon addition of 0.4 M NaCl was monitored at 685 nm. The action spectrum of  $(F_2^{MAX} - F_2^{MIN})(F_2^{MIN})^{-1}$  vs  $\lambda_{exc}$  is clearly correlated to the absorption of C-phycoyanin (maximum at 620 nm), the main phycobiliprotein of *synechococcus* [92].

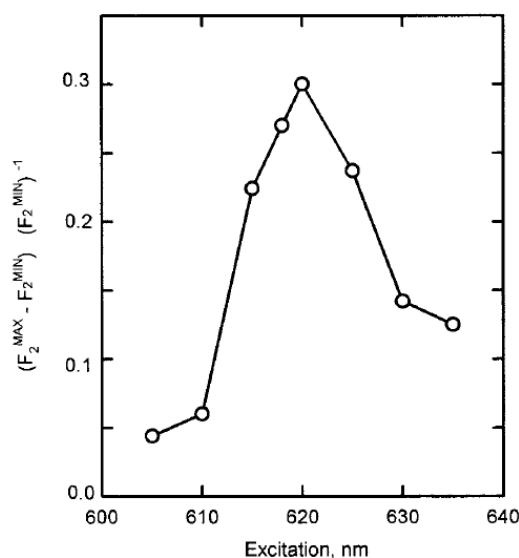


**Fig. 34** Action spectrum of the NaCl-induced rise of Chl  $\alpha$  fluorescence in *Synechococcus* sp. PCC 7942 cells. Dark-acclimated (4 min, 20  $\mu$ M DCMU) cells were excited with weak light (350  $\text{nmol m}^{-2}$  at  $\lambda=620$  nm;  $\Delta\lambda=5$  nm) at various wavelengths (abscissa) and the NaCl-induced (0.4 M) fluorescence rise was recorded at 685 nm (DI 5 10 nm). The fluorescence was detected at right angles to the excitation. The relative NaCl-induced fluorescence increment,  $(F_2^{MAX} - F_2^{MIN})(F_2^{MIN})^{-1}$ , was plotted against the excitation wavelength [92].

In summary, the process of photosynthesis and fluorescent pigments of cyanobacteria cells all together forms complex biochemical system. The ability of some species of cyanobacteria to fix nitrogen gives them a competitive advantage in low nitrate, low ammonium waters, and may also contribute substantial quantities of new nitrogen to aquatic ecosystems. One particularly important habitat for cyanobacteria is the flooded rice fields, where the cyanobacteria increase the nitrogen content and fertility of the soil because of their nitrogen-fixing capability [86].

## 4.3 Near field optical detection of living cells

The SNOM investigation of living Green *Synechococcus* – type Picocyanobacteria cell line (PCC 7942) in liquid was carried out. The technical details of exploited SNOM geometry and the advantages of use are discussed in part 2.9 of present Thesis.

### 4.3.1 Introduction

By improving the resolution beyond the limit of diffraction optics SNOM offers enhanced axial and lateral resolution of topographic features and fluorescence signals and is developing into an important technique for visualizing biological systems [93].

### 4.3.2 Experimental and results

In this study of living cells in liquids, we used our homemade SNOM setup intended for work in liquid environment. After successful imaging of topography of *E.coli* cells in air and liquids we shifted to optical observation of another live cell line Green *Synechococcus* – type of Picocyanobacteria (PCC 7942). The genera of *Synechococcus* PCC 7942 cell are one of the members of *Chroococcales* cell family (see in part 4.2.1.).

According to literature and other experiments, morphologically they are similar to previously studied *E.coli* cells, and have the typical oval shape too, with average sizes of **2 to 2.5** microns in length and **0.5-0.6** microns in width. The *main reason* for our choice of this cell line was the ability of pigment to absorb and fluoresce under the laser light. Hence, it was an excellent candidate for further near-field optical investigations.

The already described new geometry of SNOM made it easy to navigate the “cell chamber” along the Z direction allowing us to work in transmission mode. The cell chamber was specially designed with a thin squared glass mounted in the center, and fixed in order to prevent any water leak.

The SNOM experiments were started with the switching on the laser and the sample preparation. Once we got the sample ready we deposited them onto the specially prepared thin glass, which then was placed inside the cell chamber (see Fig. 17 (4)). For these measurements, we used our proprietary SNOM based on the earlier reported double-resonant montage of the fiber probe onto the tuning fork [55, 56]. Such a

montage preserves high quality factor of the probe, which makes this microscope suitable for work in liquids. Acting forces are kept in the sub nano-Newton range, which enables the study of fragile biological samples such as live bacteria and cells [81].

Once the tip reaches the surface, we carefully start to move the external water reservoir along the Z direction (see Fig. 16 (4)), to let the water slowly start filling the cell chamber. Looking through the additional Stereo Optical Microscope (Leica EZ5), we were able to precisely control the level of water covering the surface. Experience shows, that the optimal depth of SNOM tip immersed into the water is about  $\sim 0.3$  mm, where Q-factor of SNOM sensor ranges from **300** to **600**. This is to our knowledge one of the highest values of Q-factor with SNOM research in liquid.

In order to illuminate our samples, we used an Ar-ion laser at the wavelength of  $\lambda=488$  nm, and power intensity at the entrance of SNOM probe with an average of 2-3 mW. The power values were measured each time before the experiment by Power Meter (model 1815-C, Newport, USA).

The Holographic Notch filter was used for cut the noise and illumination light and pass only the filtered fluorescent laser light. The fluorescence photons were collected by 40x or 60x objective of an inverted microscope. In Fig. 35 we present a schematical illustration of near-field imaging on an inverted microscope [94].

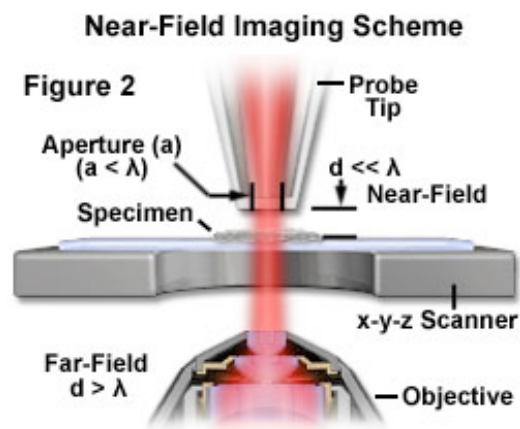


**Fig. 35** A representation of the typical SNOM imaging scheme on inverted optical microscope [94].



In Figures 36 and 37 we present shear-force topographical and near-field optical images of *Green Synechococcus* - type of Picocyanobacteria (PCC 7942) in *liquid*. In Figures 36 **c**) and 37 **(c, d)** there are cross-sections of these images showing the contours of each topographical and optical image of the cells. Scales are given in nanometers for the topographic images (Figures 36 **a**) and 37 **a**)), and fluorescent intensity is given as arbitrary units (a.u.) where the maximum value is 10 (Figures 36 **b**) and 37 **b**)). The darker region in fluorescence image corresponds to lower and brighter to higher fluorescence.

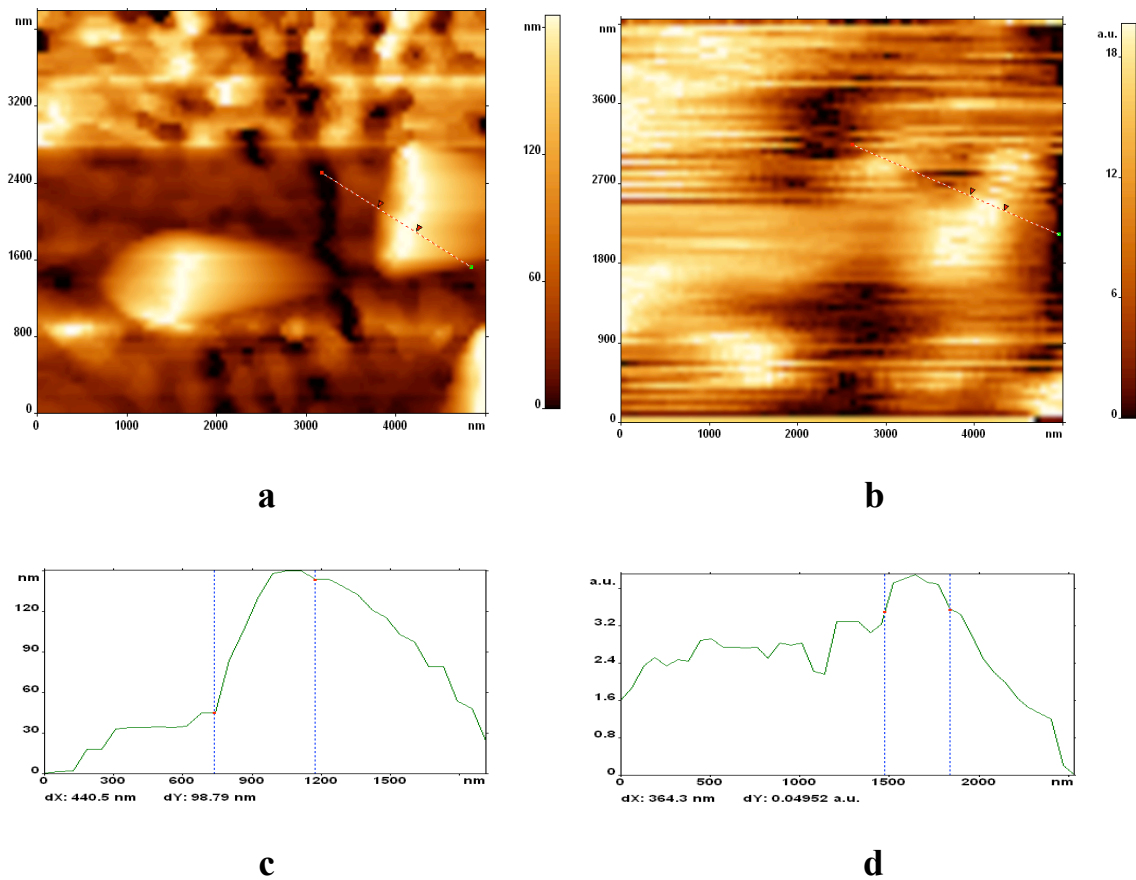


**Fig. 36** Shear-force topographical image **a**) and cross-section of chosen place **c**); Near-field optical image **b**) and cross-section of chosen place **d**): of *Green Synechococcus* – type of Picocyanobacteria (PCC 7942) in *liquid*. Corresponding image sizes are given in nanometers. In image **b**) fluorescent intensity scale is given in arbitrary units.

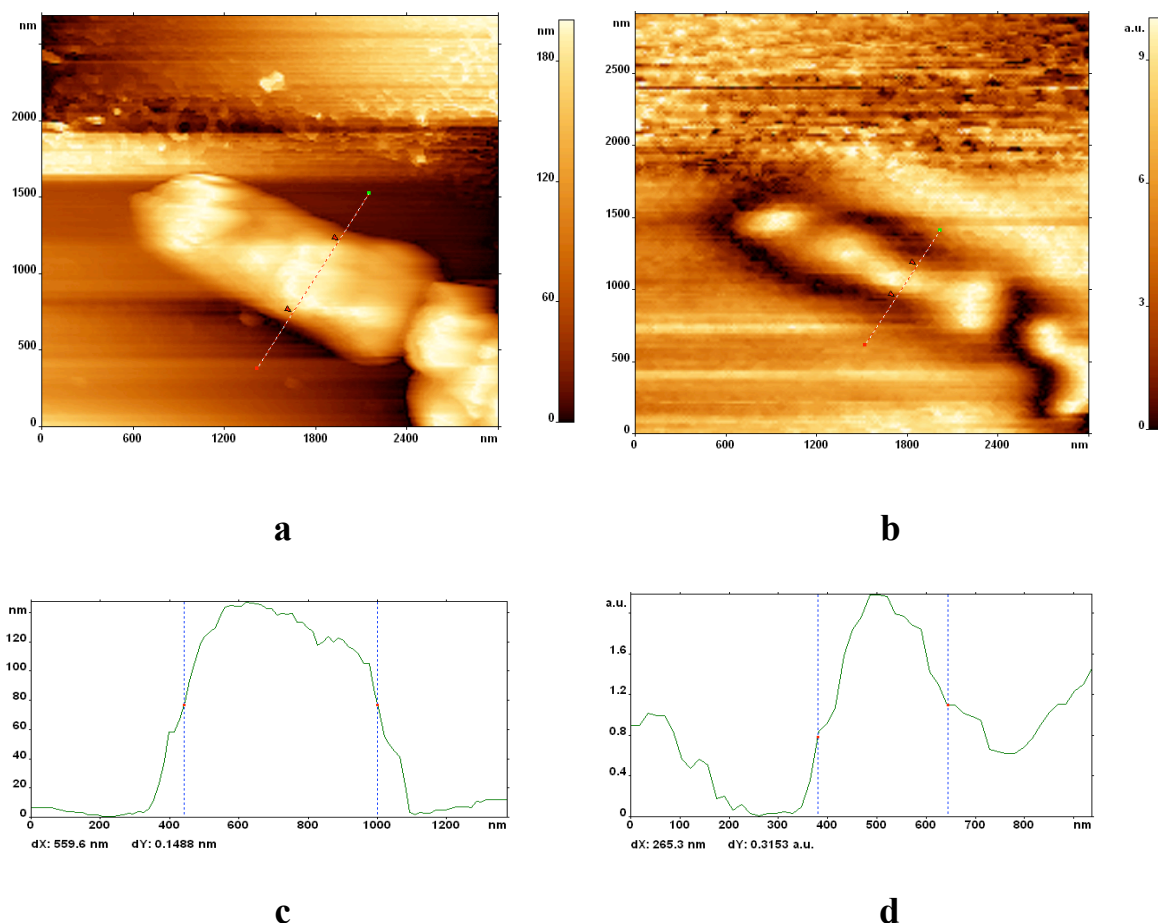


**Fig. 37** Shear-force topographical image **a)** and cross-section of chosen place **c)**; Near-field optical image **b)** and cross-section of chosen place **d)**: of *Green Synechococcus* – type of Picocyanobacteria (PCC 7942) in *liquid*. Corresponding image sizes are given in nanometers. In image **b)** fluorescent intensity scale is given in arbitrary units.

Subramaniam V. *et al.* have performed SNOM measurements on *E.coli* bacteria expressing a mutant Green Fluorescent Protein (GFP). They calculated that fluorescence distribution along the bacteria was heterogeneous, and the optical intensity fluctuated within each cell. Depending on concentration and purity of final cell solution, the distribution of cells (i.e. isolated *E.coli* or cyanobacteria) on the glass surface is different. In Fig. 38 we obtained more or less the same picture was showed by Subramaniam V. and co-workers with the same *Synechococcus* PCC 7942 living cells in *liquid*. Scales are given in nanometers, and darker region in fluorescence image corresponds to lower and brighter to higher intensity [95].

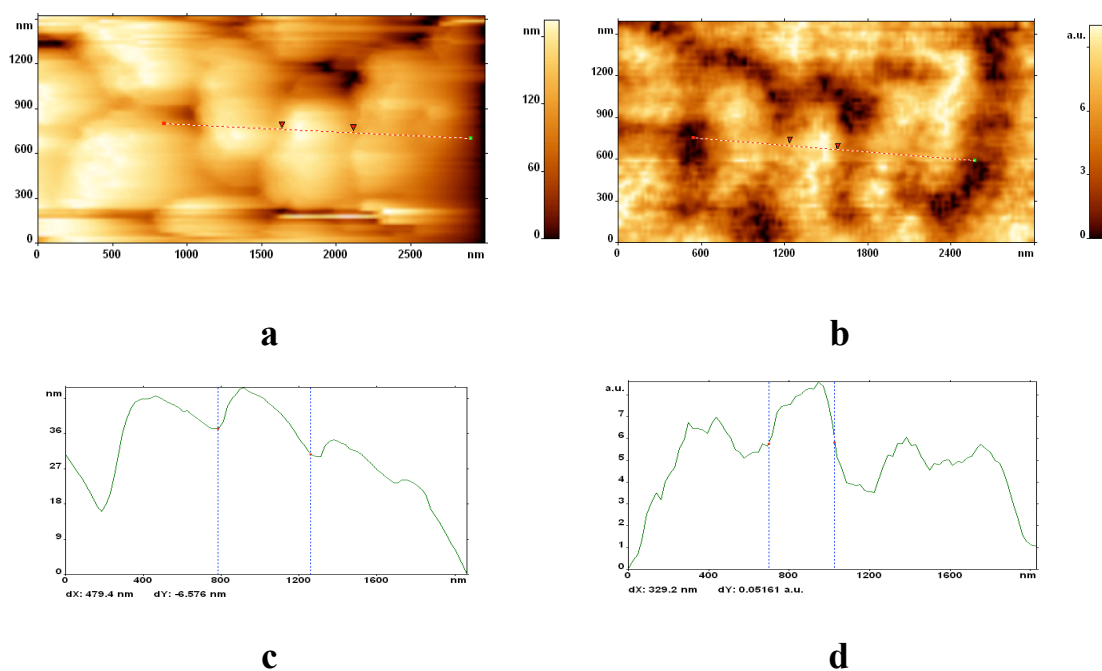


**Fig. 38** Shear-force topographical image **a**) and cross-section of chosen place **c**); Near-field optical image **b**) and cross-section of chosen place **d**): of *Green Synechococcus* – type of Picocyanobacteria (PCC 7942) in *liquid*. Corresponding image sizes are given in nanometers. In image **b**) fluorescent intensity scale is given in arbitrary units.

It is known that continuously irradiated fluorescent molecules experience a photobleaching leads to a decrease in fluorescence intensity as a function of time. Our experiments show that after 2.5-3 hours of intense scan, the fluorescence emission from cyanobacteria cells in liquid starts to slowly diminish.

There are additional factors that influence the survival rate of living cells during the SNOM measurements. They are the follows – the age of the cell culture, the laser light intensity (power value) and the working environment (air or liquid). Experimentally, during several years, we have noticed that fluorescence images obtained in liquid media were constant for a longer time, compared to those that were made in air (maximum ~1-1.5 hour).

In Figures 39 and 40 we present shear-force topography and near-filed optical images of the *Synechococcus* PCC 7942 cells obtained in *liquid*. Figures 39 (**c**, **d**) and 40 (**c**, **d**) show cross-sections, both in optical image of the cells. In both Figures 39 and 40 of **d**), subwavelength-size structures of fluorescent pigments in the cells can be seen. The darker region in the images corresponds to lower and brighter to higher fluorescence

signal. In Fig. 40 e), there is a 3D optical image presentation that shows the distribution of photo-active pigments along the cells.

Paula A. M. *et al.* have obtained somewhat analogous near-field optical images, where the large absorption was mainly at the sides of the bacterium *Pseudomonas aeruginosa* and optical path length through the membrane was the largest. This explains why the bright spots are visible on the sides of cells [96].

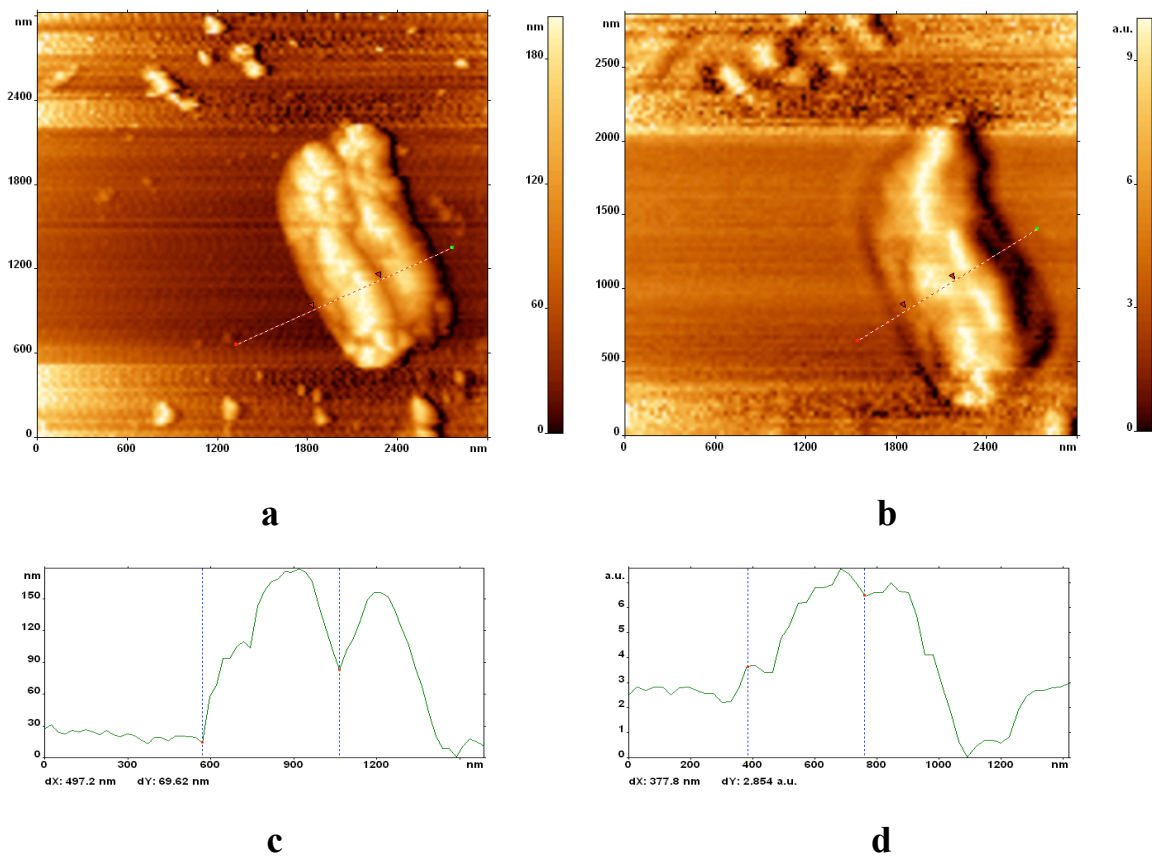


**Fig. 39** Shear-force topographical image **a)** and cross-section of chosen place **c)**; Near-field optical image **b)** and cross-section of chosen place **d)**: of *Green Synechococcus* – type of Pico cyanobacteria (PCC 7942) in liquid. Corresponding image sizes are given in nanometers. In image **b)** fluorescent intensity scale is given in arbitrary units.

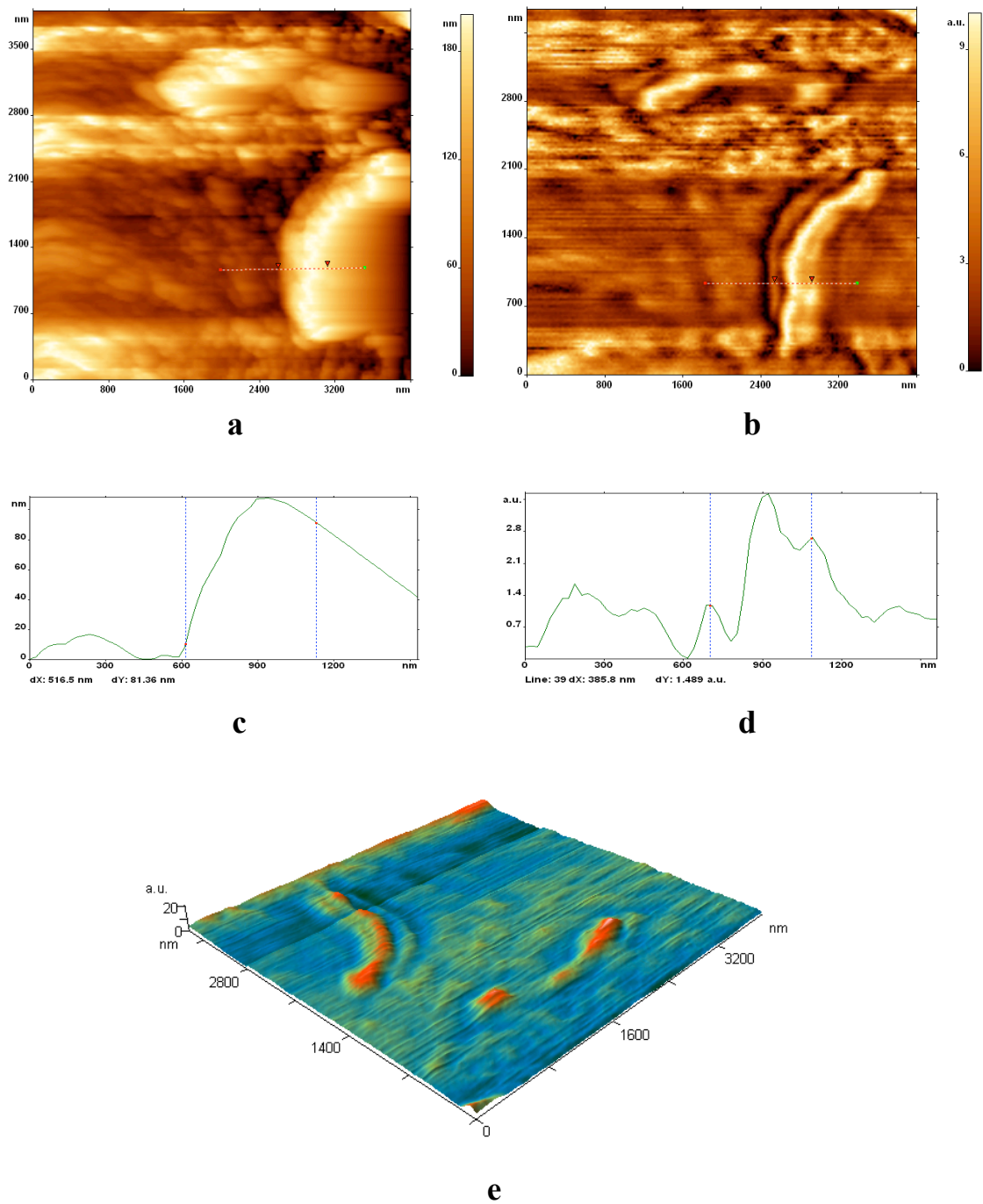


**Fig. 40** Shear-force topographical image **a**) and cross-section of chosen place **c**); Near-field optical image **b**) and cross-section of chosen place **d**): of *Green Synechococcus* – type of Picocyanobacteria (PCC 7942) in *liquid*. An image **e**) is 3D reconstruction of the near-field optical image **(b)**. The distribution of fluorescent pigments in image **c**) of Chlorophyll  $\alpha$  and Scytonemin along the cell are clearly seen. Dark colored surface is refers to lower optical intensity. Corresponding image sizes are given in nanometers. In image **b**) fluorescent intensity scale is given in arbitrary units.

## 4.4 Sample preparation

In this section we will discuss the sample preparation and surface treatment for SNOM measurements. Among many methods and protocols for preparation of living cells for SNOM we have elaborated, by trial and error, a methodology that contains several steps.

In order to perform a SNOM study with live cells, we established a collaboration with Prof. Karl Gademann's laboratory (Department of Chemistry, University of Basel) who kindly provided us with the cell culture of *Synechococcus* type - Picocyanobacteria cells lines (PCC 7942). The wet sample preparation procedure was done in our laboratory. Since the sunlight is the energy source of living cells, we stored our solution with the cyanobacteria close to windows (at room temperature).

Here is a simple protocol for sample preparation based on our tests:

The *first* step is to clean up all the plastic polymer tubes (Microtube, Treff Lab) and glass surfaces (Gold-seal coverslip; Electron Microscope Sciences, thickness 125  $\mu\text{m}$ , 18 x 18 mm). The 96% Ethanol solution (Fluka, Chemika, Switzerland) was used for primary clean. The slow flow of nanopure de-ionized water (Labtec, Services AG, Switzerland) was used for secondary additional cleaning. After this, we let everything completely dry in a chemical box (Erchmann, Plastic AG, Switzerland). In order to attach live cells onto the glass surface, we immersed the glass coverslips into a 0.1% Poly-L-Lysine solution (P8920, Sigma-Aldrich) for 30 minutes, and then air-dried them overnight in special polymer box to avoid any contamination.

The *second* step is a purifying process for our live cells. We extracted 20  $\mu\text{l}$  of cell culture from initial solution by micropipette's tips (Starlab GMBH), and injected them in two polymer tubes (1.5 ml volume) with 10  $\mu\text{l}$  for each tube (two tubes were necessary for minimal equal compensation of centrifuge motion). Then we put these tubes in a centrifuge (Sigma, Biolock Scientific), where they were centrifuged at 7000 turns/minute during 8 minutes at 22°C. As a result we got pressed cells in the bottom separated from the liquid in the upper part of the tubes. After we discarded this liquid into a special tube for used solution. Then we took 20  $\mu\text{l}$  of fresh purified water and injected it into these two tubes and mixed them until we got homogenous solutions again. For each purifying process we used new micropipette tips.

The *third* step is the deposition of cells onto the glass surface. For this we extracted 10  $\mu\text{l}$  of final solution and deposited it onto the treated glass surface for 60 minutes. Then we gently rinsed the surface of glass using nanopure water flow, thus removing non-attached cells. We found that after these operations the homogenous monolayer of single cells is formed. In total, we have repeated all procedures for three times, and then, without drying, the wet sample was ready for near field optical investigations.

## 4.5 Conclusion

In conclusion, our results indicate that typical dimensions of cells are in good agreement with the literature. Depending on the measuring conditions (working in air/liquid, high/less laser intensity and whole time for the scanning), the distribution of fluorescent pigments of cyanobacteria varies. In some cases, subwavelength-size photosynthetic structures were observed.

The high Q-factors of the SNOM sensors allowed us to get high-resolution topographical images of cells. Results are promising and further investigation of other types of living cells is planned.

# Chapter 5

---

## Near-field scanning optical microscopy using polymethylmethacrylate optical fibre probes

In this Chapter we report the first use of polymethylmethacrylate (PMMA) optical fiber-made probes for scanning near-field optical microscopy (SNOM). The sharp tips were prepared by chemical etching of the fibers in ethyl acetate, and the probes were prepared by proper gluing of sharpened fibers onto the tuning fork in the conditions of the double resonance (working frequency of a tuning fork coincides with the resonance frequency of dithering of the free standing part of the fiber) reported earlier for the case of glass fibers. Quality factors of the probes ranging 2000-6000 were obtained which enables to realize an excellent topographical resolution including state-of-art imaging of single DNA molecules. Near field optical performance of the microscope is illustrated by the Photon Scanning Tunneling Microscope images of fluorescent beads with a diameter of 100 nm. The preparation of these plastic fiber probes proved to be easy, needs not any hazardous material and/or procedures, and typical exploitation time of a probe essentially exceeds that characteristic for the glass fiber probe [93].

### 5.1 Introduction

Scanning near-field optical microscopy (SNOM) is capable to measure optical properties on a subwavelength scale exceeding the Abbe diffraction limit with the simultaneous topography imaging with a nanometer spatial resolution. Nowadays it is widely used to study a broad variety of samples in biology, material science, nanotechnology and other fields; see e.g. [10, 11, 97, 19] for recent reviews [93].



By far the most popular SNOM probe is a metal-coated tapered optical glass fiber on which apex an aperture for the light transmission, which diameter is between 50 and 200 nm, is formed. The optical resolution is of the order of the aperture size. Unfortunately, these probes are expensive, very fragile (not surprising for a glass-made construction) and their fabrication is difficult, hard to control and hazardous process. Of course, the wide use of the scanning near-field optical microscopy is hampered by the difficulty in producing probes with sufficient accuracy and a good reproducibility [93].

In this Chapter we present first SNOM probes made from polymethylmethacrylate (PMMA) optical fibers, which nowadays rapidly gain popularity as “last one hundred meters fibers” due to their cheapness and easiness to work with, see e. g. [98, 99]. Concerning the SNOM domain, these fibers look very promising because for SNOM probes made from them one can anticipate much less fragility (compare glass and plastic) and easiness to prepare the sharp tip. Actually, for such a preparation hazardous HF treating, which remains the most popular approach to prepare SNOM probes from the glass fibers [10, 11, 97, 19], can be completely avoided. These anticipations were confirmed by experiments which results are presented below [93].

## 5.2 Experimental

Plastic or polymer (or polymethylmethacrylate) optical fiber (POF) is a fiber type optical waveguide and can transmit optical signal up to several kilometers. Since optical signal is propagated along the fiber by total internal reflection, POF has sheath (or cladding)-core structure and refractive index of cladding should be lower than that of core, i.e.,  $n_{\text{cladding}} < n_{\text{core}}$  [100]. The POF used in this study were purchased from A.R.T. Photonics GmbH, Germany. They are step index type fibers with a diameter of 250  $\mu\text{m}$  made of high purity PMMA core, with an index of refraction of  $n_{\text{core}} = 1.49$ , and a fluorinated PMMA cladding with an index of refraction of  $n_{\text{cladding}} = 1.35$  [93].

Compared to silica used as core material for glass optical fiber, PMMA is very ductile and cheap. Therefore, it is possible to make optical fiber with large core size, which is easy to connect. Although POF has such advantages, the use of POF in data

communication is rather restricted to the automotive field, mainly due to rather high optical loss of POF at the telecommunication wavelength range of 1300 ~ 1600 nm. This is originated from the chemical structure of PMMA, which contains C-H bonds. Their vibrational overtones are a main cause of the loss. The main role of optical fibers including POF is to transmit light or optical signal to a specified spot. However, if we apply physical or chemical treatment to cladding of POF, the light leaks out from damaged spot and we can use such sidelight POF for decorations or lighting [100].

A 99.5% ethyl acetate (EA, Aldrich) was chosen as an etchant because weight loss of POF in it was observed to be the most significant and because the dissolution rate of POF in EA is almost linear with immersion time; in this sense our results coincide with the data presented in [100]. Fig. 41 shows the variation in the degree of dissolution of bare POF with the type of the solvent and immersion time. In contrast to chloroform and acetone, which are good solvents for PMMA, the dissolution rate of POF in EA is almost linear with immersion time [100].

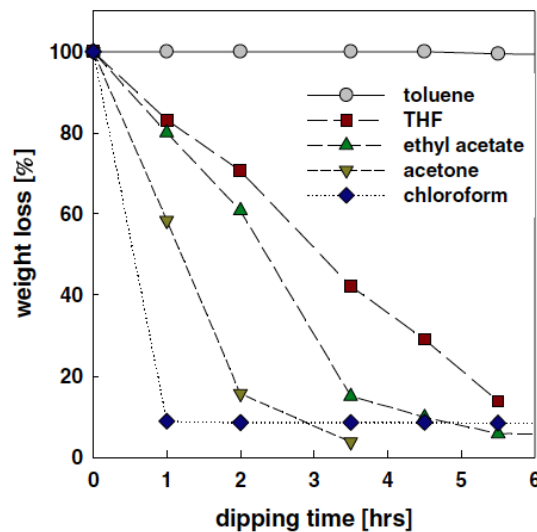
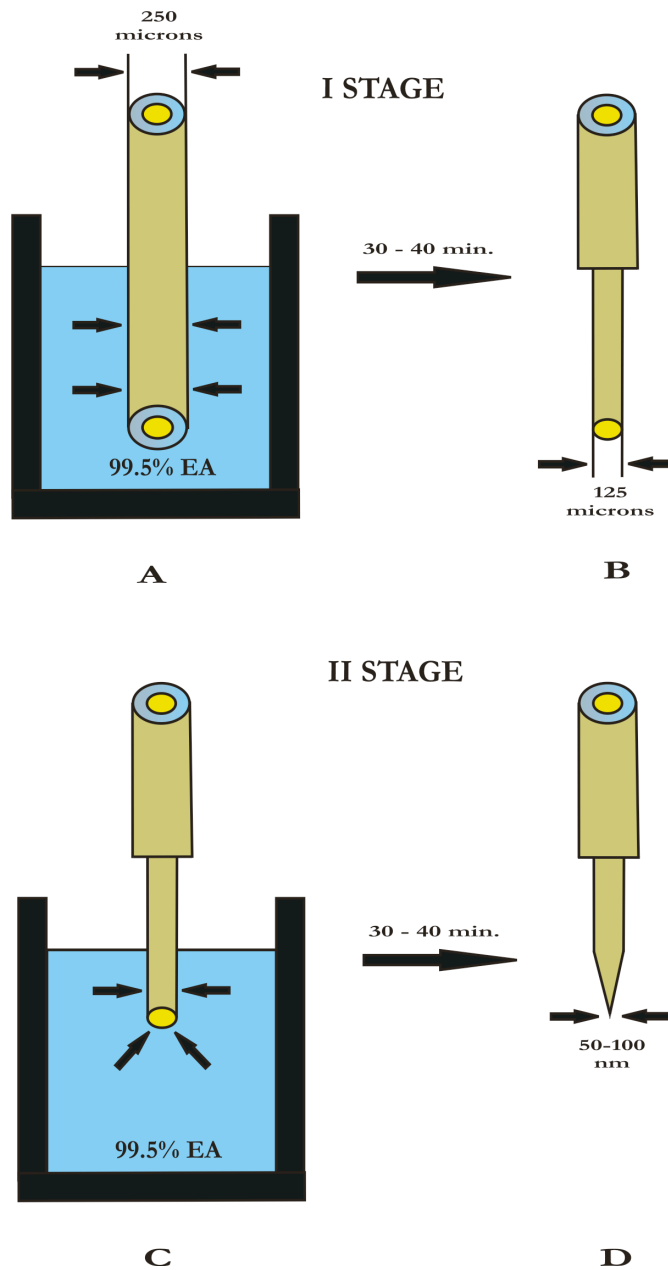


Fig. 41 Etching rate of POF in various solvents [100].

Two stages etching procedure was used: At the *first* stage the ca. 2 cm-length portion of the fiber was submerged into ethyl acetate for 30-40 minutes (see Fig. 42 **A**). As a result, the diameter of the fiber has been ca. twice diminished and the external protective polymer film that coats the fiber was destroyed (see Fig. 42 **B**) [93]. The

statistics shows (around 30 POF nanoprobe were prepared) that after first stage of chemical etching of the fiber,  $\sim 125 \mu\text{m}$  in diameter is formed.



**Fig. 42** Two stages of chemical etching of POF nanoprobe in 99.5% Ethyl Acetate (EA). **I stage:** **A)** immersion in EA solution at 2 cm; **B)** after 30-40 min. of etching  $\sim 125 \mu\text{m}$  in diameter POF is formed; **II stage:** **C)** immersion only the tip of etched POF at 5-6 mm; **D)** after 30-40 min. of etching 50-100 nm sharp tip is formed with aspect ratio equal to 8-10.

At the *second* stage the end part (5-6 mm) of the bare fiber has been slowly submerged into the etching solution with the periodical agitation of the solvent-containing glass also for 30-40 minutes (see Fig. 42 **C**). Such a procedure results in the formation of the sharp conical tip (see Fig. 42 **D**) with the radius of curvature equal to 50 – 100 nm and an aspect ratio of 8 - 10. After etching the tips were rinsed in de-ionised water [93].

Scanning electron microscope image of a typical etched POF probe coated with a gold nanolayer in order to avoid charge effects during the imaging is presented in Fig. 43 [93].

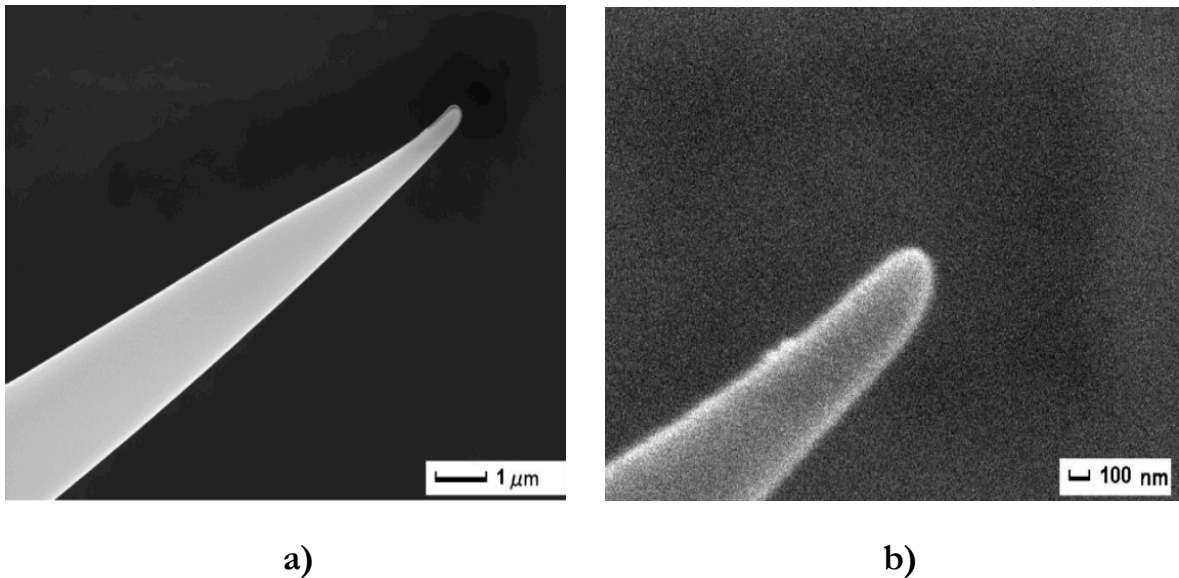


**Fig. 43** Scanning electron microscopy images of an etched POF nanoprobe. Scale bars are given in micron **a**) and nanometer **b**) [93].

Sharpened POF probes were glued onto the tuning fork using the “double resonance” operation principle first introduced in [56] and then successfully used for Scanning Near-field Optical Microscopy of different samples [55, 101]. The double resonant operation principle is such a montage of a fiber probe onto the tuning fork (see inset in Fig. 44) that the working frequency of the latter coincides with the resonance frequency of lateral dithering of a free standing part of the fiber beam *b* properly glued onto the tuning fork metal case *a*. In the paper [56] we experimentally demonstrated that such a montage enables to preserve a large quality factor of the

tuning fork after gluing the glass fiber probe onto it and also presented a theoretical model explaining such preservation [93].

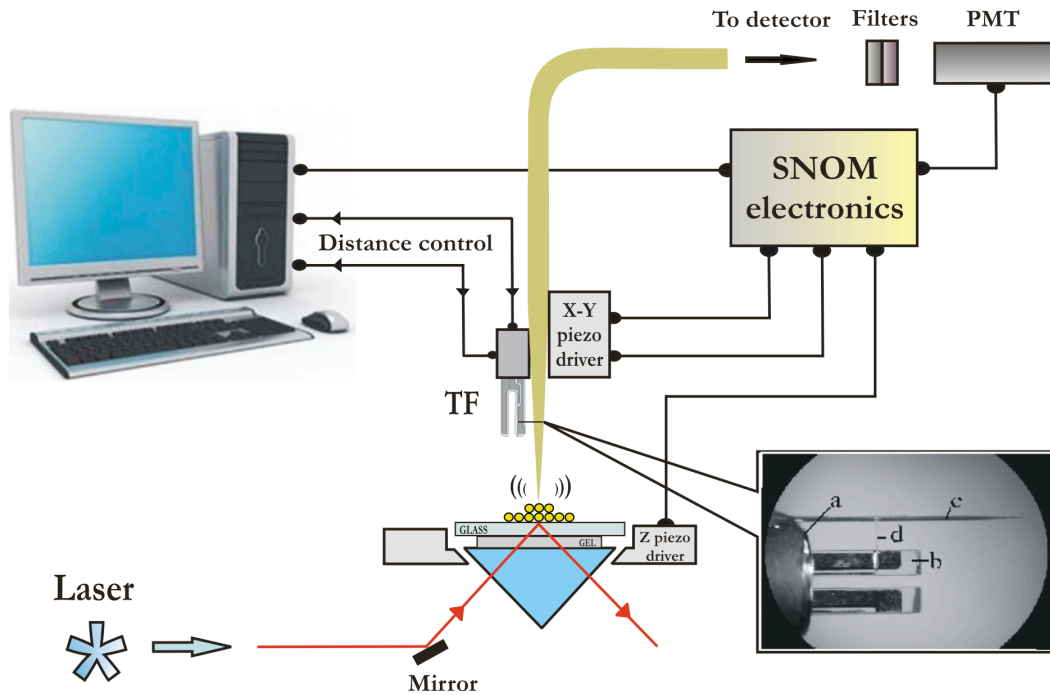


**Fig. 44** Schematic diagram of the experimental setup. In the insert the double resonant montage of a fibre probe (c) onto a tuning fork (b) is shown: a – metal case of a tuning fork, d – thin glass rod connecting probe and tuning fork [93].

Double resonant montage requires an accurate gluing and a careful control of the length of a free-standing part of the fiber beam as well as of the position where thin glass connector between a probe and a tuning fork is to be glued. It was experimentally established that for a standard 125 micron-diameter sharpened glass fiber resonance condition holds when the length of a free-standing part of the fiber beam is equal to  $4.8 \pm 0.1$  mm [56]. Based on the well known formula expressing the resonant frequencies of the dithering of a cylindrical beam whose one end is clamped and other is free:

$$\omega = \frac{\alpha_n^2}{l^2} \sqrt{\frac{EI}{\rho S}}$$

(here  $I = \frac{1}{4} \pi r^4$  is the inertia moment,  $l$ ,  $r$  are the length and the radius of the cylindrical rode,  $E$ ,  $\rho$  – Young modulus and density of the material it is made of,  $S = \pi r^2$  and  $\alpha_n$

is a numerical constant characterizing  $n$ th resonance:  $\alpha_1 = 1.875$ ,  $\alpha_2 = 4.694$ , etc. [102]), we obtain the scaling rule how this double resonant montage is to be effected for different materials: for this, the number

$$\eta = \frac{r}{l^2} \sqrt{\frac{E}{\rho}}$$

should be kept constant. This formula was the starting point to determine the optimal probe parameters, but it turned out that both Young modulus and density of PMMA varied broadly hence careful experimental adjustment of the plastic fiber probe montage conditions were necessary. The best results were obtained when the diameter of a probe was around 0.125 mm (twice diminished by etching in comparison with the initial diameter, see above) and the length was equal to  $3.4 \pm 0.1$  mm. The distance between the drive  $d$  (Fig. 44; glass rod with the diameter of 20  $\mu\text{m}$  was used as a drive) and the tuning fork case was fixed at  $1.4 \pm 0.1$  mm [93].

Such a montage of the PMMA fiber probe onto the tuning fork results in a large quality factor  $Q$  of the sensor: the initial value of  $Q = 10,000 - 11,000$ , which is characteristic for a free unloaded tuning fork in air, drops down to the values of  $Q = 2,000 - 6,000$  after proper gluing of a plastic fiber probe onto it. These values are quite comparable with those obtained earlier for glass fibers [56]. Such large mechanical quality factors attained enable us to use the specialized low noise, precise and fast electronics measuring the resonant frequency  $f_{res}$  and  $Q$ -factor of a tuning fork to control the SNOM operation. Two different electronics equipments, viz. the proprietary electronics earlier designed essentially for the sensors made by a tuning fork and an AFM cantilever glued on it [55, 70], and a commercially available electronics from Nanonis SA, Switzerland, specially adapted to work with this particular SNOM, were exploited [93].

To avoid complications related with the necessity to prepare metal – coated sharpened aperture probe (this work is currently in progress), at this demonstrational stage we used a Photon Scanning Tunneling Microscope (PSTM) [10, 11, 97, 19] for the operation in the near-field, see Fig. 48. In PSTM, the sample is illuminated by an evanescent wave produced by total internal reflection and the optical field of the

sample is probed by locally frustrating the evanescent field over it with an uncoated tapered optical fiber probe. The same SNOM as reported in this Thesis was adapted to operate in this PSTM regime. The samples were deposited onto thin glass plate placed onto the glass prism surface with a drop of the index matching gel (Cargille Laboratories, Ceder Grove, NJ, USA). A 488 nm argon ion laser with the power diminished to 2.5 mW (Spectra Physics) was used to illuminate the sample. A 488 nm Holographic Notch filter (Kaiser Optical Systems, Inc., USA) was inserted to cut off the excitation laser light, the fluorescence was detected by the PMT MP942 (Perkin Elmer) working in a single photon counting mode [93].

### **5.3 Results and discussion**

In Fig. 45 we present shear force topographical images of a TGQ 1 calibration grating (NT-MDT Company, Russia) and densely packed 1.0  $\mu\text{m}$  diameter fluorescent polystyrene microspheres 488/560 nm (T-8880, Molecular Probes Inc., Oregon, USA) on thin glass slide surface obtained using PMMA fiber probes and the SNOM under discussion. To better illustrate the performance of our SNOM, in Fig. 46 we present a shear force topographical image of single Lambda Mix Marker 19 #SM0231 DNA molecules (Fermentas, Ontario, Canada), which in our opinion is among the best topographical images of DNA molecules obtained by a scanning probe microscopy of any type. DNA molecules with the concentration of 1  $\mu\text{g}/\text{ml}$  were deposited onto the APTES-functionalized mica surface as discussed in [103]. High topographical resolution of these images demonstrates that a few nanometer-size “whiskers” and/or other irregularities are often present on the surface of generally smooth (see Fig. 43) PMMA tip apex [93].

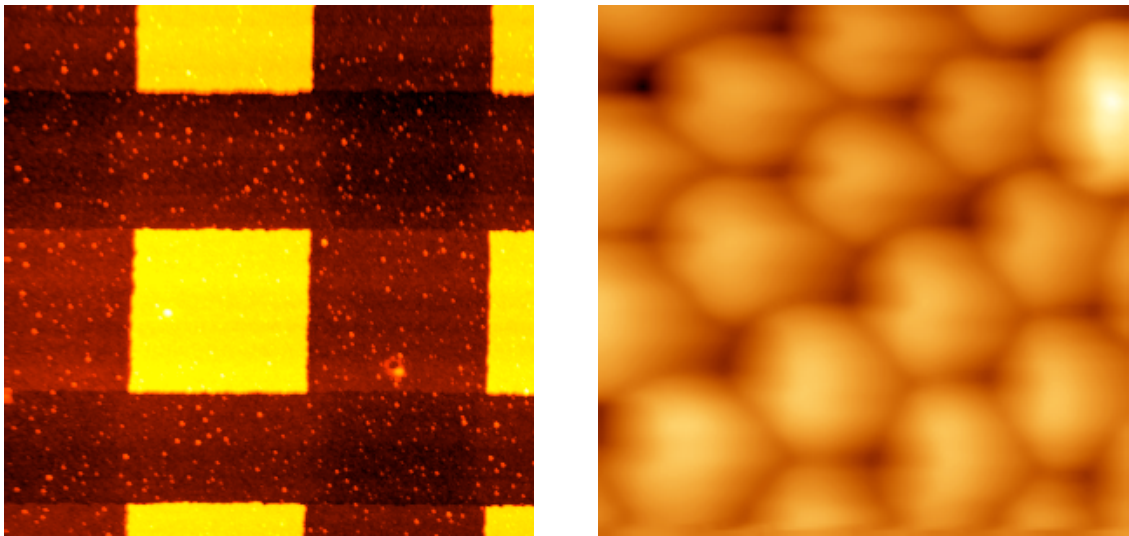


**Fig. 45** Left: Shear force topographical images of TGQ 1 calibration grating with the period of 3 microns and the rectangle height of 20 nm, NT-MDT, Moscow, Russia. Image size 4.5 x 4.5  $\mu\text{m}$ . Right: Densely packed fluorescent polystyrene 1  $\mu\text{m}$ -diameter beads. Image size 6 x 6  $\mu\text{m}$ . The only image processing is the Z-plane correction, images are presented without the scanner nonlinearity compensation [93].

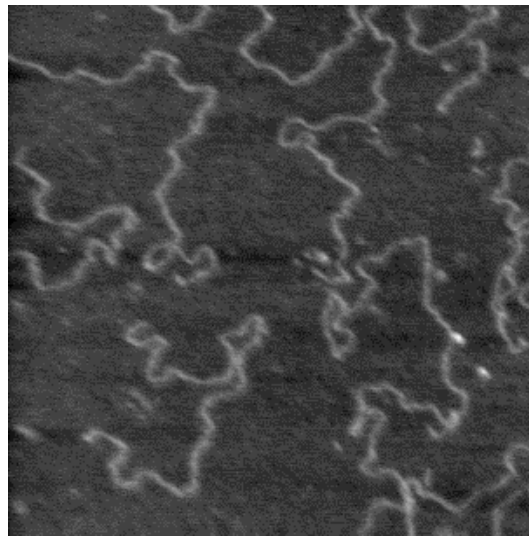


**Fig. 46** Shear force topographical image of single Lambda DNA molecules on mica. Constant amplitude mode of the Nanonis SA, Switzerland, SNOM controller was used as a feedback source. Scan size: 2.2 x 2.2  $\mu\text{m}$  [93].

Densely packed fluorescent beads in Fig. 45 were prepared by simple drying of a drop of a bead solution on the glass slide surface. This results in multilayer bead coating, which does not enable to achieve the near-field optical resolution. Such a resolution is illustrated in Fig. 47 where the isolated fluorescent beads are seen. These samples were prepared as follows. Water solutions of fluorescent polystyrene microspheres 488/560 nm of 0.1  $\mu\text{m}$  and 1  $\mu\text{m}$  diameter (T-8872 and T-8880



respectively, Molecular Probes Inc., Oregon, USA) with the initial concentration 2% vol. were, each, diluted 1000 times. Then one drop (10 – 20  $\mu\text{l}$ ) of each solution was deposited onto the glass slide surface and dried in air. Beforehand these glass slides were pre-treated with 0.1% Poly-L-Lysine solution (P8920, Sigma-Aldrich) by submerging them into this solution for 30 minutes and then drying in air for 5 - 6 hours. As follows from experimental results, such a deposition procedure enables to prepare samples where isolated fluorescent beads are present. No displacement of the beads during the scanning was observed which is due to both the reasonably strong adhesion of the beads to the poly-lysine-treated glass surface and small acting forces characteristic [55] for this SNOM cf. [93].

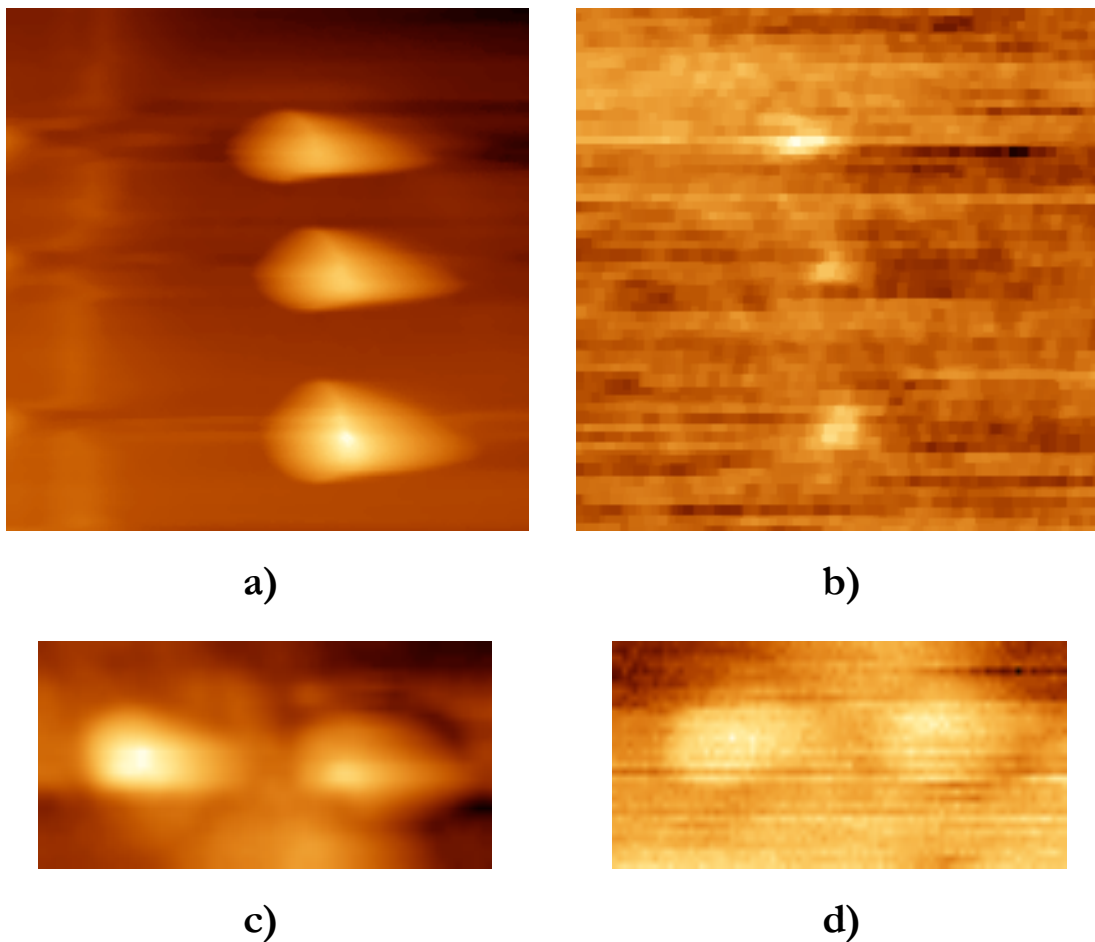


**Fig. 47** Shear force topographical images of **a)** isolated 1  $\mu\text{m}$ -diameter fluorescent beads and **c)** 100 nm-diameter fluorescent beads. Corresponding near-field optical images are presented in **b)** and **d)**. Image sizes: 6  $\mu\text{m}$   $\times$  6  $\mu\text{m}$  and 300 nm  $\times$  700 nm respectively. Constant quality factor mode of the SNOM controller electronics [55, 56] was used as a feedback source [93].

Of course, the samples under the study are not flat, hence topographical artefacts can not be excluded, see e.g. [75, 76], and these images should not be taken for the quantitative estimation of the near-field optical resolution achieved. Such quantitative study will be performed after the preparation of plastic fiber probes with the subwavelength-size aperture for the light transmission, which is currently in progress. Important is that they, together with the topographical images presented above, unambiguously attest the successful realization of PMMA fiber probes for SNOM [93].

## 5.4 Conclusion

We have reported the first use of a PMMA fiber probes for Scanning Near-field Optical Microscopy. Preparation of these probes is easy and does not require any hazardous materials and/or procedures. The hydrophobic nature of the plastic fiber surface and relative easiness of its chemical modification also can be advantageous for certain cases. What is probably the most important, these probes do demonstrate much less fragility than the glass fiber-made probes: days of intensive work for one probe were many times achieved. We believe that all these factors promise broad perspectives for the probes under discussion [93]. In addition, due to increasing interest on application of PMMA optical fibers in optical research, particularly in SNOM domain, recently in **Microscopy and Analysis** (Issue 129, p. 30, April 2010) our paper in [93] has been highlighted as promising scanning probe sensor for SNOM research.

# Appendix I

## Preparation of glass optical fiber probes

In SNOM experiments, the use of a glass optical fiber plays an important role, as this is the probe that allows obtaining of topographical and optical data and investigating the sample. It is well known that to increase the optical resolution of the fibers, it is necessary to collect the laser light at the end of the fiber tip. Therefore, the cone angle of the apex plays a fundamental role since it reduces the propagation path for the evanescent field inside the fiber as well as the losses due to the multiple internal reflections. A larger cone angle (aspect ratio) produces a more efficient probe while preserving the resolution [67].

Today, there is no problem to produce sharp optical fibers for preparation of SNOM sensors. Moreover, there are several ways of fabrication of sharp tips. The first method is based on “heating and pulling” [68], and the second on the chemical “tube-etching” method [69].

Stöckle *et al.* suggest microconvection model (this is similar to tube-etching process), where transient capillary effects explain the etching process. Initially, due to geometrical constraints, it is expected that the outer regions of the fiber are etched slightly faster than the center. This is attributed to the fact that at the rim of the glass cylinder, HF supply occurs out of a larger volume as compared to the central region (see Fig. 48 (a)). This effect starts the formation of a conical shape. As soon as the preliminary taper is formed, convection starts to deliver Hydrofluoric Acid (HF) to the upper region of the cone as shown in Fig. 48 (b) [69].

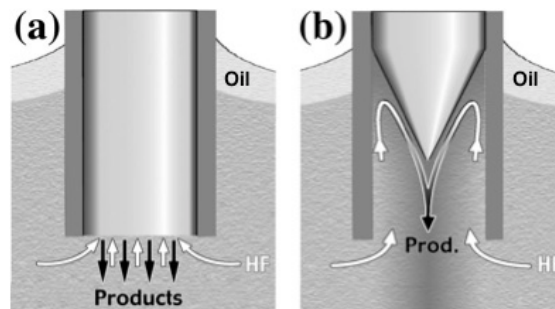


**Fig. 48** The schematic of the “convection mechanism” involved in tube etching method in HF: **a)** Initial diffusion-controlled etching, and **b)** convection-controlled tip formation inside the tube [69].

In this section, we will emphasize the chemical tube-etching method, with standard 125 microns single mode glass optical fibers (3M, SA Telecommunications, Switzerland), and Hydrofluoric Acid 40% (Fluka, Chemika, Switzerland) as an etchant solution. The main purpose of this section is to describe the tube-etching process, and show the technical manipulations for the sharp tip formation of the glass optical fiber.

Following the literature [67, 69], we had partially adopted the chemical tube-etching method in our laboratory, and that includes the following steps: the *first* step, is the proper mounting the several fibers (fixation of all fibers at the same level in fiber holder) into the “fiber holder” (see Fig. 49). The *second* step, is to submerge these fibers into HF solution (around 20-25 mm in depth) for 120 minutes at room temperature (22-23°C). The surface of the HF solution was covered by a layer of 5-6 mm of “vacuum oil”, in order to avoid the corrosive/hazardous evaporation. In Fig. 49 we show the setup for chemical tube-etching method.

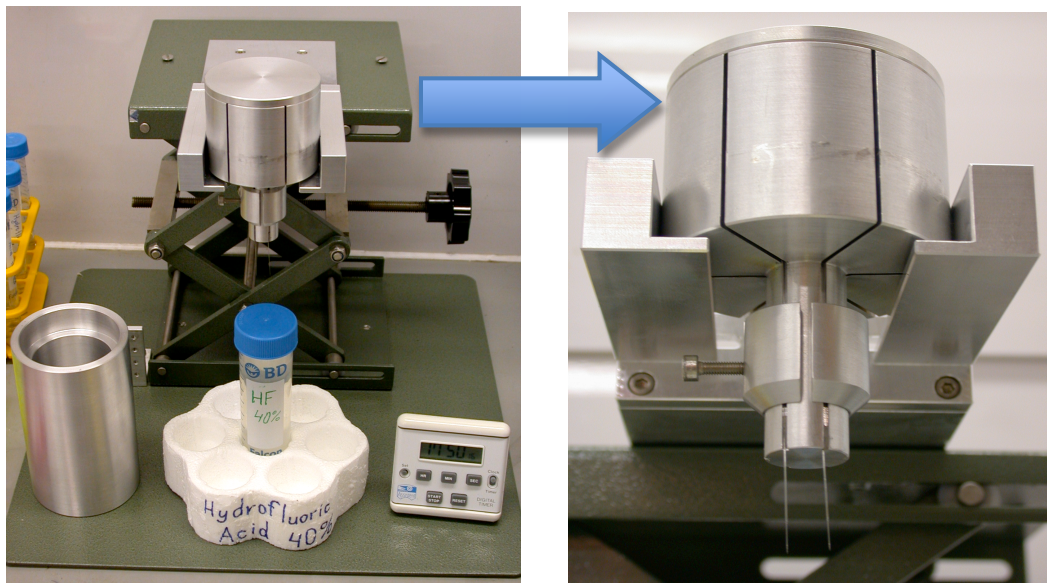


**Fig. 49** The technical facilities for chemical etching of glass optical fibers by “tube-etching” method in HF solution. Fiber holder (right image) is intended to keep six fibers at the same level.

The *third* step is to extract the fibers from the HF solution, and wash them several times in the Ethanol 96% solution (Fluka, Chemika, Switzerland) and in the nanopure de-ionized water afterwards (Labtec, Services AG, Switzerland). The *fourth* and last step, is to remove the protective polymer film by 127 microns “fiber optical stripper” (NO-NIK, Cornwell, USA). After all these stages, the smooth and sharp tips are formed for the further preparation of SNOM sensors, and these procedures can be easily reproduced. In Fig. 50 we show two images of home made uncoated optical fibers obtained by the described method.

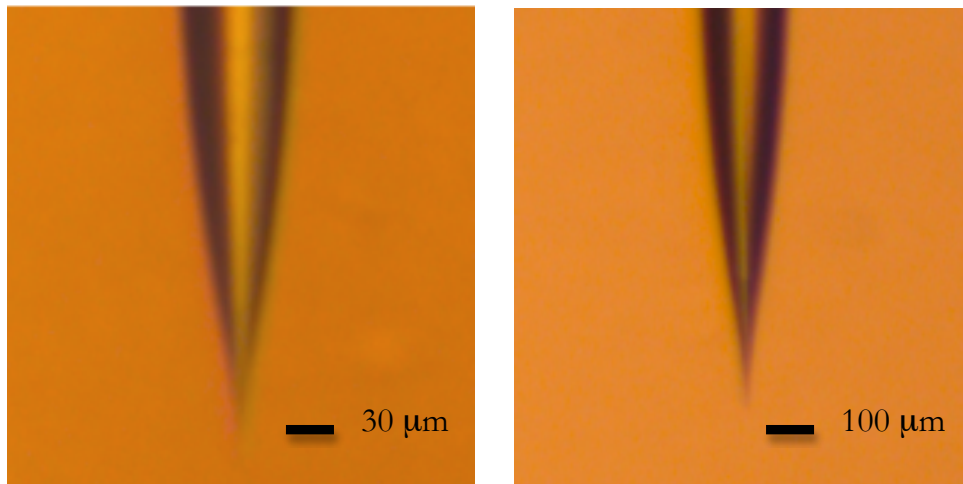
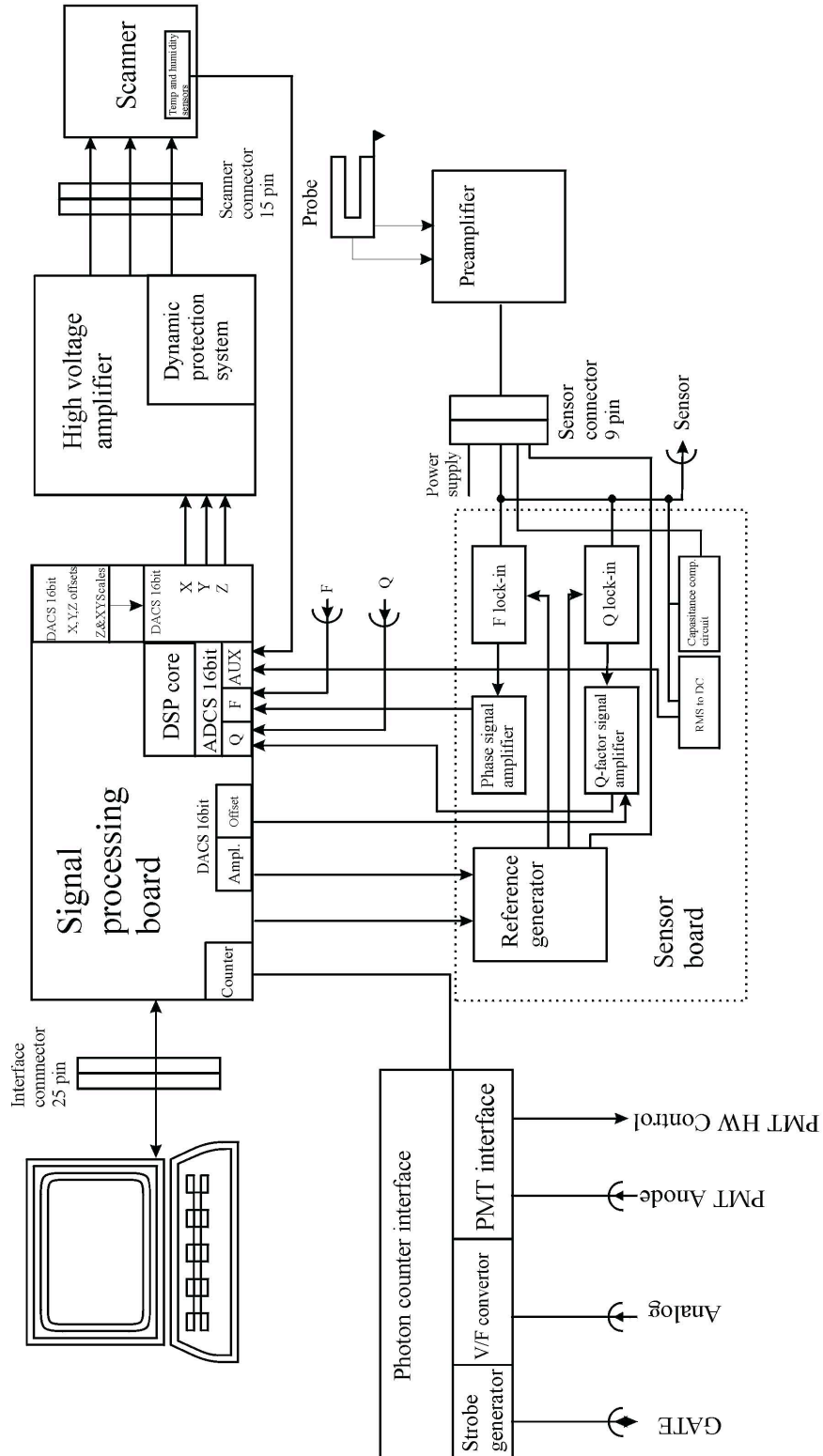


**Fig. 50** The photography's of two different home made uncoated glass optical fibers. Images made through the eyepiece 16x/16 of Leica EZ5 Stereomicroscope (Leica Microsystems AG, Switzerland). Scale bar is given in microns.

# Appendix II

## Schematic diagram of electronics of our SNOM

$F$  – signal corresponding to the resonance frequency,  $Q$  – signal corresponding to the quality factor,  $AUX$  – auxiliary signal.  $DAC$ ,  $ADC$  – digital-to-analog and analog-to-digital converters,  $DSP$  – digital signal processor.

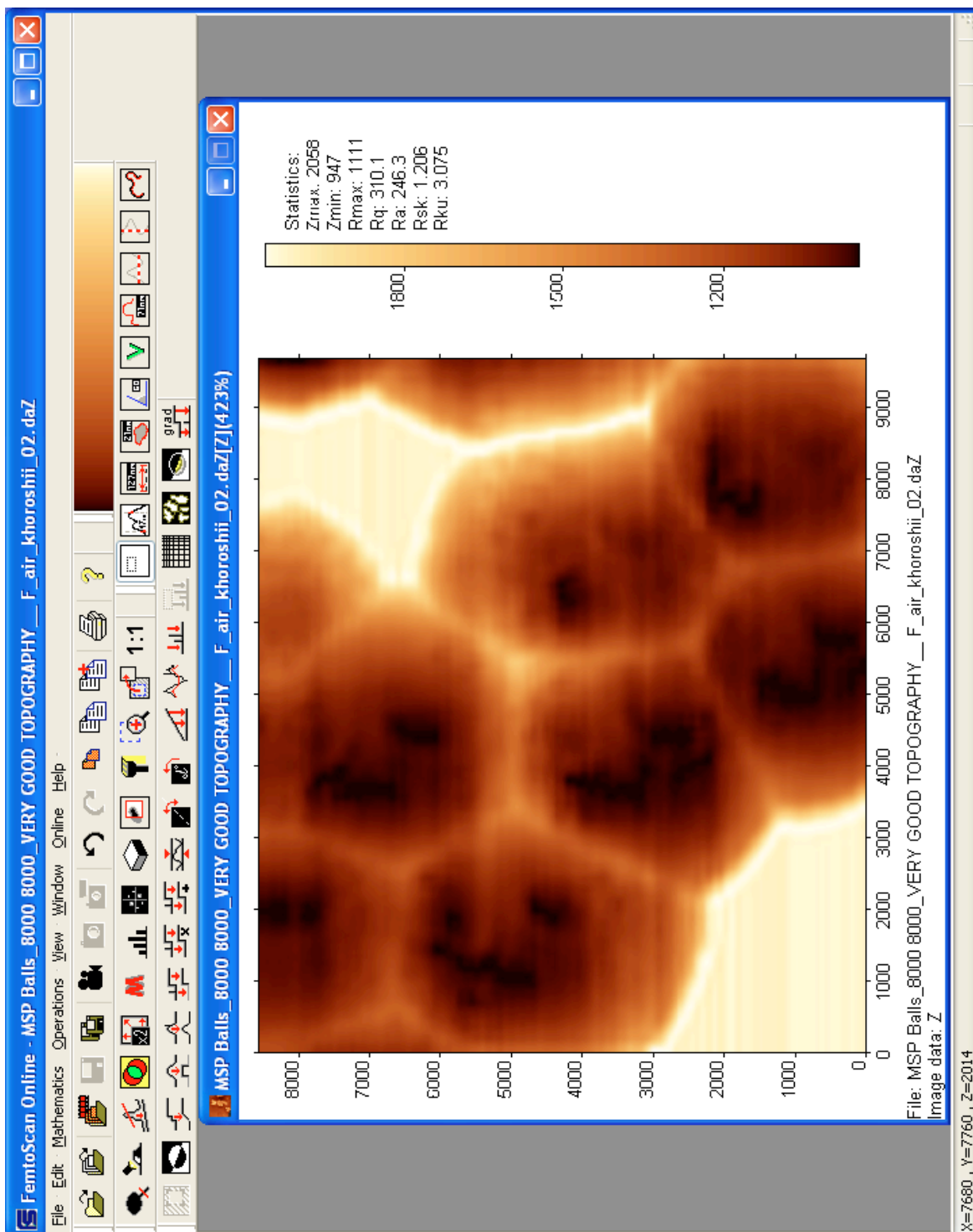


SPM block diagram

# Appendix III

## Interface of FemtoScan (version 2.2.96) program used for XYZ motion of the sample

See URL: <http://www.nanoscopy.net/en/Femtoscanner-V.shtm>



# Appendix IV

Interface of UsScope (version 1.0.2.33) program used for 2D and 3D analysis of the sample

The screenshot displays the UsScope software interface, version 1.0.2.33. The main window is titled "UsScope - NSOM processor Ver 2.06". The interface is divided into several functional areas:

- Top Panel:** Includes "Contact Search" with a "Light" button, "Move to:" fields for X (nm) and Y (nm), and "Step" navigation controls. The "Z Feedback" section shows Channel F, On, Offset (-0.300 V), Gain (-0.500 nm/V), Tconst (1.000 msec), and Limit (50 %).
- Left Panel:** Features "Auto Range" and "Auto Offset" sliders, and a "Scan" button.
- Center Plot:** A 2D plot showing current (mV) on the y-axis (ranging from 0 to 50) and time (ms) on the x-axis (ranging from 0 to 40). The plot displays two traces: a red trace and a yellow trace. The y-axis is labeled "mV" and the x-axis is labeled "ms".
- Right Panel:** Contains "Scale Factor" (XY: 1.000, Z: 1.000), "Z Offset, nm" (User: 0.0, Auto: 0.0), "Surface Sensor" (Adjust: F = 32807.60 Hz, I = 4.9 nA, Compensation: 0), "PMT Voltage" (0.0 V), "Voltage On" (-1268.3871 mV), and "Scope On" controls.
- Bottom Panel:** Includes "ImageMode" (Q, F, Photo, Z), "Scan parameters" (Minimum, Maximum, Resolution, pixel for X and Y; Scan speed, Retrace speed, Estimated scan time), and "Save Trace" and "Approach curve" buttons.



# Bibliography

- [1] Birdi K. S., Scanning Probe Microscopes Applications in Science and Technology, Print ISBN: 978-0-8493-0930-4, CRC Press (2003).
- [2] Heinzelmann H. and Pohl D. W., *Appl. Phys. A: Solids and Surfaces*, **59**, p. 89 (1994).
- [3] See URL: [http://www.azonano.com/details.asp?ArticleID=1483#\\_The\\_Near-Field\\_Scanning\\_Optical\\_Mic](http://www.azonano.com/details.asp?ArticleID=1483#_The_Near-Field_Scanning_Optical_Mic).
- [4] Bouhelier A., *Encyclopedia of Materials: Science and Technology*, ISBN: 978-0-0804-3152-9, p. 1 (2010).
- [5] Pohl D. W., Denk W. and Lanz M., *Appl. Phys. Lett.*, **44**, p. 651 (1984).
- [6] Lewis A., Isaacsson M., Harootunian A. and Murray A., *Ultramicroscopy*, **13**, p. 227 (1984).
- [7] Bouhelier A., “Nanoscale Optical Imaging and spectroscopy”, *Encyclopedia of Materials: Science and Technology*, ISBN: 978-0-0804-3152-9, p. 1 (2008).
- [8] Synge E. H., *Phil. Mag.*, **6**, p. 356 (1928).
- [9] Greffet J. J. and Carminati R., *Prog. Sur. Sci.*, **56**, p. 133 (1997).
- [10] Paesler M. A. and Moyer P. J., “Near-field Optics: Theory, Instrumentation, and Applications”, *John Wiley and Sons*, New York (1996).
- [11] Courjon D., “Near Field Microscopy and Near Field Optics”, *Imperial College Press*, London (2003).
- [12] Betzig E. and Trautman J. K., *Science*, **257**, p. 189 (1992).
- [13] Betzig E., Lewis A., Harootunian A., Isaacson M and Kratschmer E., *Biophys. Journ.*, **49**, p. 269 (1986).
- [14] Düring U., Pohl D. W. and Rohner F., *Journal of Applied Physics*, **59**, p. 3318 (1986).

- [15] Abbe E., *Archiv für mikroskopische Anatomie*, **9**, p. 413 (1873).
- [16] Courjon D., Bainier C., Girard C. and Vigoureux J. M., *Ann. Physik*, **2**, p. 149 (1993).
- [17] Fischer U. C., Heimel J., Maas H.-J., Fuchs H., Weeber J. C. and Dereux A., *Topics Applied Physics* (J. Tominaga and D. P. Tsai, eds.: Optical Nanotechnologies), Berlin-Heidelberg, **88**, p. 141 (2003).
- [18] Rayleigh Lord, *Philosophical Magazine*, **5**, p. 167 (1896).
- [19] Zayats A. and Richards D., “Nano-optics and Near-field Optical Microscopy”, *Artech House Series: Nanoscale Science and Engineering* (Eds. Zhang X. and Wang K. L.), p. 6 (2009).
- [20] See URL: <http://nam.epfl.ch/research/14.html>.
- [21] See URL: <http://www.azonano.com/details.asp?ArticleID=1205>.
- [22] Harootunian A., Betzig E., Isaacson M. and Lewis A., *Appl. Phys. Lett.*, **49**, p. 674 (1986).
- [23] Kim J. H. and Song K.-B., *Micron*, **38**, p. 409 (2007).
- [24] Betzig E., Isaacson M. and Lewis A., *Appl. Phys. Lett.*, **51**, p. 2088 (1987).
- [25] Courjon D., Sarayeddine K. and Spajer M., *Opt. Commun.*, **71**, p. 23 (1989).
- [26] Reddick R. C., Warmack R. J. and Ferrell T. L., *Phys. Rev. B*, **39**, p. 767 (1989).
- [27] Tsai D. P., Kovacs J. and Moskovits M., *Ultramicroscopy*, **57**, p. 130 (1995).
- [28] Krenn J. R., Dereux A., Weeber J. C., Bourillot E., Lacroute Y., Goudonnet J. P., Schider G., Gotschy W., Leitner A., Aussenegg F. R. and Girard C., *Phys. Rev. Lett.*, **82**, p. 2590 (1999).
- [29] Fischer U. C. and Pohl D. W., *Phys. Rev. Lett.*, **62**, p. 458 (1989).
- [30] Zenhausern F., O’Boyle M. P. and Wickramasinghe H. K., *Appl. Phys. Lett.*, **65**, p.1623 (1994).
- [31] Zenhausern F., Martin Y. and Wickramasinghe H. K., *Science*, **269**, p. 1083 (1995).
- [32] Inouye Y. and Kawata S., *Opt. Lett.*, **19**, p. 159 (1994).
- [33] Kawata S. and Inouye Y., *Ultramicroscopy*, **57**, p. 313 (1995).

- [34] Gleyzes P., Boccara A. C. and Bachelot R., *Ultramicroscopy*, **57**, p. 318 (1995).
- [35] Bachelot R., Gleyzes P. and Boccara A., *Appl. Opt.*, **36**, p. 2160 (1997).
- [36] Sugiura T., Kawata S. and Okada T., *J. Microsc.*, **194**, p. 291 (1999).
- [37] Knoll B. and Keilmann F., *J. Microsc.*, **194**, p. 512 (1999).
- [38] Zanten van T. S., Lopez-Bosque M. J. and Garcia-Parajo M. F., *Small*, **6** (2), p. 270 (2010), DOI: 10.1002/smll.200901204.
- [39] Zanten van T. S., Cambi Alessandra and Garcia-Parajo M. F., *Biochimica et Biophysica Acta*, **1798**, p. 777 (2010).
- [40] Westphal V. and Hell S. W., *Phys. Rev. Lett.*, **94**, p.143903 (2005).
- [41] Donnert G., Keller J., Medda R., Andrei M. A., Rizzoli S. O., Luhrmann R., Jahn R., Eggeling R. and Hell S. W., *PNAS USA*, **103**, p. 11440 (2006).
- [42] Willig K. I., Rizzoli S. O., Westphal V., Jahn R. and Hell S. W., *Nature*, **440**, p. 935 (2006).
- [43] Sieber J. J., Willig K. I., Kutzner C., Gerding-Reimers C., Harke B., Donnert G., Rammner B., Eggeling C., Hell S. W., Grubmuller and Lang T., *Science*, **317**, p. 1072 (2007).
- [44] Kellner R. R., Baier C. J., Willig K. I., Hell S. W. and Barrantes B. J., *Neuroscience*, **144**, p. 135 (2007).
- [45] Westphal V., Rizzoli S. O., Lauterbach M. A., Kamin D., Jahn R. and Hell S. W., *Science*, **320**, p. 246 (2008).
- [46] Eggeling C., Ringemann C., Medda R., Schwarzmann G., Sandhoff K., Polyakova S., Belov V. N., Hein B., Middendorff von C., Schonle A. and Hell S. W., *Nature*, **457**, p. 1159 (2009).
- [47] Gustafsson M. G. L., *PNAS USA*, **102**, p. 13081(2005).
- [48] Schermelleh L., Carlton P. M., Haase S., Shao L., Winoto L., Kner P., Burke B., Cardoso M. C., Agard D. A., Gustafsson M. G. L., Leonhardt H. and Sedat J. W., *Science*, **320**, p. 1332 (2008).
- [49] Gustafsson M. G. L., Shao L., Carlton P. M., Wang C. J. R., Golubovskaya I. N., Cande W. Z., Agard D. A. and Sedat J. W., *Biophys. J.*, **94**, p. 4957 (2008).
- [50] Pielage J., Cheng L., Fetter R. D., Carlton P. M., Sedat J. W. and Davis G. W., *Neuron*, **58**, p. 195 (2008).

- [51] Betzig E., Patterson G. H., Sougrat R., Lindwasser O. W., Olenuch S., Bonifacino J. S., Davidson M. W., Lippincott-Schwartz J. and Hess H. F., *Science*, **313**, p. 1642 (2006).
- [52] Hess S. T., Girirajan T. P. K. and Mason M. D., *Biophys. Jour.*, **91**, p. 4258 (2006).
- [53] Rust J., Bates M. and Zhuang X., *Nature Methods*, **3**, p. 793 (2006).
- [54] Cao G., “Nanostructures and nanomaterials, Synthesis, Properties and Applications”, *Imperial College Press*, p. 326 (2004).
- [55] Serebryakov D. V., Sekatskii S. K., Cherkun A. P., Dukenbayev K., Morozov I. V., Letokhov V. S. and Dietler G., *Journal of Microscopy*, **229**, p. 287 (2008).
- [56] Cherkun A. P., Serebryakov D. V., Sekatskii S. K., Morozov I. V. and Letokhov V. S., *Rev. Sci. Instr.*, **77**, p. 033703 (2006).
- [57] Dukenbayev K., Sekatskii S. K., Serebryakov D. V., Zayats A. V. and Dietler G., *Proceedings of the SPIE*, **6728**, p. 67282D (2007).
- [58] Rensen W. H. J., Van Hulst N. F. and Kammer S. B., *Appl. Phys. Lett.*, **71**, p. 1557 (2000).
- [59] Lei F. H., Angiboust J.-F., Qiao W., Sockalingum G. D., Dukic S., Chrit L., Troyon M. and Manfait M., *J. Microsc.*, **216**, p. 229 (2004).
- [60] Moyer P. J. and Kammer S. B., *Appl. Phys. Lett.*, **68**, p. 3380 (1996).
- [61] Lambelet P., Pfeffer M., Sayah A. and Marquis-Weible F., *Ultramicroscopy*, **71**, p. 117 (1998).
- [62] Taylor R. S., Vobornik D., Lu Z., Chisholm R. A. and Johnston L. J., *Jour. Of Appl. Phys.*, **107**, p. 043526 (2010).
- [63] Naber A., *Journal of Microscopy*, **194**, p. 307 (1999).
- [64] Lapshin D. A., Reshetov V. N., Sekatskii S. K. and Letokhov V. S., *JETP Lett.*, **67**, p. 245 (1998).
- [65] Tsai P. and Lu Y. Y., *Appl. Phys. Lett.*, **73**, p. 2724 (1998).
- [66] Davydov D. N., Shelimov K. N., Haslett T. L. and Moskovits M., *Appl. Phys. Lett.*, **75**, p. 1796 (1999).
- [67] Hoepfener C., Siebrasse J. P., Peters R., Kubitscheck U. and Naber A., *Biophys. J.*, **88**, p. 3681 (2005).

- [68] Mensi M., Dukenbayev K., Sekatskii S. K. and Dietler G., *Laser Physics*, **20** (1), p. 78 (2010).
- [69] Barbic M., Eliason L. and Ranshaw J., *Sensors and Actuators A*, **136**, p. 564 (2007).
- [70] Serebryakov D. V., Cherkun A. P., Loginov B. A. and V. S. Letokhov, *Rev. Sci. Instr.*, **73**, p. 1795 (2002).
- [71] Koopman M., Bakker B. I., Garcia-Parajo M. F. and Van Hulst N. F., *Appl. Phys. Lett.*, **83**, p. 5083 (1999).
- [72] Karrai K. and Grober R. D., *Appl. Phys. Lett.* **66**, p. 1842 (1995).
- [73] Karrai K. and Grober R. D., *Ultramicroscopy*, **61**, p. 197 (1995).
- [74] Kumbhakar M., Nath S., Mukherjee T., Mittal J. P. and Pal H., *Journal of Photochemistry and Photobiology C: Photochemistry Reviews*, **5**, p. 113 (2004).
- [75] Hecht, B., Bielefeldt, H., Inouye, Y., Pohl, D.W. and Novotny, L., *J. Appl. Phys.* **81**, p. 2492 (1997).
- [76] Sandoghdar, V., Wegscheider, S., Krausch, G. and Mlynek, J., *J. Appl. Phys.* **81**, p. 2499 (1997).
- [77] Feng P., Weagant S. D. and Grant M. A., Chapter 4: "Enumeration of *Escherichia coli* and the Coliform Bacteria", *Bacteriological Analytical Manual*, (2002).
- [78] See URL: [http://www.cdc.gov/nczved/divisions/dfbmd/diseases/ecoli\\_o157h7/index.html#what](http://www.cdc.gov/nczved/divisions/dfbmd/diseases/ecoli_o157h7/index.html#what).
- [79] Bolshakova A. V., Kiselyova O. I., Filonova A. S., Frolova O. Y., Lyubchenko Y. L. and Yaminsky I. V., *Ultramicroscopy*, **86**, p. 121 (2001).
- [80] See URL: [http://en.wikipedia.org/wiki/Bacterial\\_cell\\_structure](http://en.wikipedia.org/wiki/Bacterial_cell_structure).
- [81] Dukenbayev K., Dittrich, Mensi M., Sekatskii S. K. and Dietler G., Abstract book of *10<sup>th</sup> International Conference on Near-Field Optics, Nanophotonics and Related Techniques*, p. 141 (2008).
- [82] Singh S. P., Häder D. - P. and Sinha R. P., *Ageing Research Reviews*, **9**, p. 79 (2010).
- [83] Zubkov M. V., Sleigh M. A., Burkill P. H., *Aquatic Microbiol. Ecol.*, **21**, p. 13 (2000).
- [84] Kouzminov F. I., Maximov E. G., Gorbunov M. Y. and Fadeev V. V., *Proceedings of Book: SPIE Conference Photonics*, Paper 7715-70, Bruxelles, Belgium 2010.
- [85] Flores E. and Herrero A., *Nature Review / Microbiology*, **8**, p. 39 (2010).

- [86] Vincent W. F., Cyanobacteria, *Encyclopedia of Inland Water*, p. 226 (2009).
- [87] Dignum M, Hoogveld H. L., Matthijs H. C. P., Laanbroek H. J. and Pel R., *FEMS Microbiology Ecology*, **48**, p. 29 (2004).
- [88] Andrizhiyevskaya E. G., Schwabe T. M. E., Germano M., Haene S., Kruij S., Grondellea R. V. and Dekker J. P., *Biochimica et Biophysica Acta*, **1556**, p. 265 (2002).
- [89] Kaňa R., Prášil O., Komárek O., Papageorgiou G. C. and Govindjee, *Biochimica et Biophysica Acta*, **1787**, p. 1170 (2009).
- [90] Nägeli C., Gattungen einzelliger Algen, physiologisch und systematisch bearbeitet, *Neue Denkschr. Allg. Schweiz. Ges. Naturwiss.*, **10**, pp. 1–138 (1849).
- [91] Proteau P. J., Gerwick W. H., Garcia-Pichel F. and Castenholz R., *Experientia*, **49**, Birkh/iuser Verlag, CH-4010 Basel, Switzerland (1993).
- [92] Stamatakis K., Ladas N. P., Alygizaki-Zorba A. and Papageorgiou G. C., *Archives of Biochemistry and Biophysics*, **370** (2), p. 240 (1999).
- [93] Chibani H., Dukenbayev K, Mensi M, Sekatskii S. K. and Dietler G., *Ultramicroscopy*, **110**, p. 211 (2010).
- [94] See URL: <http://www.olympusmicro.com/primer/techniques/nearfield/nearfieldintro.html>.
- [95] Subramaniam V., Kirsch A. K., Pomar R. V. R. and Jovin T. M., *Journal of Fluorescence*, **7**, p. 381, (1997).
- [96] Paula A. M., Chaves C. R., Silva H. B. and Weber G., *Applied Optics*, **42**, 16, p. 3005 (2003).
- [97] Taha H., Strinkovski A., Manevitch A., Khatchatouriants A., Dekhter R., Ammann E. and Lewis A., *Nature Biotechnology*, **21**, p. 1378 (2003).
- [98] Ziemann O., Krauser J., Zamzow P. E. and Daum W., *Plastic Optical Fiber Handbook – Optical Short Range Transmission Systems*, Springer, Berlin (2008).
- [99] Polishuk P., *Fiber and Integrated Optics*, **27**, 1 (2008).
- [100] Im M. H., Park E. J., Kim C. H. and Lee M. S, in: *Human-Computer Interaction. Interaction Platforms and Techniques*, 4551, Springer, Berlin – Heidelberg (2007).
- [101] Sekatskii S. K., Dietler G. and Letokhov V. S., *Chem. Phys. Lett.*, **452**, p. 220 (2008).
- [102] Landau L. and Lifshitz E., *Theory of Elasticity*, Butterworth-Heinemann (1986).

[103] Adamcik J., Valle F. Witz G., Rechendorff K. and Dietler G., *Nanotechnology*, **19**, p. 384016 (2008).

[104] Spinelli A., Davis L. M. and Dautet H., *Rev. Sci. Instr.*, **67** (1), p. 55 (1996).

# Acknowledgements

The first and foremost I would like to express my deep and sincere gratitude to my supervisor Professor Giovanni Dietler. It has been an honor to be his first Ph.D. student from Kazakhstan. His wide knowledge and his logical way of thinking have been of great value for me. He has taught me, both consciously and unconsciously, how good experimental physics is done. I am also thankful for the excellent example he has provided as a successful physicist and as very good specialist. I appreciate all his contributions of time, ideas, and funding to make my Ph.D. experience productive and stimulating.

I would greatly grateful to my co-adviser Dr. Sergey K. Sekatskii, for his immense scientific and social support to make this PhD training fruitful and regulative. During these years I have learned from him many useful scientific and experimental knowledge's, which I am sure will play a key role in further academic career. His understanding, encouraging and personal guidance have proved an excellent basis for the present thesis.

I warmly thank to Dr. Dusan Vobornik, Dr. Andrzej Kulik, Dr. Sandor Kasas and Dr. Malgorzata Lekka for theirs valuable advices and friendly help. Theirs extensive discussions around my work and interesting explorations in operations have been very helpful for this thesis and other projects.

My sincere thanks are due to the official referees: 1) Professor Anatoly V. Zayats, Head of Experimental Biophysics & Nanotechnology, Director of Research Program on Nanoplasmonics, Department of Physics, King's College London, UK; 2) Professor Alexandra Radenovic, Head of Laboratory of Nanoscale Biology, Swiss Federal Institute of Technology of Lausanne, Switzerland; and 3) Dr. Valery V. Prokhorov, Institute of Mathematical Problems of Biology, Russian Academy of Sciences, Moscow region, Russia, for their detailed review, constructive criticism and excellent advice during the preparation of this thesis.

It is a pleasure to thank those who made this thesis possible to Dr. Mounir Mensi, Dr. Guillaume Witz, Dr. Suriya Murthy Nagamani and Haytham Chibani with whom I have closely worked on several projects on SNOM and general friendship. Thanks to them for enthusiasm and warm collaboration during all time.



During this work I have collaborated with many colleagues for whom I have great regards to: Fabrizio Benedetti, Alonso Sarduy Livan Bladimir, Jae Sun Jeon, Andrea Cerreta, Caroline Maillard, Carine Ben Abida, Andrey Mikhaylov and Dmitry Basmanov. I wish to extend my warmest thanks to all those who have helped me with my work in the Laboratory of Physics of Living Matter, and other friends within the our Institute of Physics of Biological Systems.

I would like to show my gratitude to our laboratory secretary Christine Vuichoud. Who kept us organized and was always ready to help. Whenever I come with administrative questions, she always gives me appropriate answer and makes my EPFL's campus life easier.

I would appreciate also to our former postdocs: Dr. Josef Adamcik, Dr. Giovanni Di Santo, Dr. Melanie Favre, Dr. Susana Tobenas and Dr. Alexander Yersin for their advices, help in samples preparation and with whom I shared this enjoyably scientific collaboration.

I am especially thanks to Michel Kessous, our “informatics man”, his technical and software assistance and always present to face the PC problems to resolve, and mechanical workshop stuff to Jean-Rene Moser, Alain Pinard, Rodolfo Ganzalez, Jean-Louis Marmilon, Bernard Howard and Jean-Marc Repond for the technical discussions and many prepared experimental SNOM tools and mechanical parts.

I gratefully acknowledge the funding source – the government of my country, which made my Ph.D. work possible. I was funded by international Presidential fellowship “Bolashak” for my 4 years, and to my previous supervisors Professor Baktybekov S. Kazbek and Dr. Myrzakhmet K. Marat, Eurasian National University by name L. N. Gumilev, Astana, Kazakhstan, for their yearly initiation and involving me to interesting scientific research life.

My time at EPFL was made enjoyable in large part due to the many friends and groups that become a part of my life. I am grateful for the time spent with friends, for our memorable trips into the mountains, and for many other people and memories.

Lastly, I would like to deeply thanks to my family for all their love and encouragement. For my parents and little brother Almat who raised me with a love of science and supported me in all my pursuits. And most of all for my loving, understandable, encouraging and patient wife Gulmira and son Alikhan whose faithful support during the final stages of this Ph.D. is so appreciated.

Lausanne, December 20, 2010

# Curriculum Vitae

---

## Kanat Dukenbayev

Laboratory of Physics of Living Matter,  
Institute of Physics of Biological Systems,  
Faculty of Basic Science, Swiss Federal Institute of Technology,  
CH-1015, Lausanne, Switzerland

Phone: +41 (0) 21 693 04 45 Fax: +41 (0) 21 693 04 22

E-mail: [kanat.dukenbayev@epfl.ch](mailto:kanat.dukenbayev@epfl.ch) Website: <http://lpmv.epfl.ch/>

---

## EDUCATION

- 02/2007-02/2011 Ph.D. in Science (in February, 2011),  
Swiss Federal Institute of Technology, Lausanne,  
Title of thesis: “Scanning Near-field Optical Microscopy  
of living cells in liquid, elaboration of new SNOM probes  
and detection methods”,  
Advisors: Prof. Giovanni Dietler  
and Dr. Sergey K. Sekatskii.
- 09/2000-07/2004 Master of Medical and Biotechnical Apparatus  
and Systems (with highest distinction),  
Faculty of Physics and Mathematics,  
Kazakh National Pedagogical University,  
Almaty, Republic of Kazakhstan.
- 09/1990-06/2000 Kazakh Secondary School № 164, Almaty, Kazakhstan.

## HONORS AND AWARDS

- 2007-2011 International Presidential fellowship of the  
Republic of Kazakhstan for Doctoral study – “Bolashak”,  
(Ph.D., Swiss Federal Institute of Technology,  
Lausanne, Switzerland);
- 2005-2007 International Swiss Federal Scholarship of Confederation  
for young scientists, “Research stage”, at Swiss Federal  
Institute of Technology, Lausanne, Switzerland;
- 2005 Presidential Fellowship for Post-graduate research  
at Eurasian National University, Astana, Kazakhstan.

## **PROFESSIONAL MEMBERSHIPS**

Since 2006      Swiss Physical Society (Switzerland).

## **TEACHING EXPERIENCES**

- 2008-2010  
(Four semesters)      Teaching–Assistant, General Physics I, II for Bachelor degree with Prof. **Marc Schiltz** and Prof. **Davor Pavuna**, at Swiss Federal Institute of Technology, Lausanne, Switzerland.
- 2008-2009      Student supervisor, **Master project**, “Near-field scanning optical microscopy using Polymethylmethacrylate optical fiber probes”, at Swiss Federal Institute of Technology, Lausanne, Switzerland.
- 2005      Laboratory Tutor, General Physics II, III for Bachelor degree, at Eurasian National University, Astana, Kazakhstan.

## **PUBLICATIONS IN PEER REVIEWED JOURNALS**

1. N. Suriyamurthy, B. S. Panigrahi, **K. Dukenbayev**, S. K. Sekatskii and G. Dietler, “Luminescence Studies of Photo Stimulated Phosphor CsBr: Eu<sup>2+</sup>”, submitted to Journal of Radiation Measurements.
2. H. Chibani, **K. Dukenbayev**, M. Mensi, S. K. Sekatskii and G. Dietler, “Near-field scanning optical microscopy using polymethylmethacrylate optical fiber probes”, **Ultramicroscopy**, Volume 110, issue 3, pp. 211-215, February **2010**.  
  
Highlighted in **Journal of Microscopy and Analysis**, Europe, Issue 129, p. 30, April **2010**.
3. M. Mensi, **K. Dukenbayev**, S. K. Sekatskii and G. Dietler, “Scanning Near-field Optical Microscopy based Study of Local Dynamics of Receptor Ligand Interactions at the Single Molecule Level”, **Laser Physics**, Volume 20, No. 1, pp. 78-84, **2009**.
4. D. V. Serebryakov, S. K. Sekatskii, A. P. Cherkun, **K. Dukenbayev**, I. V. Morozov, V. S. Letokhov and G. Dietler, “Scanning Near-Field Optical Microscope based on a double resonant fiber probe montage and equipped

with time-gated photon detection”, **Journal of Microscopy**, Vol. 229, pp. 287–292, Pt 2, **2008**.

5. **K. Dukenbayev**, S. K. Sekatskii, M. Dittrich, M. Mensi and G. Dietler, “Scanning Near-Field Optical Microscopy of Picocyanobacteria in Liquid”, 10<sup>th</sup> International Conference on Near-Field Optics, Nanophotonics and Related Techniques (NFO 10), **Proceeding of Conference book**, University of Buenos Aires, Buenos Aires city, Argentina, 1–5 September **2008**.
6. **K. Dukenbayev**, S. K. Sekatskii, D. V. Serebryakov, A. V. Zayats, G. Dietler, “Scanning near-field optical microscope based on double-resonant fiber probe montage and its operation in liquids”, in *Novel Photonics Materials: Optics and Optical Diagnostics of Nanostructures*, **Proceedings SPIE**, vol. 6728, 6728-84, **2007**.

#### **PUBLICATIONS PRESENTED IN CONFERENCES AND SCHOOLS**

1. 16<sup>th</sup> International Conference on Solid State Dosimetry, Sydney, Australia, 19-24 September **2010** (Poster presentation).
2. 11<sup>th</sup> International Conference on Near-Field Optics, Nanophotonics and Related Techniques (NFO 11), Peking University, Beijing, China, 29 August – 2 September **2010** (Oral presentation).
3. International Symposium SPIE Photonics Europe, Nanophotonics, The Square Conference Ctr., Brussels, Belgium, 12-16 April **2010** (Poster presentation).
4. Winter Doctoral School in Biophysics “Studying Biomolecules by Experiment and Theory: a Biophysist’s View”, Crans-Montana, Switzerland, 14-20 February **2010** (Poster presentation).
5. Summer Doctoral School in “Nano-Bio-Sensing”, Auditorium Polydôme, Swiss Federal Institute of Technology, Lausanne, Switzerland, 29 June-3 July **2009** (Poster presentation).
6. 10<sup>th</sup> International Conference on Near-Field Optics, Nanophotonics and Related Techniques (NFO 10), University of Buenos Aires, Buenos Aires city, Argentina, 1–5 September **2008** (poster presentation).

7. 39<sup>th</sup> IFF Doctoral School, “Soft Matter – From Synthetic to Biological Materials”, Institute of Solid State Research, Jülich, Germany, 03-14 March **2008**.
8. 9<sup>th</sup> International Conference on Near-field Optics, Nanophotonics and Related Techniques (NFO 9), EPFL, Lausanne, Switzerland, 10-15 September **2006** (oral presentation).
9. 10<sup>th</sup> Europhysical Conference on Defects in Insulating Materials (EURODIM 2006), University of Milano-Bicocca, Milan, Italy, 10-14 July **2006** (Poster presentation).
10. Annual Meeting of the Swiss Physical Society, Swiss Federal Institute of Technology, Lausanne, Switzerland, 13 - 14 February **2006** (Poster presentation).
11. 15<sup>th</sup> International Conference on Defects in Insulating Materials, (ICDIM-2004), Riga, Latvia, 11-16 July **2004** (Poster presentation).
12. 2<sup>nd</sup> Eurasian Conference on Nuclear Science and Applications, Almaty, Kazakhstan, 16-19 September **2002** (Poster presentation).

### **ORAL PRESENTATIONS**

- 08-09/2010    **K. Dukenbayev**, H. Chibani, M. Mensi, S. K. Sekatskii and G. Dietler: “Near-field scanning optical microscopy using polymethylmethacrylate optical fiber probes”, 11<sup>th</sup> International Conference on Near-Field Optics, Nanophotonics and Related Techniques (NFO 11), Peking University, Beijing, China.
- 02/2010        **K. Dukenbayev**, H. Chibani, M. Mensi, S. K. Sekatskii and G. Dietler: “Near-field scanning optical microscopy using polymethylmethacrylate optical fiber probes”, Doctoral School in Biophysics “Studying Biomolecules by Experiment and Theory: a Biophysist`s View”, Crans Montana, Switzerland.
- 05/2008        **K. Dukenbayev**, S. K. Sekatskii and G. Dietler: “Scanning Near-Field Optical Microscopy in Liquid”, Biophysical days, Swiss Federal Institute of Technology, Lausanne, Switzerland.

## **LANGUAGES**

Kazakh and Russian are mother tongues,  
English and French fluently.  
Basic knowledge of German.